AN EXPLORATION OF CHEMICAL AGENTS DETECTION USING THE QUANTUM FINGERPRINT^{TM} TECHNOLOGY

A Dissertation
presented to
the Faculty of the Graduate School
at the University of Missouri

In Partial Fulfillment
of the Requirements for the Degree
Doctor of Philosophy

---

by

Annie YuNing Hsu Tipton

Dr. Robert V. Tompson, Jr., Dissertation Supervisor
Dr. Mark A. Prelas, Dissertation Supervisor

August 2009

The undersigned, appointed by the Dean of the Graduate School, have examined the dissertation entitled

AN EXPLORATION OF CHEMICAL AGENTS DETECTION USING THE QUANTUM FINGERPRINT^{TM} TECHNOLOGY

presented by Annie YuNing Hsu Tipton
a candidate for the degree of Doctor of Philosophy
and hereby certify that, in their opinion, it is worthy of acceptance.

Dr. Robert V. Tompson, Jr.

Dr. Mark A. Prelas

Dr. Tushar K. Ghosh

Dr. Sudarshan K. Loyalka

Dr. Dabir S. Viswanath

This work is dedicated to my husband Lynn and my family (Landon, Chrissie, Ruthie, Blake, Jennifer, Frank, Linda, and Lynn), for their love and support.

ACKNOWLEDGMENTS

Deepest gratitude and appreciation to my advisors, Dr. Tompson and Dr. Prelas. I am thankful for their patience and support they have given me over the years.

I am thankful for the great advice, support, comments, and suggestions from my Ph.D. committee members, Dr. Loyalka, Dr. Ghosh, and Dr. Viswanath.

I am thankful for the help and friendship of Latricia J. Vaughn and James C. Bennett from the Nuclear Science & Engineering Institute.

Many thanks to the following students, Daniel, Jason, and Jose. I am thankful for their suggestions, comments, discussions, help, and the many hours we have worked together. Gwen and Rob for helping me with some of the preliminary sensor chips.

I am thankful for the constant supervision and proofreading of this dissertation from Lynn.

I would also like to thank the following organizations for financial support in order for the completion of my work: the U.S. Department of Energy for Nuclear Engineering Education Research (NEER) grant, the U.S. Department of Energy for Innovation in Nuclear Infrastructure and Education (INIE) grant, and the research grant from the Leonard Wood Institute (LWI).

Contents

ACKNOWLEDGMENTS ii

LIST OF TABLES vi

LIST OF FIGURES viii

ABSTRACT xi

CHAPTER

1 Introduction 1

1.1 Scope of this work 2
1.2 Classification of sensors 4
1.2.1 Thermal sensors 6
1.2.2 Mechanical sensors 7
1.2.3 Electromagnetic sensors 8
1.2.4 Optical sensors 9
1.2.5 Biological sensors 9
1.2.6 Chemical sensors 10
1.3 Key aspects to be addressed in new sensors 14

2 Literature Review 15

2.1 Material selection 15
2.2 Surface states of solid-state materials 18
2.2.1 Crystalline structure 18
2.2.2 Impurities in semiconductors 19
2.2.3 Surface states 21
2.3 Metal contacts on semiconductor substrates 23

2.3.1 Schottky barrier and contact formation 23
2.3.2 Contact resistance measurements 25
2.3.3 Formation of ohmic contacts 28
2.3.4 Ohmic contacts on n-type Si 29
2.3.5 Ohmic contacts on 4H-SiC 30
2.3.6 Metal contacts on sapphire 32
2.4 Application of Q-DLTS system for sensor 34
2.4.1 Systems for the characterization of deep-level impurities . . 34
2.4.2 Capacitance transient measurements 35
2.4.3 Current transient measurements 38
2.4.4 Charge transient measurements 39

3 Methodology **46**
3.1 Material specifications 46
3.2 Metal contacts on semiconductors 49
3.2.1 Material characterization of semiconductors 49
3.2.2 Electrical characterization of semiconductors 51
3.2.3 Substrate cleaning 52
3.2.4 Termination bonds on the substrate surfaces 55
3.2.5 Deposition of metal contacts 56
3.3 Setting up a sensor fabrication and testing environment 58
3.3.1 Construction of a controlled cleanroom environment 58
3.3.2 Enclosures for sensor testing 60
3.3.3 Construction of a vacuum system for sample introduction . . 62
3.4 Data processing 62
3.4.1 Data collection and signal analysis for MU prototype QDLTS unit 64
3.4.2 Investigation of other signal analysis approach 65

4 Results and Discussion **69**
4.1 Results of preliminary tests on commercially packaged QF^{TM} sensor chips 69
4.1.1 Characterization and preparation of prototype QF^{TM} sensor chips 69

4.1.2 Preliminary measurements 71
4.1.3 Discussion of the results from preliminary QF™ sensor chips 75
4.2 Preliminary prototype Q-DLTS unit and computer code evaluation 78
4.3 In-house silicon sensor chips 81
4.3.1 Material characterization and preparation 82
4.3.2 Fabrication and experimental matrix for silicon sensor chips 87
4.3.3 Q-DLTS signals for silicon sensor chips 92

5 Conclusions and future work 105

Bibliography 114

A MU prototype Q-DLTS unit 115

VITA 116

List of Tables

Table **page**

1.1 Ideal sensor characteristics. 2
1.2 Functional classification of commercialized sensors. 5
1.3 Various types of solid-state gas sensors. 13

2.1 Properties of silicon and wide bandgap semiconductors. 17
2.2 Properties of metals used in metallization. 25
2.3 Several examples of ohmic contacts to silicon from the literature. . . 30
2.4 Ohmic contacts to n-type 4H-SiC. 31
2.5 Metal contacts to sapphire. 33
2.6 Summary of capacitance, current, and charge deep-level transient spectroscopy measurement methods. 35

3.1 Specifications of semiconductor materials used. 48
3.2 Sources of substrate surface contaminants. 53
3.3 Specifications of the cleanroom at NSEI. 60

4.1 Thermal treatment parameters used for the lithographically fabricated sensor chips. 70
4.2 Prototype QF^{TM} sensor chips. 71
4.3 A proposed metallization experimental matrix for 4H-SiC based sensor chips. 76
4.4 A proposed metallization experimental matrix for sapphire based sensor chips. 78
4.5 Specifications of commercial diodes used for Q-DLTS evaluation. . . 79
4.6 Specifications of commercial diodes used for Q-DLTS evaluation. . . 81
4.7 Resistance measurements from four-point probe. 87

4.8 Experimental matrix for silicon sensors. 89

List of Figures

Figure **page**

2.1 Carrier concentration for various intrinsic materials. 16
2.2 Crystalline defects. 20
2.3 Energy level diagram for a deep-level impurity. 21
2.4 Various types of barriers formed at metal and semiconductor interfaces. 26
2.5 A schematic of two-point probe setup with cross-section and top view. 28
2.6 Schematic of a four-point probe setup. 28
2.7 Relationship between double boxcar approach and corresponding DLTS signal. Capacitance transient measurements are taken at different times as a function of temperature [1]. 37
2.8 A simplified circuit diagram for Q-DLTS measurement (adapted from [2]). 41
2.9 A diagram on sample collection's timing sequence (adapted from [2]). 41
2.10 Circuit diagram of QDLTS system. 44
2.11 Time sequence diagram of signal input and output. 45

3.1 Process sequence for fabrication of a typical sensor chip. 47
3.2 Cleanroom arrangement. 59
3.3 Enclosures for sensor testing. 61
3.4 Vacuum system design. 63
3.5 Vacuum system and gas mixing apparatus. 63
3.6 Flow chart of computer program. 68

4.1 2" diameter Si wafer with interdigitated pattern. 69
4.2 Prototype packaging of QF^{TM}. 71

4.3 Current-voltage curves for the 6H-SiC sensor chips. 73
4.4 Q-DLTS spectra measured using the ASMEC system with a Vaisala HUMICAP humidity sensor with introduction of 1 mL isopropanol in a background of atmospheric air. 74
4.5 Q-DLTS of 6H-SiC sensor chip (SN02C) measured using the ASMEC system with presence of isopropanol and water vapor in a background of atmospheric air. 75
4.6 Damaged wafers. 77
4.7 Preliminary examination of diodes with Q-DLTS. 81
4.8 Q-DLTS spectra of a RC sample. 81
4.9 Some representative material characterization measurements for silicon substrates used in this work. 83
4.10 A SEM image indicating test locations on a representative sample. . 84
4.11 EDS spectra from a representative sample of metallized silicon (Point 1, 2, and 3). 84
4.12 EDS spectra from a representative sample of metallized silicon (Point 4, 5, and 6). 85
4.13 Current-Voltage response of silicon substrates. 86
4.14 Resistance testing using transmission line method. 92
4.15 In-house silicon sensor chips designs. 93
4.16 A representative of leakage current observed for high resistivity silicon substrate. 94
4.17 A representative of leakage current observed for low resistivity silicon substrate. 95
4.18 Q-DLTS signals of various target species 98
4.19 Q-DLTS signals of various target species after substraction background (air) 99
4.20 Q-DLTS signals measured in vacuum system for sensor chip BSC5 in N_2 gas. 102
4.21 Q-DLTS signals measured in vacuum system for sensor chip BSC5 in CO_2 gas. 103
4.22 Q-DLTS signals measured in vacuum system for sensor chip BSC5 in CH_4 gas. 103

4.23 Q-DLTS signals measured in vacuum system for sensor chip LS2 in a mixture of 5% Ar and 95% N_2 gases. 104

A.1 A schematic diagram of MU prototype QDLTS unit. 115

ABSTRACT

The detection of chemical agents using a novel, gas-phase, sensor technology has been examined experimentally in this work. The goal of the work was to determine the feasibility of using solid-state materials as gas-phase Quantum Fingerprint ^{TM}(QF^{TM}) sensors. The energy levels created by various targeted species adhered on the semiconductor substrate surface, acted as charge traps which can be excited and the transient signals associated with their relaxation examined. A Charge-based Deep Level Transient Spectroscopy (Q-DLTS) system has been used to characterize the deep level states created by surface impurities. In this research, critical components have been examined for the development of such sensor technology. These include selection of appropriate semiconductor substrates and metal contacts for ohmic contacts, fabrication protocols and metallic pattern designs for optimal signals, development of sensor technology measurement protocols, and testing of sensor chips under a controlled environment. The substrate materials tested in this work include silicon, silicon carbide, and sapphire. Fabrication of each sensor chip followed stringent material cleaning procedures to prevent contamination that would affect performance and integrity of the metallization. A few chemical agents were selected for testing, which included: water, 1-propanol, isopropanol, methanol, butanol, ethanol, nitrogen gas, argon gas, and methane gas. The testing of the sensor chips was performed in a controlled, high vacuum environment, isolated from the presence of other species. The experimental measurements made in this work have shown some dependency of targeted species concentrations and pressures with electrical charge collected from trap centers.

Chapter 1

Introduction

Sensors are an integral part of modern society. With the advance of science and technology, utilization of sensors in areas such as national security, industry, transportation, agriculture, commerce, and health care has escalated explosively. Many detection mechanisms are used to address needs in these different areas. Here, a novel, gas-phase, sensor technology, the Quantum Fingerprint^{TM} (QF^{TM}) is explored experimentally. The QF^{TM} is potentially capable of providing more effective responses and greater versatility in many applications. Some characteristics of the QF^{TM} include high sensitivity, high selectivity, fast acquisition and response rates, portability, and robustness. High sensitivity is desired for the detection of trace amounts of target species at concentrations normally considered too low to detect. High selectivity is needed to accurately discriminate target species in complex, mixed-species, environments. Fast sampling and data processing are also preferred, because they determine the overall response time which defines how close to real-time the sensor can function. For the detection of multiple target species, fast response time ensures minimum delays between measurements even when discriminating one species from others.

All of the above characteristics of the QF^{TM} sensor are, of course, desirable in all sensors in general. Additionally, all sensors should preferably be robust, portable, and inexpensive like the QF^{TM} sensors. To be maximally effective, they must also be user-friendly. The likely environment in which a sensor will be deployed should

be taken into consideration as the robustness and portability of the sensor may vary under different conditions. What output format will the sensor have? Will the readout be easily understood at a glance? Will the readout be informative? All of these characteristics need to be addressed during the initial sensor design. A summary of all the above-mentioned, desirable, sensor characteristics are tabulated in Table 1.1 [3, 4].

Table 1.1: Ideal sensor characteristics.

Characteristic	Description
Sensitivity	The capability to detect various levels of the target species concentration and to measure minimal change in the input signal.
Selectivity	The capability to discriminate between the detected species.
Data Acquisition & data processing response rate	A fast acquisition and dada processing rate could allow minimum time required to sample and to respond to a situation.
Hysteresis	The evaluation of a sensor's performances (output) change due to extended operation period.
Robustness	An optimal operating life, low maintenance, and reliability under rugged conditions are desirable.
Portability	The size and weight will determine the practicality of where the device will be deployed.
Cost	Reasonable price.
User interface	User friendly output format.

1.1 Scope of this work

The goal of this work is to determine the feasibility of using certain solid-state materials as gas-phase QF^{TM} sensors, in which the creation of signature deep-level energy traps on the sensor surface identify and quantify various target species. Ide-

ally, this sensor would have high sensitivity with the potential of detecting parts per billion or fewer molecules adsorbed onto the sensor surface. Also, high selectivity would be preferred for discerning various chemical or possibly biological species. Fast data acquisition and processing rates that could provide rapid detection-warning responses are also a goal of this work. Robust hardware and portability that would allow for low maintenance and easy deployment would also be desirable; but equipment design is not within the scope of this effort. Further, simplicity in device design that would allow for it to be reasonably priced and, hence, widely available would be preferred. However, such design/manufacturing/marketing concerns are also outside the scope of this work. The QF^{TM} sensor being studied is a solid-state device in which energy levels created by target species deposited on the surface of a semiconductor substrate act as charge traps which can be excited and the transient signals associated with their relaxation examined. The backbone of the QF^{TM} sensor is the use of Charged-Based Deep Level Transient Spectroscopy (Q-DLTS) for surface signal detection. The Q-DLTS system is commonly used for characterizing deep level impurities in bulk semiconductor materials. For the purpose of this research, the Q-DLTS system is used for characterizing the deep level states created by surface impurities. The change in surface states arises from the energy differences due to the surface, any chemically bonded surface species and the attractive van der Waals forces that bind molecules of the target species onto the sensor surface. Key components critical to the design of a QF^{TM} sensor include the selection of appropriate metal contacts and semiconductor substrates to minimize Schottky barrier formation at the interface, and the design of an optimal metallic pattern for signal collection that will maximize the signal-to-noise ratio. An ohmic contact is desired at the metal to semiconductor interfaces, to minimize the contact resistance and, hence, allow for the maximum linearity in the transient currents being measured. Within the scope of this work, the following goals were pursued using prototype sensors:

1. Development of QF^{TM} sensors using silicon (Si), 4H-silicon carbide (4H-SiC), and sapphire (Al_2O_3) substrates;

2. Development of metalization recipes and metalization protocols for making ohmic metal contacts on the above substrate materials;

3. Development of a preliminary design for potential commercial chips;

4. Development of standardized in-house chip designs for non-commercial testing purposes;

5. Development of partial packaging specifications for the above substrate materials was included in anticipation of future commercial products and applications;

6. Testing of the prototype QF^{TM} sensor chips using a commercially available Q-DLTS system and a separately developed in-house prototype QF^{TM} system, and;

7. Testing of the prototype QF^{TM} sensor chips for sensitivity to pure samples of the following materials: He, Ar, N_2, CO_2, H_2O, and some alcohols.

1.2 Classification of sensors

The purpose of a sensor is to convert some physical phenomenon into information that can be registered by people and/or their mechanisms. Prime examples are found in the human sensory systems which include vision (eyes), hearing (ears), smell (nose), taste (tongue), touch (skin), and balance (inner ear). People are constantly receiving information from these senses, processing it, and interacting with their surroundings in response to the processed information. Human sensory cells in these systems sense the various physical phenomena and send signals to the corresponding regions of the brain where interpretation of the signals takes place

and responses are initiated. However, the human sensory systems have limited capabilities. For instance, human vision only responds to wavelengths between 380 nm and 750 nm and deteriorates with age. Human hearing has a limited audio frequency range between 20 Hz and 20 kHz. Human smell is capable of discerning different smells but not the level of concentrations [5] and can be confused by different species that stimulate the same olfactory cells and nerves yielding identical signals. With such natural limitations in human sensory systems, alternative sensors have been designed to cover a much wider range of inputs to compensate for these human shortcomings. Numerous alternative sensing mechanisms have been designed to fit various niches. With the increasingly compact size of integrated circuit (IC) technology, the extensive use of sensors in day-to-day life in numerous hand-held portable devices has expanded to the point that sensor technology is now observable in all aspects of the modern lifestyle. Prior to the development of the fundamentally new QF^{TM} sensors used in this research, the various sensor technologies that were available were quite diverse. A few of them are examined here to place the QF^{TM} technology in perspective. In Table 1.2 [6,7], a selection of commercial sensors are listed according to their functionality. Of course, there is some overlap in the various categories. In the sections that follow, details of their functions and detection mechanisms are discussed.

Table 1.2: Functional classification of commercialized sensors.

Functional Classification	Type of Sensors (Examples)
Thermal	Silicon, thermocouple, thermistor, resistance temperature detector
Mechanical	Pressure/Force (Pressure gauge, Strain gauge) Acceleration (Accelerometer) Position (Linear Variable Differential Transformer) Humidity (Hygrometer)
Electromagnetic	Magnetic (Magnetic motion sensor, Hall effect sensor)
Optical	Photodiode, thermal infrared detector

Continued on Next Page...

Table 1.2 – Continued

Functional Classification	Type of Sensors (Examples)
Biological	Resonant biosensors, optical biosensors, thermal biosensors, ion-sensitive field-effect transistor biosensors, electrochemical biosensors
Chemical	Gas sensors

1.2.1 Thermal sensors

Thermal sensors are used for detecting temperature and/or changes in temperature. Some class examples of thermal sensors include silicon temperature sensors, thermocouples, thermistors, and resistance temperature detectors (RTDs). Each of these thermal sensors serves its purposes differently. For instance, they each may operate best in different temperature ranges and, thus, selection of the best sensor for a given application must take into account both the specific details of the application and the relevant specifications of the various sensor types. No one sensor does the entire job best; a common theme with modern sensors across the board.

Silicon temperature sensors are used in integrated circuit (IC) design and are intended for integration into electronic instruments. This is mainly because of their high sensitivity and temperature-dependent linearity with respect to electrical resistance. Temperatures ranging from cryogenic (1.4 K) to 200 °C can be detected [6].

Thermocouples are widely used devices for temperature measurements. They can withstand substantial shocks and vibration, and are sensitive to temperatures ranging from -200 °C to 2315 °C. The principle behind the thermocouple is the Seebeck effect. When two electrical conductors of different metals or alloys come into contact at one end, the presence of a temperature difference will cause an electromotive force (voltage) to form in the circuit. The magnitude of the voltage

that develops then corresponds to the temperature [6, 8]. Even here, no single thermocouple serves every purpose equally well because the sensitivity and linear response ranges of different conductor pairings are notably different for various temperature ranges.

Thermistors are temperature sensitive resistors made out semiconductor oxides. The conductivity of a thermistor is proportional to the change in temperature. Generally, a change in one to five percent resistance corresponds approximately to a degree Celsius difference. The advantages of using a thermistor include: a wide operating and measurement range, small in size, and can withstand electrical and mechanical stresses. Thermistors are typically applied in areas of thermal, thermal conductivity, infrared, and audio and radio frequencies measurements are just to a name a few [9].

Resistance temperature detectors (RTDs) measure temperature variation in response to change in electrical resistance of metals. The temperature readings are proportional to the resistance changes; or simply, the resistance of a conductor increases due to elevated temperature. Platinum is a widely used material because of its chemical stability thus suitable for long-term use, obtainable in high purity form, and high endurance to electrical stresses.

1.2.2 Mechanical sensors

Mechanical sensors deal with physical displacements. This category of sensors can be further broken down into pressure/force sensors, accelerometers, position sensors, and humidity sensors depending upon the mechanism via which an input is supplied.

A pressure/force sensor measures deformation as a result of an applied pressure or strain and converts this to an electrical output. For example, a piezoelectric transducer generates electrical polarization when the crystal is subjected to mechanical pressure, allowing one to measure the charge produced [6].

An accelerometer operates based on Newton's laws of motion. Accelerometers are widely used for measuring acceleration, vibration, and shock [6].

An example of a position sensor is the linear variable differential transformer (LVDT) used to measure linear distance displacement. Functionally, it consists of a primary coil sandwiched between two secondary coils wound into a cylinder; essentially a kind of transformer. A magnetic core is mechanically attached to the object for which the position is to be measured. Inside the transformer, the core is free to move in the bore laterally when the primary coil is subjected to an alternating current (AC). Under the influence of a current, the primary coil creates inductance which affects the secondary coils and the output signal is simply the differential voltage of the secondary coils [6].

Humidity sensors are used for measuring water vapor content in the air. Most humidity sensors today are made out of solid-state materials and detect humidity based on changed in capacitance, resistance, and thermal conductivity in the material due to exposure to humidity [6].

1.2.3 Electromagnetic sensors

Electromagnetic sensors operate based on Faraday's law of electromagnetic induction. A voltage will be induced as a conductor moves through a magnetic field.

A magnetic motion sensor design for instance, places a loop of wire between two poles of a magnet. A magnetic field is confined within this region. The magnetic flux is related to width of the wire loop, length of the wire loop, and the magnetic field of the magnet. Voltage is induced as a function of magnetic flux versus time. When the wire loop is displaced laterally, the voltage changes. Such a mechanism can be used to detect seismic signals or other low-frequency vibrations [6].

For a Hall effect sensor, the current flowing though an electrical material is affected by the presence of an external magnetic field. The output voltage of a Hall effect sensor therefore changes in response to any varying of the magnetic

field. These types of sensors are often used in speed detection, current sensing, and digital switching [6].

1.2.4 Optical sensors

The electromagnetic characteristics of photons allow light and its intensity to be measured by optical sensors. Some optical sensors are briefly discussed below.

A photodiode is essentially a p-n junction diode. Rather than the use of a reverse bias, photons are used to excite the mobility of electrons and holes across the junction. A photocurrent is then produced when the absorbed photons have enough energy to travel through the junction [6] and this current can be measured. The photon flux at the sensor is then proportional to the current generated.

Thermal infrared detectors operate by absorption of infrared radiation which causes measurable temperature changes. Thermal infrared detectors are independent of incident wavelength; any energy absorbed will lead to detector responses [4, 6, 10].

1.2.5 Biological sensors

A biological sensor is defined as a device that incorporates a biological structure as part of the detection mechanism. Some of these biological structures include enzymes, antibodies, bacteria, and proteins [3,7]. The complex biochemical nature of many specimens generally makes the lead time between preparation of the sensor and procurement of the results a long process. It is also usually a multi-step process that can involve not only collection but, concentration and remote laboratory analysis steps.

A clear distinction between biological sensors and chemical sensors is sometimes not apparent. The main difference is that a biosensor often requires a medium to transfer data from the biological aspect to information that can be interpreted. Often times, this bridge outputs the biological information as electrical or other signals (i.e. current, voltage, capacitance, temperature, impedance, and so forth)

[7]. A resonant biosensor, for instance, has an acoustic element associated with. This physical element is coupled to a membrane with selective antibodies attached. When antigens come in contact with the membrane, the mass of the membrane is changed which results in a change in the resonant frequency of the membrane which can be measured [7].

Thermal biosensors operate based on the thermal properties associated with biochemical reactions. Changes in temperature, whether by heat absorbed or produced, may be proportional to the number of molecules involved and their molar enthalpies [7].

Ion sensitive biosensors are another example. Here, the surface electrical potential of a semiconductor material is changed due to interaction with ions. Ions also could be measured selectively, this often involves a polymer coating that has a selective permeability to target specific analyte ions [7].

1.2.6 Chemical sensors

Chemical sensing is based on various chemical reactions among the target species. Use of chemical sensors is typically for identifying specific chemical elements or compounds and the concentration present in liquid or gas form. Various chemical sensors and their detection mechanisms will be reviewed here. This is to provide understanding for existing chemical sensors and context for the novel, QF^{TM} sensor technology.

Existing chemical sensing mechanisms can be categorized as either direct or indirect [4]. For direct chemical detection, once a chemical species is detected, an output of some measurable electrical quantity is generated immediately, i.e. resistance, potential, current, or voltage. For indirect chemical detection, an indirect step is required. Information from the target creates some form of physical change such as changes in shape, frequency, temperature, or mass which is then output as electrical signals [4].

A notable category of chemical sensors are gas detecting sensors. There are many materials used for such sensors. Materials include: solid-state materials, plastics, metals, ceramics, and glasses [4]. Solid-state materials are of special interest, these generally exhibit the following characteristics: (a) an electrical resistivity in the range of 10^{-3} and 10^{9} Ω·cm, between that of a metal and that of an insulator, (b) a negative temperature coefficient for electrical resistivity, and (c) an electrical conductivity that can change by orders of magnitude under the influence of temperature, optical excitation, excess charge carrier injection, or impurity concentration [11, 12].

Since the understanding that semiconductive metal oxides are gas sensitive at increasing temperatures, the feasibility of using such solid-state materials as gas sensing devices has been systematically explored. The demand for environmental gas sensing at sub-ppm concentration levels are needed for fire detectors, indoor hazardous gas detectors, volatile organic compound detectors (VOC) [13], outdoor air quality monitoring, and potential hazardous chemical agents attack. These solid-state devices can be manufactured in compact sizes, high sensitivities (ppm or even ppb range) for a variety of chemical compounds, real-time monitoring, and possibly low cost [13].

Solid-state gas sensors detect gases via interaction of the chemical species with the material surface by monitoring the changes in electrical conductivity, work function, mass, optical characteristics, and chemical reactions at gas-solid interfaces [13]. A brief summary of commercially available solid-state gas senors is given in Table 1.3. An overview of some of these gas sensors is also provided. Generally, these sensors monitor changes in electrical resistance, electrical current, mass, temperature, and optical properties [13].

Semiconductor gas sensors are typically made from metal oxide substrates such as ZnO, NiO, SnO_2, TiO_2, In_2O_3, and WO_3 [13]. Interactions at gas-solid interfaces usually involve one of the following processes: (a) reduction-oxidation processes,

(b) adsorption on semiconductor surface, (c) adsorption followed by chemical reaction with surface states, and (d) catalytic effects between surface chemicals and adsorbed chemical species [13]. The gas/solid interactions can lead to changes in the electrical resistance of the sensor, its surface conductance, or its bulk substrate conductance. For example, oxygen adsorbates can be used to detect inflammable gases like H_2 and CO. O^- reacts with inflammable gases and, as concentration varies with surface coverage, a space-charge region builds up on metal oxide surfaces. Changes in electrical resistance can be observed in conjunction with increasing or decreasing oxygen concentration [14]. Semiconducting gas sensors are simple to fabricate, but selectivity and sensitivity are typically poor. Metal oxide films are sensitive to water vapor and also to environments with more than one chemical species present, therefore the lack of selectivity is a problem since cross species detection is common. Long periods of use can affect the stability of these devices and such effects may include: 'drifts' in the baseline signal and 'drifts' in the sensor response curve. The causes of these instabilities are primarily changes in granular size and number distributions at the surfaces and boundaries of the sensing elements. Other influences may also include contamination and irreversible chemical reactions with the detected species [13].

Electrochemical gas sensors operate based on chemical species reacting chemically with electronic/ionic interfaces. An electrochemical element usually consists of some chemical reactant (electrolyte or gel) that is in contact with two terminals (an anode and a cathode). Oxidation may take place at the anode and reduction at the cathode, thus a current flow is created with a direction that depends on whether ions are positive or negative. Gases that are electrochemically reducible, such as oxygen, nitrogen oxides, and chlorine will be detected at the cathode end. While gases such as carbon monoxide, nitrogen dioxide, and hydrogen sulfide are electrochemically oxidizable will be detected at the anode end. For an oxygen gas sensor, an external voltage is usually supplied to the cathode to maintain mini-

mal oxygen concentration. A current response is then observed when there is a diffusion of oxygen into this region [13].

Table 1.3: Various types of solid-state gas sensors.

Sensor devices	Manufacturer	Targeted species	Detection mechanism	Detection limit
Semiconductor gas sensors	Figaro, Dräger	Air quality, VOCs, CO, H_2	Electrical conductivity (resistivity)	0 to 2000 ppm
Field effect gas sensors: diodes, transistors, capacitors	–	–	Work function	–
Piezoelectric sensors: Quartz crystal microbalances (QMB), surface acoustic wave (SAW)	MSA	Chemical warfare agents (nerve and blister agents)	Mass change	0.3 to 1.4 mg m^{-3}
Optical sensors: Fiber optic	E2V	Methane, CO_2	Reflection, interferometry, absorption, fluorescence, refractive index	0 to 100% by volume
Catalytic gas sensors: Pellistor	City Technology	Combustible gases and vapors	Temperature change due to combustion	0 to 100% LEL
Electrochemical gas sensors: Potentiometeric, amperometric, and conductimetric	General Monitors, Inc.	H_2S, ammonia, CO, HCL, NO	Electrolyte (ions)	0-500 ppm

1.3 Key aspects to be addressed in new sensors

Challenges still exist for current sensor technologies. Selectivity, sensitivity, detection limits, response times, irreversibility, and device aging are just some of the issues inherent to sensor performance that have to addressed. Solid-state materials are of particular interest because they are low cost, robust, and relative easy to work with. As advances in micro- and nano-technology yield smaller sensors, the performance of miniaturized sensors will ultimately involve a whole new set of challenges also. Choices of materials and fabrication methods are some of the parameters to be factored into future sensors. The development of wireless and global satellite technologies and the capability for quick reference to online databases will also be features for future real-time sensing and signal analysis. There are, of course, other factors to be considered in future sensors development. This is only a sampling of issues certain to become even more important as sensor technology advances. All of the old issues continue to be of importance as well and it is further certain that future sensor developments will reveal issues of importance of which we are currently unaware.

Chapter 2

Literature Review

In this chapter, the theory and development of Quantum Fingerprint^{TM} (QF^{TM}) sensors will be discussed. This technology was invented and patented by Dr. Mark Prelas and colleagues at the University of Missouri (MU) [15]. The QF^{TM} sensor is envisioned as means to detect chemical and biological species that are adsorbed onto semiconductor substrate surfaces. Surface adsorption results in the creation of deep-level energy traps are unique to the adsorbed species. Charge-based transient spectroscopy method may be used to identify and quantify these deep-level energy traps [15]. The content of this chapter will address the fundamentals necessary for the understanding, fabrication, and testing of such sensors.

Sections of this chapter will address: (1) material selection for QF^{TM} sensor chips, (2) metal-semiconductor contacts for QF^{TM} sensor chips, (3) change in surface potential due to adsorption, and (4) the use of charge-based deep-level transient spectroscopy (Q-DLTS) as a QF^{TM} sensing modality.

2.1 Material selection

The predominate trend for solid-state electronics has been the use of silicon-based substrates because of their versatility, availability, and cost. Silicon is used as the base material in making of diodes, microprocessors, solar cells, semiconducting detectors, to name a few. However, the use of silicon as a base material for electronics does have a few drawbacks. Since it is limited to a lower operating temperature and

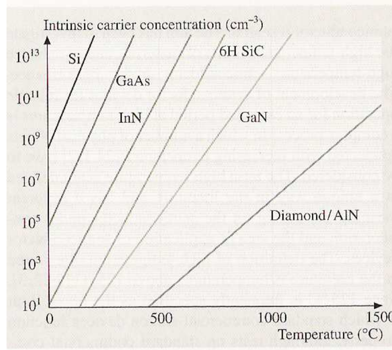

Figure 2.1: Carrier concentration for various intrinsic materials. [18]

has a lower electric field breakdown voltage. The use of wide bandgap materials have been explored as they do not exhibit these limitations. Wide bandgap materials exhibit an energy gap of 2.2 electron volts (eV) or greater. Wide bandgap materials are superior to silicon in many areas. These materials have a higher operating temperature (above 600°C) and thermal conductivity to allow better heat dissipation. A higher electric field breakdown voltage enables operation at high power and allows for denser packaging capabilities for integrated circuit systems [12, 16]. The thermally generated leakage current is also 10 to 14 orders of magnitude lower than conventional semiconductors (silicon based) at any given temperature [17]. In Figure 2.1, the temperature dependence of various intrinsic materials versus carrier concentration is shown. These trend lines shown in the figure clearly depict that, wide bandgap materials are less affected by the deterioration due to thermally excited carriers [18], thus, a wider range of operating temperature.

A common practice in semiconductor industry is to vary the dopant concentration in the substrate to adjust the electrical conductivity of the material. And, as a result, alter the energy band structures. These materials are called as extrinsic materials. For the proposed QF^{TM} sensor chips, intrinsic materials are preferred, since this category of materials do not have impurities or lattice defects in their crystals. In addition to the use of intrinsic materials, as previously discussed, wide

energy bandgap materials are of particular interest for the development of a QF^{TM} sensor chip. Examples of these include: silicon carbide, diamond, sapphire, aluminum nitride, and gallium nitride. Electrical properties for these materials are tabulated in Table 2.1 below. These properties are of particular interest because they could help suggest the optimal conditions a selected substrate material could be used in.

Silicon was identified as a test material for preliminary studies in this work. Silicon is widely available and low cost; it is an excellent material to demonstrate and benchmark the feasibility for QF^{TM} sensor chips. However, to further assess usability of other materials, two wide bandgap materials, namely 4H-SiC and sapphire were identified for this study. Both 4H-SiC and sapphire are commercially available and lower cost when compared to other wide bandgap materials. By selecting these three materials, this work would examine a range of material property values exhibit by semiconductors.

Table 2.1: Properties of silicon and wide bandgap semiconductors [17, 19, 20].

Property	Si	4H-SiC	AlN	Diamond	Sapphire	GaN
Bandgap (eV) at room temperature	1.12	3.26	6.2	5.45	9.9	3.45
Dielectric constant	11.9	10.1	8.6	5.7	11.5	9
Electric breakdown field (kVcm^{-1})	300	2200	–	10000	170	2000
Electron mobility ($cm^2V^{-1}s^{-1}$)	1500	1000	–	2200	–	1250
Hole mobility ($cm^2V^{-1}s^{-1}$)	600	115	–	2200	–	850
Thermal conductivity (W $cm^{-1}K^{-1}$)	1.5	4.9	2	22	0.3-0.5	1.3
Thermal expansion coefficient (10^{-6}/K)	2.6	–	–	1.18	8.8	–

2.2 Surface states of solid-state materials

2.2.1 Crystalline structure

The considerations for design of an electronic device based on a semiconductor material are different than those encountered when using other solid materials (i.e. insulators and conductors). Interactions occurring at the surface of the material could favor a particular orientation of crystal lattice. Energy level associated with the surface, or near the surface would be distorted significantly if the chemical bonds were broken. In the case of silicon carbide, depending on which plane the crystal was terminated, interaction of the exposed, dangling bonds with a gas may be different. For the case of an air atmosphere, the silicon terminated plane could be easily attack by oxygen in the air. Whereas carbon terminated plane would be more stable.

Another important consideration for semiconductor materials is that the density of a unit cell volume of the crystal. Mechanical properties such as the hardness and etching effects to various planes can be determined depending on the crystal. A periodic structure of crystal lattice can determine the allowable energy states, which will also impact electrical conductivity of the material [11, 21]. The crystal structure of silicon has a face-centered cubic ($f$cc) unit cell in which there are eight atoms at the corners and six at the center of each plane of a unit cell. Other solids that also have this structure (referred to as a diamond structure) are carbon, germanium, and tin. A unit cell of silicon has a lattice spacing of 5.43Åand a packing density of 34%, which is much less than the packing density of 74% for a regular *fcc* unit cell [11,21]. Here, the packing density typically refers to occupancy by the solid atoms in each unit cell, and hence, is the volume density of the solid.

A crystal Lattice of silicon carbide has a variety of polytype structures [22]. Differences in polytypes are identified by the stacking sequence of silicon and carbon atom layers. The basic structure for a unit cell of silicon carbide crystal is

a tetrahedron of four carbon atoms with silicon atom in the center. The lattice spacing between the carbon atoms and the silicon atom is 1.89Å, and the distance between the carbon atoms is 3.08Å. It is also useful to note that the crystal structure of silicon carbide has a unit cell spacing which is a close match to any nitride based semiconductors (gallium nitride, aluminum nitride, etc). Silicon carbide substrate is often used as a base substrate for epitaxial growth of the nitride based semiconductors [22, 23].

Sapphire substrates are also used for nitride epitaxy. Although, substrates like SiC, MgO, and ZnO are generally preferred because of better lattice match. Application of sapphire were largely used as base substrates in electronics manufacturing. A few advantages for sapphire include: the hardest of oxide based materials, good optical properties (transparent) and thermal properties, and resistant to chemicals. The crystal structure of sapphire has a hexagonal geometry and the unit cell has lattice parameters of $a = 4.76$Åand $c = 13$Å [20, 24].

2.2.2 Impurities in semiconductors

For a perfect single crystal semiconductor, the conduction and valence bands are separated by an energy band gap with no energy levels allowed within this band gap (also known as forbidden gap). Energy levels are created by perturbations in the periodic crystalline structure via crystalline defects or the introduction of foreign atoms (also known as dopant atoms or impurities) to the crystal lattice. Some examples of the defects include: (1) foreign interstitial, (2) foreign substitution, (3) vacancy, (4) self-interstitial, (5) stacking fault, (6) edge dislocation, and (7) precipitation [25]. A schematic drawing of various defects is shown in Figure 2.4 [25].

The inherent impurity concentration of a semiconductor is on the order of 10^{-7} to 10^{-3} for each atom in the crystal [26]. Changes in the impurity concentration can be introduced via dopant atoms. The presence of impurities results in

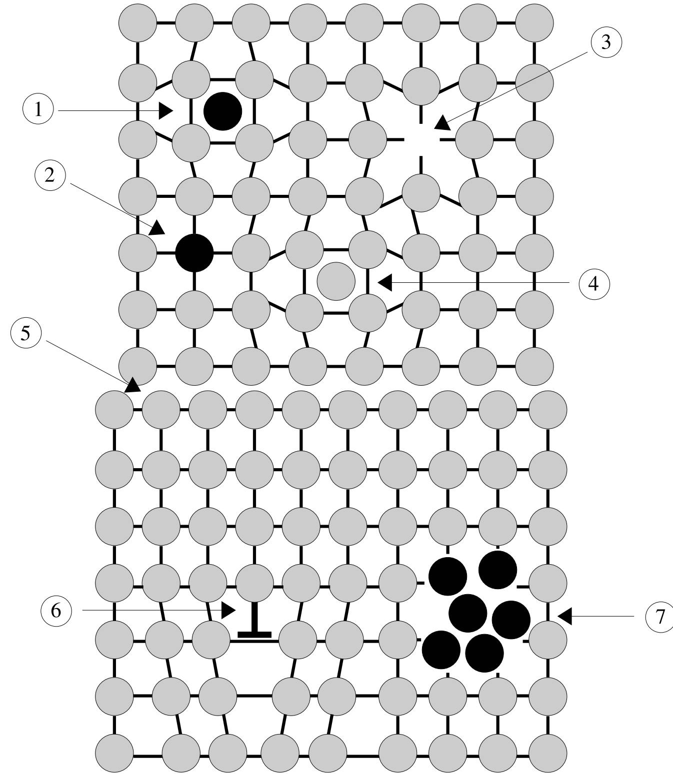

Figure 2.2: Crystalline defects. (1) Foreign interstitial, (2) Foreign substitution, (3) Vacancy, (4) Self-interstitial, (5) Stacking fault, (6) Edge dislocation, and (7) Precipitation. (Adapted from Reference [25]).

additional energy levels in the crystal structure and the surface states of semiconductor. Impurities that are localized in vicinity to the edges of the band are often referred as shallow-level impurities [27]. Similarly, impurities created and localized deeper in the band gap are known as deep-level impurity centers (or traps) [25]. Conductivity results as electrons are thermally excited from impurity levels to the conduction band [26].

Deep-level impurities in semiconductors create additional discrete energy levels that acts as generation-recombination centers, where electrons (from the conduction band or the valence band) are generated and recombined in the bandgap. In the case where there are excess charge carriers, the energy level is referred to as a recombination center. On the other hand, when the density of charge carriers is below an equilibrium state, the energy level acts as generation center. Figure 2.3,

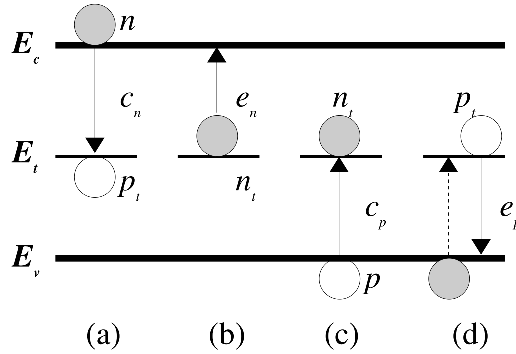

Figure 2.3: Energy level diagram for a deep-level impurity (Adapted from Reference [25]).

adapted from Reference [25], shows four possible scenarios demonstrating electron capture and emission processes at deep energy levels. The impurity energy level is denoted as E_t in the figure. There are n electrons in the conduction band (in units of electrons/cm^3) and p holes in the valence band (in units of holes/cm^3). Consider the recombination event shown in Figure 2.3a. An electron is captured from conduction band to the energy level, this process is denoted by the capture coefficient c_n. Two events could happen as a result of an electron being captured. An electron could be emitted back to the conduction band, known as electron emission e_n (Figure 2.3b). The other scenario is capturing an electron from valence band, this is denoted by c_p in Figure 2.3c. A hole is then left at the energy level. Again, a hole can be emitted back to valence band, e_p, or an electron will be captured (Figure 2.3d). The events that take place at generation-recombination center (or trap) will depend on the impurity energy level (E_t), Fermi level, temperature, and capturing cross-sections of the impurity [25].

2.2.3 Surface states

Impurity levels (shallow or deep) are resulted from foreign atoms or defects in the crystal lattice. Energy states for impurity levels may be localized in the forbidden gap. Localized energy in the forbidden gap may also result from surface states of a semiconductor which is most important for the present work. Surface states may

be formed from surface imperfections or foreign atoms on the surface. Depending on the population of surface atoms, the energy levels may be continuous if the atoms are densely distributed across the semiconductor surface, or discrete if the atoms are scarcely distributed. For a clean semiconductor surface, a continuous energy distribution is expected [26, 28].

At the surface of a semiconductor, there exists of a space-charge region. This region may come about due to the preferential adsorption of positively or negatively charged ions, or the alignment of absorbants due to electrical dipole moments [28, 29]. These surface states induced by the presence of atoms on the surface of the materials, can be modeled by quantum wave functions. Many models are used to discuss this complex band structure, including: there are the *nearly free electron* model, *tight-binding* approximation, *virtual gap states* model, and *electronegativity concepts* [29]. The derivation and calculation of surface states are beyond the scope of this work. However, future work on the QF^{TM} sensor chips should address the energy states on the semiconductor surfaces. Such that, one could theoretically and experimentally predict the energy states from atoms on the substrate surfaces.

Here, the physical process on the substrate surfaces will be described by a phenomenon known as adsorption. Atoms and molecules could form weak or strong bonds with surface atoms of another material. Depending on the forces between atoms and molecules with the surface, this process can be categorized to as physisorption and chemisorption [30]. Physisorption is a weak force of adsorption on solid surfaces. The adsorbant and surface do not bind by chemical bonds, but rather, van der Waals force [31]. As the adsorbant comes in proximity with the surface, the force is related to polarization of molecules from quantum mechanical fluctuations of the electron clouds. Binding energies of physisorption are typically less than 0.3 eV and the atom-surface distance is in the range of 3-10 Å [30]. Chemisorption is the interaction of an adsorbed molecule with the surface by means of chemical bonding. Chemisorption is characterized with binding energies in the

range of a few eV, the equilibrium distance is around 1-3 Å, shorter than that of physisorption [30].

2.3 Metal contacts on semiconductor substrates

In the following sections, metallization for silicon, 4H-silicon carbide and sapphire will be discussed. Ideal metal contacts would have the following properties: low contact resistance, good metal-semiconductor adhesion, thermal stability, a bondable top layer and, smooth surface topology [32]. The dopant concentration in the semiconductor will also influence carrier transport across the metal-semiconductor interface; where the probability of carrier tunneling through the barrier could be increased [16]. The recipes for the metal contacts fabricated for this have been developed from existing empirical data published in the literature; where some of these are presented later in this section for silicon, 4H-SiC and, sapphire.

2.3.1 Schottky barrier and contact formation

Metal and semiconductor contacts contribute to the functionality of electronic-semiconductor devices. When a metal comes in contact with a semiconductor, a potential barrier will be formed at this interface due to differences in work functions, temperature, Fermi levels, and dopant concentrations of the semiconductor.

A Schottky barrier is usually formed between a metal and a semiconductor interface. The magnitude of the barrier is determined by the amount of charge carriers transported across metal-semiconductor interface, and hence, influences the capacitance behavior of the device [27]. The potential barrier that arises between a metal and a semiconductor typically results in a rectifying behavior.

The work function of a metal (ϕ_m) is defined as the energy required to raise an electron above the Fermi level. Similarly, the work function of a semiconductor (ϕ_s) is the energy difference between the Fermi level and the energy to raise an electron to the semiconductor surface (in vacuum) [33]. To illustrate some of

the various barrier formations, schematic diagrams for energy bands are shown in Figure 2.4(a) through (d), adapted from References [33] and [27]. In Figure 2.4(a), the energy bands for an n-type semiconductor and a metal are depicted. The two materials are separated and under vacuum and the work function of semiconductor is less than that of metal. If the two are connected electrically with a wire, as seen in Figure 2.4(b), a thermal equilibrium will be reached. Though Fermi levels for the metal and the semiconductor are initially different, the two levels will reach an equilibrium where both are at the Fermi level of the metal. As shown in Figure 2.4(b), the work function of metal ($q\phi_m$) is equivalent to the electron affinity of semiconductor ($q\chi_s$) combined with the energy difference ($q\phi_n$) between the conduction band ($\mathbf{E}_C$) and the Fermi level ($\mathbf{E}_{F,s}$). The potential difference is therefore the contact potential between the two materials' work functions, $\phi_m - (\chi_s + \phi_n)$ [27]. Note that in Figure 2.4 (b) and (c), the major difference between the metal and the semiconductor is the gap distance (δ), a parameter determined by physical distance of the contacting material. As this distance decreases, negative charge will be built up on the metal surface while an equal positive charge will be built up in the semiconductor depletion region [27, 33]. A depletion region is formed between the metal contacts and the n-type semiconductor when the shallow donors are ionized at room temperature. A positive space charge resides in this region, which is depleted of electrons on the semiconductor side [33]. An ideal case for a metal-semiconductor contact is illustrated in Figure 2.4 (d). The contact potential (V) is given by $V = \delta \mathscr{E}_i$, where δ is the gap between the metal and the semiconductor and, $\mathscr{E}_i$ is the electric-field strength at the interfacial layer. As this gap diminishes, the contact potential will approach zero and the gap will become negligible to the electrons [33]. When this happens, the potential difference between the metal and the semiconductor is separated by a small potential barrier with a potential of $q\phi_{bn} = q\left(\phi_m - \chi_s\right)$ [27,33]. This would allow charge carriers to transport through the potential barrier. In Table 2.2, properties for some of the

selected metals are tabulated.

Table 2.2: Properties of metals used in metallization. [32–34]

Metal	Density (g cm^{-3})	Work Function (eV)	Resistivity x 10^{-6} ($\Omega \cdot$ cm)	Thermal Expansion Coefficient (10^{-6} K^{-1})	Melting Point (°C)
Al	2.70	4.18	2.65	23.10	660.32
Ag	10.50	4.42	1.59	19.00	961.78
Au	19.30	5.20	2.35	14.00	1064.18
Cu	8.96	4.59	1.67	17	1084.62
Ni	8.90	5.15	6.84	13	1455.00
Pd	12.00	5.17	10.80	11.80	1554.80
Pt	21.50	5.43	10.60	9.00	1768.20
Ti	4.51	4.33	–	8.60	1668.00
W	19.25	4.55	5.65	5	3422.00
Zr	6.52	4.05	–	5.70	1854.70

2.3.2 Contact resistance measurements

Current flow can be measured across a metal-semiconductor contact, this is depended upon the applied voltage, barrier height, and doping density of semiconductor. The contact resistance can be measured by using a two-point probe or a four-point probe approach. These methods can indirectly determine the *specific contact resistivity*, ρ_c ($\Omega \cdot cm^2$). For practical purposes, the total resistance can be measured directly [25].

The basic theory regarding bulk material resistivity measurement is described in the following. The electric field $\mathscr{E}$ is related to current density J, resistivity ρ,

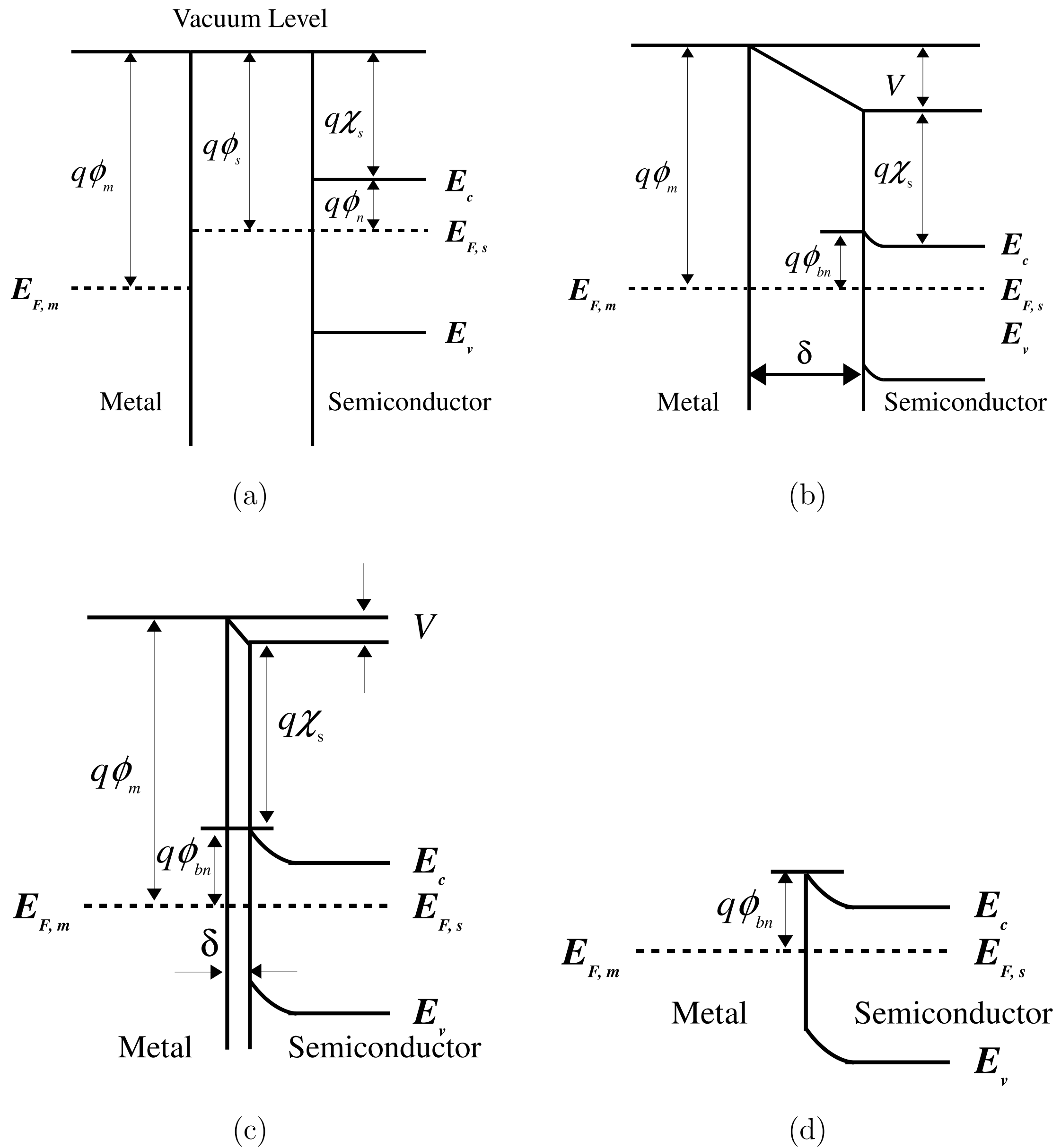

Figure 2.4: Various types of barriers formed at metal and semiconductor interfaces: (a) isolated contacts separated by a vacuum, (b) electrically connected but separated by a gap, (c) reducing of the gap, and (d) when the gap is essentially negligible [27, 33].

and voltage V by [25],

$$\mathscr{E} = J\rho = -\frac{dV}{dr}. \tag{2.1}$$

Here, the current density is expressed as,

$$J = \frac{I}{2\pi r^2}, \tag{2.2}$$

where r is the distance between some arbitrary point in the bulk and the probe. The voltage output is therefore,

$$\int_0^V dV = -\frac{I\rho}{2\pi}\int_0^r \frac{dr}{r^2} \Rightarrow V = \frac{I\rho}{2\pi r}. \tag{2.3}$$

The bulk resistivity measured with a two-point probe is

$$V = \frac{I\rho}{2\pi r_1} - \frac{I\rho}{2\pi r_2} = \frac{I\rho}{2\pi}\left(\frac{1}{r_1} - \frac{1}{r_2}\right), \tag{2.4}$$

where r_1 and r_2 are distances to the probes (see Figure 2.5). The resistivity is,

$$\rho = 2\pi\frac{V}{I}\left(\frac{1}{r_1} - \frac{1}{r_2}\right)^{-1}. \tag{2.5}$$

The two-point probe measurement method for metal-semiconductor contact will be discussed. The total resistance, $R_T = V/I$, measured across two contacts is given as [25, 32],

$$R_T = R_{SH}\frac{l}{W} + 2R_C, \tag{2.6}$$

where R_{SH} is the sheet resistance, l is the distance separating the two contacts, w is the width of the contact, and R_C is the contact resistance. Figure 2.5 shows the contact resistance structure from cross-section and top view for the two-point probe method.

For four-point probe measurement, the most common arrangement of probes is in a linear array. It is an array of four equally spaced probes, S ($\mathrm{S} = \mathrm{S}_1 = \mathrm{S}_2 = \mathrm{S}_3$). Typically, the outer two probes are for current conduction and the voltage is measured by the inner two probes [25]. The voltage measured can be expressed as

$$V = \frac{I\rho}{2\pi}\left(\frac{1}{S_1} - \frac{1}{S_2 + S_3} - \frac{1}{S_1 + S_2} + \frac{1}{S_3}\right), \tag{2.7}$$

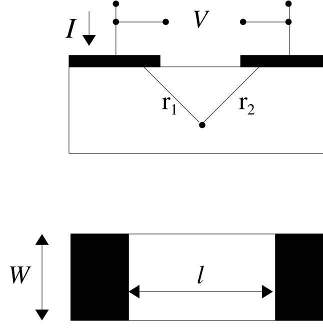

Figure 2.5: A schematic of two-point probe setup with cross-section and top view.

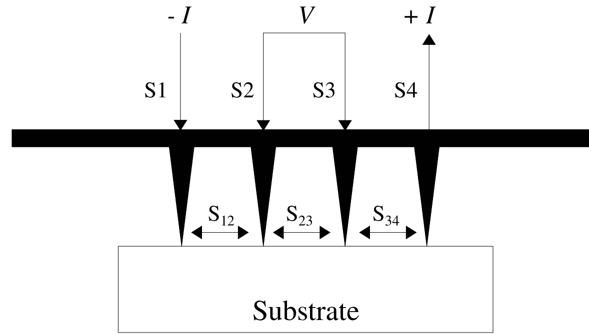

Figure 2.6: Schematic of a four-point probe setup.

where the resistivity, ρ, is,

$$\rho = \frac{2\pi}{(1/S_1 - 1/(S_1 + S_2) - 1/(S_1 + S_2) + 1/S_3)} \frac{V}{I} = 2\pi s \frac{V}{I}. \tag{2.8}$$

A schematic of a four-point probe configuration is shown in Figure 2.6. The influence of instrumentation to contact resistance can be reduced with four-point probe method, since a constant current flow goes though probe number 1 and 4. If there is resistance, a potential drop will be noticed at probe number 2 and 3 by the voltmeter. However, the use of a high impedance voltmeter will also help minimize this problem (see Figure 2.6).

2.3.3 Formation of ohmic contacts

An ohmic contact for an electronic device refers to an electrical contact between a metal and a semiconductor, that has negligible resistance in comparison to total resistance of the device. Such that the voltage drop across the metal-semiconductor interface will not lead to loss of current transport. Current-voltage characteristics

for an ohmic contact exhibits a linear or quasi-linear behavior in both directions of biasing voltage. Whereas, contacts with rectifying characteristics (i.e. a Schottky barrier) exhibit non-linear behavior [11]. The contact resistance is depended upon dopant concentration, contact dimension, uniformity and cleanliness of contact surface [35]. The specific contact resistance (R_c) can be defined by the equation [27]:

$$R_c = \left(\frac{\mathrm{d}V}{\mathrm{d}J}\right)_{V=0} \tag{2.9}$$

Theoretically, ohmic contacts are the result of tunneling of electrons and holes over the barrier at the interface. A good ohmic contact should have specific resistance in the range of 10^{-7} $\Omega\cdot\mathrm{cm}^2$, if not less [33]. Though experimental data have shown that the actual specific contact resistance for these contacts are typically a few orders of magnitude larger than the theoretical predicted values. The discrepancy is due to the loss of scattered incident electrons at the interface, where only a portion of electrons will tunnel through the potential barrier [36].

The resistivity of a sample can potential affect the Q-DLTS measurement. And therefore, the contact resistance should be measured. The contact resistance can be studied using the transmission line model (TLM) method. By measuring the resistance across a series of metallized contacts (using two-point probe), this model is useful for derivation of optimal contact resistance. For a sample with low contact resistance, a filling pulse may not be able to completely fill the trap centers due to the low impedance.

2.3.4 Ohmic contacts on n-type Si

Several metals have been previously studied to demonstrate Ohmic contacts on silicon substrate which include: aluminum, platinum, nickel, and gold. Some of these are included blow in Table 2.3.

Table 2.3: Several examples of ohmic contacts to silicon from the literature.

Material	Metal	Deposition method (Thickness)	Annealing condition	Contact resistance ($\Omega \cdot cm^2$)	References
n-type Si	Ni	Electroless plating (Catalytic reduction of Ni)	NA	NA	[37]
Si	Pt	Cathodic Sputtering (70 nm)	700°C 5 to 10 minutes	NA	[38]
n-type Si	Pt	Chemical vapor Deposition	700°C 5 to 10 minutes	NA	[39]
n-type Si	Al	E-beam evaporation	450°C	9.0 x 10^{-7}	[40]

NA – not available

2.3.5 Ohmic contacts on 4H-SiC

Undoped SiC crystals are by default n-type materials because of the presence of nitrogen introduced during crystal growth. The conductivity of SiC can be adjusted to n-type or p-type by incorporating donors or acceptors during crystal growth and/or by using ion implantation [41]. There are several articles published in the literature that have provided a comprehensive review for ohmic contacts to 4H-SiC [42–45]. In this section, the details for various metalizations and considerations will be discussed.

Several formulations for ohmic contacts have been examined for SiC in general, these include Cr-, Ni-, Ti-, and Ta-based metals [44, 46, 47]. The earliest work reported on ohmic contacts to n-type SiC was done using Cr and five weight percent (minimum) Cr alloys containing Fe, Ni, and Fe-Ni. Ohmic contacts were observed when the metals were subjected to heat treatment in the range of 1500°C to 1900°C [46]. However, the specifications on the metal thickness, annealing time, contact

resistivity and chemical reactions between the materials were not given. The use of Ni is widely use for SiC, although the non-rectifying characteristic of ohmic contacts are not typically observed until after a post-deposition annealing process, at temperatures between 900°C and 1000°C [43, 44]. The onset for formation of silicides is typically present at low temperature annealing (250°C to 400°C) [48]. The Schottky barrier decreases from heat treatment with increasing temperature due to annealing. A possible explanation for ohmic contacts could be due to the composition of the silicon and carbon at the interface. It was noted by Han and Lee [49], that with elevated temperature, the carbon atoms diffuse toward the surface of semiconductor after silicidation. The authors [49] theorized that carbon vacancies are created below the metal contact, and that these vacancies act as donors for the electrons, thus improving the net electron concentration and decreasing the width at space-charge region. Another explanation for an ohmic contact on SiC is due to the presence of an inhomogeneous Schottky barrier at the nickel silicide and SiC interface. At this region, the current transport occurs preferentially across the lower potential barrier due to surface topography [50, 51]. It is important to note that packaging issue arise for SiC with Ni layer. Typically a layer of Au is deposited on top of the Ni to provide bonding for practical device fabrication. Table 2.4 summarizes some of the metalizations that have shown ohmic characteristics with n-type 4H-SiC.

Table 2.4: Ohmic contacts to n-type 4H-SiC.

Material (Doping, conductivity type)	Metal	Deposition method (Thickness)	Annealing condition	Contact resistance ($\Omega \cdot cm^2$)	References
n-type α-SiC	Cr	Melting	NA	NA	[46]
n-type 4H-SiC	Ni	Evaporation (200 μm)	700 to 900°C	2.8×10^{-3} to 6.5×10^{-4}	[47]

Continued on Next Page...

Table 2.4 – Continued

Material (Doping, conductivity type)	Metal	Deposition method (Thickness)	Annealing condition	Contact resistance ($\Omega \cdot cm^2$)	References
n-type 4H-SiC	Ni/W	NA	1000 to 1050°C	NA	[52]
n-type 4H-SiC	Ni/Ti/W	NA	1000 to 1050°C	NA	[52]

NA – not available

2.3.6 Metal contacts on sapphire

Metallization to sapphire can be somewhat more challenging than just metal to semiconductor contacts. The properties of sapphire are between that of a ceramic and semiconductor which make it difficult for metal to bond to, and thus, form electrical contacts. Metallization for sapphire, or aluminum oxide (Al_2O_3) would preferentially require metals that can form oxides to obtain a stronger adhesion. During the sintering process, oxygen migration between the two surfaces would allow for better bonding.

Several studies have been published for metallization to sapphire substrates. Some of the metals studied include: Al, Ti, Zr, Cu, Pt, and Ag. Otsuka [53] had demonstrated the feasibility of good bonding of Al to sapphire. The bonding strength and electrical resistivity were examined for evaporation of Al at temperatures of 100°C and above 200°C. It was observed at 100°C, that the evaporated aluminum had high electrical resistance. This was due to possible inadequate coverage of aluminum and insufficient oxygen interdiffusion for adhesion. At temperatures above 200°C, the migration of aluminum to the substrate during evaporation and the interdiffusion oxygen was observed. Which lead to better metal adhesion [53]. In the study by Suenaga [54], thin film deposition of Ag, Cu, and Ti metal layers were studied. Two metallization recipes were sputtered onto single crystal sap-

phire, Ag/Cu/Ti (540/245/72 nm) and Cu/Ag/Ti (245/540/72 nm). The samples were heat treated in temperatures ranging from 673K to 973K, followed by analysis of the reaction products by the x-ray diffraction (XRD) method. The diffusion of the Cu to Ag and towards the Ti layer was observed for the formulation - Cu/Ag/Ti - Al_2O_3 at temperatures above 723K. As for the formulation - Ag/Cu/Ti - Al_2O_3, several compounds were observed after annealing, CuTi, Cu_4Ti_3, and Cu_3Ti. After annealing at 973K, Cu_3TiO was observed to be present for both metallization recipes. This compound was formed by oxidation of Cu_3Ti, which was believed to enhance the bonding of Ag-Cu to the sapphire substrate [54]. An improvement in the performance of Zr and Ti adhesion to a Pt metal layer was demonstrated on a sapphire substrate by Bernhardt and co-workers [55]. Their investigations have shown that Zr exhibits better bonding after annealing in comparison to Ti. Analytical techniques were performed using XRD, AES (Auger electron spectroscopy), and SIMS (secondary ion mass spectroscopy) to study the composition. For Pt on Ti, after annealing between 450 to 500°C, the Ti diffuses into Pt and oxidizes, which leads to degradation of the metal layers and results in delamination of Pt with substrate. No migration of Zr to Pt was observed, and it was suggested by the authors that using Zr as adhesion layer would be better at minimizing delamination.

Table 2.5: Metal contacts to sapphire.

Material	Metal	Deposition method (Thickness)	Annealing condition	Contact resistance ($\Omega \cdot cm^2$)	References
Sapphire	Al	E-beam evaporation (4 μm)	NA	NA	[53]
Sapphire	Ag/Cu/Ti	Magnetron sputtering (540/245/72 nm)	400, 450, 500, 600, and 700°C	NA	[54]

Continued on Next Page...

Table 2.5 – Continued

Material	Metal	Deposition method (Thickness)	Annealing condition	Contact resistance ($\Omega \cdot cm^2$)	References
Sapphire	Cu/Ag/Ti	Magnetron sputtering (540/245/72 nm	400, 450, 500, 600, and 700°C	NA	[54]
Sapphire	Zr/Pt	E-beam evaporation (20/300 nm)	450 to 850°C	NA	[55]
Sapphire	Ti/Pt	E-beam evaporation (20/300 nm)	450 to 850°C	NA	[55]

NA – not available

2.4 Application of Q-DLTS system for sensor

2.4.1 Systems for the characterization of deep-level impurities

As described in the previous sections, deep-level impurities can be caused by inherent defects or foreign atoms which have adhered onto the surface of a semiconductor. To understand and identify these deep-level energy centers, this section will focus on introducing methods to characterize the deep-level energy centers.

Earlier characterization for deep-level energy centers was done by means of thermal and optical methods, such as the thermally stimulated current (TSC) method, the thermally stimulated capacitance (TSCAP) method, and luminescence [56]. In addition, static measurements such as capacitance-voltage (C-V) and current-voltage (I-V) methods can also be used, although they are commonly used for shallow-level impurities [25]. To characterize deep-level impurities, transient measurements are examined, which can better demonstrate the time-varying characteristics of the charge carriers. Some of the characterization methods for deep-level impurities are summarized in Table 2.6. The details of each of these

characterization methods will be discussed in the following sections.

Table 2.6: Summary of capacitance, current, and charge deep-level transient spectroscopy measurement methods.

Reference	First Author	Year	Characterization Method	Scanning Method
[1]	Lang	1974	Deep-Level Transient Spectroscopy (DLTS)	Thermal
[57]	Wessels	1976	Current Transient Spectroscopy	Thermal
[2]	Kirov	1981	Charge Deep-Level Transient Spectroscopy (Q-DLTS)	Thermal
[58]	Farmer	1982	Charge Transient Spectroscopy (QTS)	Thermal
[59]	Arora	1993	Charge Deep-Level Transient Spectroscopy (Q-DLTS)	Isothermal

2.4.2 Capacitance transient measurements

Capacitance transient measurements are commonly used for obtaining information on impurity level in the depletion region of a Schottky barrier and also at the p-n junction. In this approach, an initial pulsed bias is applied, followed by observing the spectral transients as the charge carriers return from a non-equilibrium to thermal equilibrium state.

The deep-level transient spectroscopy (DLTS) was first proposed by Lang [1], a capacitance transient thermal scanning technique. DLTS used a dual-gated integrator or double boxcar approach, allowing one to set emission rate window. The capacitance transient is only observed when it falls in this rate window. The maximum rate window is on the order of 10^5 sec^{-1}, but technically there is not a lower limit. According to Lang [1], it is inconvenient to go below 1 sec^{-1}. By averaging

the signals, it gives a significant advantage for signal-to-noise ratio enhancement, especially when detection trap centers are low in concentration. In comparison to thermally stimulated current (TSC) method, the DLTS technique is low in noise, low in leakage current, and is better for identifying majority and minority carriers. DLTS is also more versatile than the thermally stimulated capacitance (TSCAP) method since it has a better sensitivity and a greater range for the observable trap depths [1].

The basic concept for DLTS is similar to that of capacitance measurements – to obtain information on impurity levels in the space charge region of p-n junction or Schottky barrier. An initial non-equilibrium state will be induced by a pulsed bias, and the transient phenomenon is observed as occupation level of charge carriers return (decay) to thermal equilibrium. The transient decay is a function of temperature, and the presence of traps are indicated by peaks, when plotted temperature versus capacitance (normalized to arbitrary units). The height of these peaks are proportional to their trap concentrations. The change in capacitance is due to the pulsed bias, which introduces charge carriers, and thus changes the number of electrons residing in the traps. The signs (positive or negative) of capacitance change are dependent upon the presence of electrons in the traps; whether the concentration had increased or decreased due to the applied pulse. For a p-type material, an increase in trapped minority carriers (electrons) results in capacitance increase and thus, positive peaks are observed [1].

A key feature of DLTS is the ability to vary rate window by carrying out a series of thermal scans. As mentioned previously, the double boxcar approach determines the rate window and by varying the temperature, responsive peaks of emission rates will be seen in the window. The thermally excited emission rates can be shown as:

$$e_1 = \left(\sigma_1 \left\langle \nu_1 \right\rangle N_{D1}/g_1\right) \exp\left(-\Delta E/kT\right), \tag{2.10}$$

where e_1 is the emission rate of minority carriers (electrons), σ_1 is the capture

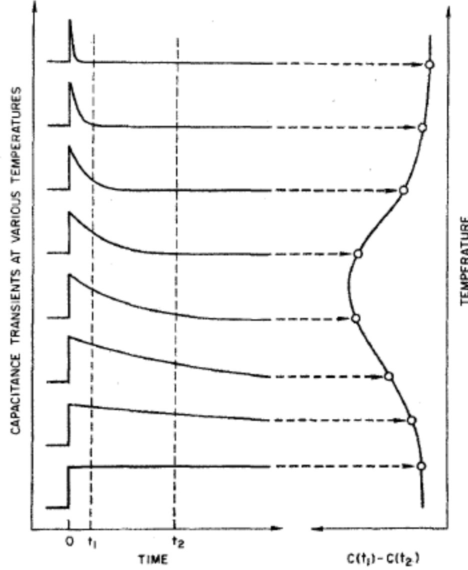

Figure 2.7: Relationship between double boxcar approach and corresponding DLTS signal. Capacitance transient measurements are taken at different times as a function of temperature [1].

cross-section for minority carriers, $\langle \nu_1 \rangle$ is the mean thermal velocity of minority carriers, N_{D1} is the effective density states, g_1 is the degeneracy level of trap centers, ΔE is the energy separation between trap centers and minority carrier band, k is the Boltzmann constant, and T is the temperature. The relationship between the double boxcar and the corresponding DLTS signals are illustrated in Figure 2.7.

As seen in the Figure, a rate window is specified on the time scale at t_1 and t_2. The capacitance transient measurements are made within the rate window over a temperature range. The emission rate is very small at lower temperature, but the decay is more rapid as temperature increases. The transient signals are fed into the DLTS system with window set at t_1 and t_2. As shown in Figure 2.7, each point on DLTS signal is calculated as the capacitance difference at t_1 and t_2. The normalized signal, $S(T)$, is therefore defined as:

$$S\left(T\right) = \left[C\left(t_1\right) - C\left(t_2\right)\right] / \Delta C\left(0\right), \tag{2.11}$$

where $\Delta C\left(0\right)$ is the change in capacitance at time $t = 0$. This expression can be

represented in an exponential form as:

$$S\,(T) = \exp(-\mathrm{t}_1/\tau) - \exp(-\mathrm{t}_2/\tau) \tag{2.12}$$

or as:

$$S\,(T) = \exp(-\mathrm{t}_1/\tau)\,[1 - \exp(-\Delta \mathrm{t}/\tau)] \tag{2.13}$$

where $\Delta t = t_2 - t_1$, and $\tau_{\max}$ is obtained by differentiating $S(T)$ with respect to τ. $\tau_{\max}$, where the time rate window is then:

$$\tau_{\max} = (t_1 - t_2)\,[\ln(\mathrm{t}_1/\mathrm{t}_2)]^{-1}\,. \tag{2.14}$$

By varying the time rate window and the temperature, $\tau_{\max}$ can be calculated from Equation (2.14), which corresponds to the activation energies of the traps. This would then allow one to plot an Arrhenius plot (if needed), based on logarithmic scale of emission rate versus $1000/T$. The emission rate of a trap was described in equation 2.10.

2.4.3 Current transient measurements

For current transient measurements, the current-time signal represents integration over time of the total charge emitted from trap centers. Current transient measurements are useful for devices like small-geometry MOSFETs, where lower capacitance is typically encountered. The presence of deep-level impurities can be detected by pulsing the voltage and observing current as it drains as a function of time [25]. Current transient measurements can be more complicated because of various components, such as, the emission current I_e, displace current I_d, and junction leakage current I_j. The emission current is defined as [25]:

$$I_e = qA \int_0^W \frac{dn}{dt} dx, \tag{2.15}$$

and the displacement current is [25]:

$$I_d = qA \int_0^W \frac{dn_T}{dt} \frac{x}{W} dx, \tag{2.16}$$

where q is the electron charge, A is the area of sample, W is the width of space-charge region, $\frac{dn}{dt}$ is the electron density in conduction band's time rate of change, and $\frac{dn_T}{dt}$ is the rate of change at trap centers.

The first results reported using current transient measurements were by Wessels [57]. The detection of traps was based on combination of reverse recovery and thermal stimulated current measurements. Transient measurement was made for a copper-doped gallium phosphide diode. The diode was repeatedly pulsed, after each pulse current transient was measured at time t_1, followed by turning off the pulse for 10 nsec. The measured current transients can be expressed as [57]:

$$I = \frac{N(t)qA\Delta W}{2\tau_e}\exp\left(\frac{-\mathrm{t}_1}{\tau_\mathrm{e}}\right) \tag{2.17}$$

where $N(t)$ is the total number of filled traps, ${\tau_e}^{-1}$ is the emission rate, ΔW is the change in the width of the space-charge region, and t_1 is the time that current transient is sampled. By differentiating equation 2.17 with respect to τ_e, the maximum of current transient occurs at $\tau_e = t_1$. The emission rate is therefore governed by equation 2.10.

2.4.4 Charge transient measurements

Two groups have independently reported on the modification of capacitance-based DLTS to charge-based transient DLTS (Q-DLTS) [2,58]. Basic principles involving the two approaches will be discussed in the following paragraphs.

According to Kirov and Radev, a n-type Metal-Insulator-Semiconductor (MIS) capacitor was measured [2]. A reverse bias was initially applied, U_G, to deplete the space charge region, followed by a forward bias filling pulse. This resulted in an accumulation and filling of the electrons at the interface states. It was postulated that changes in the capacitance can be observed as the electrons (n_t) are emitted and return to a thermal equilibrium state. In the work by Kirov and Radev, capacitance change was observed in the form of charge difference. After initial filling of trap centers, electron concentration (n_t) at the conduction band decays

exponentially with time [2],

$$n_t = N_t e^{(-t/\tau)}, \tag{2.18}$$

where N_t is, t is time, and τ is

$$\tau = (\sigma_n \nu_{th} N_c)^{-1} e^{(E_t/kT)}. \tag{2.19}$$

Here, σ_n is the capture cross section, ν_{th} is the thermal velocity of electrons, N_c is density state at bottom of conduction band, and E_t is the depth for energy level measured from conduction band. In this technique, the electrical charge is measured at interval at time t_1 and time t_2. After the filling pulse, measurements are made at t_1 and t_2, and the Q-DLTS signals can be expressed as [2]:

$$\Delta Q_G(t_1 - t_2) = -\frac{qWN_t}{2}(1 + C_{SC}/C_0)^{-1}(e^{-t_1/\tau} - e^{-t_2/\tau}), \tag{2.20}$$

where C_{SC}/C_0 is the normalized capacitance measured. Essentially, equation 2.20 describes the exponential decay transient measured at t_1 and t_2. A simplified circuit diagram of the Q-DLTS system used in the study by Kirov and Radev. [2] is shown in Figure 2.8. The device under test (DUT) is connected either to the ground or to the amplifier. In Figure 2.9, K_1 and K_2 denote the switches that control flow path of electrical charge. K_1 is normally open while K_2 is normally closed. After a filling pulse, at time t_1, K_1 will be open and vice versa for K_2. At time t_2, the switches change their positions again before the next filling pulse comes in. An electrometer was used to measure signal as it exited the amplifier.

Farmer and co-researchers proposed another variation of charge transient spectroscopy, referred to as QTS. Similar to the approach first proposed by Lang [1], a reverse pulse bias (from a negative voltage to zero) was applied to a n-type Si diode. The space charge region's width collapsed, while the charge carriers were trapped at the deep-level centers within this region. Then, as a function of time and temperature, the charge carriers were emitted back to the original state. Here,

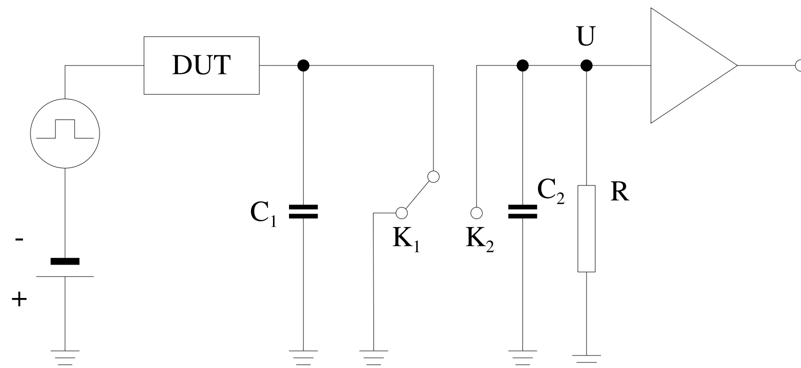

Figure 2.8: A simplified circuit diagram for Q-DLTS measurement (adapted from [2]).

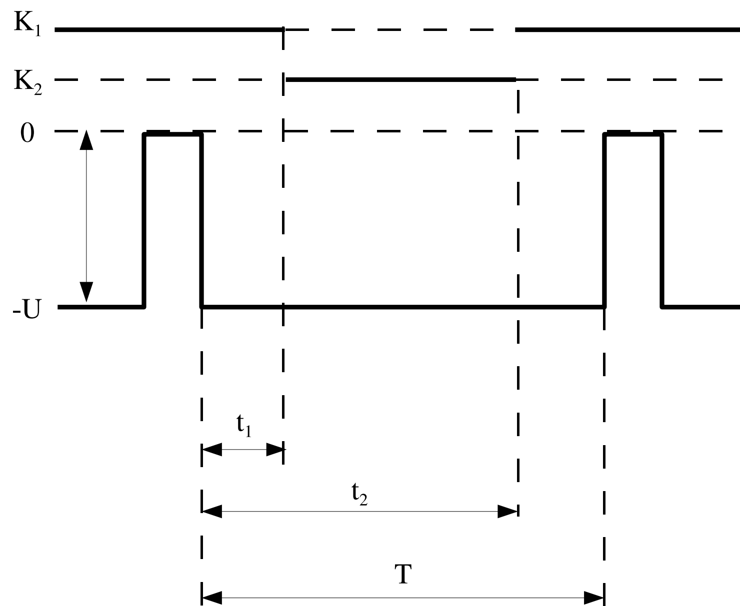

Figure 2.9: A diagram on sample collection's timing sequence (adapted from [2]).

one should note that this relaxation process can be observed through junction capacitance or current [58]. The current transient is expressed in the form,

$$i(t) = AqWN_T e^{t/\tau}/2\tau. \tag{2.21}$$

The equation above is essentially the same as equation 2.17. For a n-type material, τ, the current transient decay time constant, can also be defined as a thermal emission rate e_n with the following relationship,

$$\tau^{-1} = e_n = N_c \sigma_n \langle \nu \rangle e^{-(E_c - E_T)/kT}, \tag{2.22}$$

where N_c is the effective density in the conduction band, σ_n is the carrier capture cross section, $\langle \nu \rangle$ is the carrier thermal velocity, $(E_c - E_T)$ is the trap depth just below conduction band, K is Boltzmann's constant, and T is temperature. For the QTS method, the current transient can be expressed as:

$$q(t) = \int_0^t i(t')dt' = \frac{AqWN_T}{2}(1 - e^{-t/\tau}). \tag{2.23}$$

The integration of current of time is performed by a high-speed field-effect transistor operational amplifer. The circuit integrates the current from the diode into voltage, given as:

$$V(t) = \frac{AqWN_T R(e^{-t/RC} - e^{-t/\tau})}{2(RC - \tau)}, \tag{2.24}$$

where for $RC \gg \tau$,

$$V(t) = (AqWN_T/2C)\left[1 - e^{-t/\tau}\right]. \tag{2.25}$$

The RC circuit acts an integrator in this case, because the capacitor will not be completely charged due to insufficient time. The output voltage will roughly equal to voltage across the resistor. Following Ohm's law, one has

$$I = \frac{V_{in}}{R}, \tag{2.26}$$

where the current is equal to voltage in divided by the resistance. The voltage output can be denoted,

$$V_{out} = \frac{1}{C}\int_0^t I dt = \frac{1}{RC}\int_0^t V_{in} dt. \tag{2.27}$$

Essentially, equations 2.24 and 2.25 show $V(t) = q(t)/C$, meaning that output of the circuit is proportional to the integrated current, or charge transient [58].

Arora and co-researchers reported another Q-DLTS system design [59]. In their approach, cyclic forward bias pulses are applied to tin doped $Al_xGa_{1-x}As$. In the first part of a cycle, trapped centers are filled by the filling pulse (Figure 2.11a). Charges from trapped centers are then emitted as the bias pulse goes back to zero. The charges emitted are collected by capacitor C1 as shown in Figure 2.10. Voltage signals are controlled by the toggle switches TG 1 and TG 1' as shown in Figure 2.11b and 2.11c. TG 1 and TG 1' are opposite of each other, when one is open the other one will be closed; switches are open when voltage is high. The integrator circuit is composed of an operational amplifier (M1 in 2.10) and a current amplifier. Output from the integrator is a voltage signal, and is expressed as:

$$V(t) = \frac{Q(t)}{GC_I}, \tag{2.28}$$

where $Q(t)$ is the charge from the integrating capacitor C_I and G is the current amplifier's gain. The actual observation of charge signal is observed after a dead time, t_d, in order to avoid unwanted initial transient signals (Figure 2.11d). Figure 2.11e represents the total charge at the trapped centers as a function from t_0 to the end of one cycle. The Q-DLTS system output signal is obtained through a "Follow-and-Hold" circuit. The switches TG 3 and TG 4 from Figure 2.11(Ke3 and Ke4 in Figure 2.10) are timed to sample at varied scanning rate window. The Q-DLTS signal can be obtained using the expression:

$$S = Q(t_2) - Q(t_1) = GC_I[\nu(t_2) - \nu(t_1)]. \tag{2.29}$$

Similar to other DLTS methods, the emission rate is denoted e_n. The electrical charge from trapped emission is therefore a transient decay, expressed as,

$$Q(t) = Q_0(1 - e^{-e_n t}). \tag{2.30}$$

The Q-DLTS signal will be given by,

$$S = Q_0(e^{-e_n t_1} - e^{-e_n t_2}). \tag{2.31}$$

As mentioned earlier, a scanning rate window method is also incorporated in this work. The rate window is set for $\ln(t_2/t_1)/(t_2 - t_1)$, while the temperature is kept the constant. Furthermore, the ratio of t_1 and t_2 is also fixed such that $t_2/t_1 = \alpha$, while varying $(t_2 - t_1)$. As reported in the work by Arora et al., the maximum signal will correspond to the trap emission rate at a given temperature (T),

$$e_n(T) = \frac{ln\alpha}{(\alpha - 1)t_1}. \tag{2.32}$$

Substituting equation 2.32 back to equation 2.31, the Q-DLTS signal can be written as:

$$S_{max} = Q_0 \left(\alpha^{1/1-\alpha} - \alpha^{\alpha/1-\alpha} \right). \tag{2.33}$$

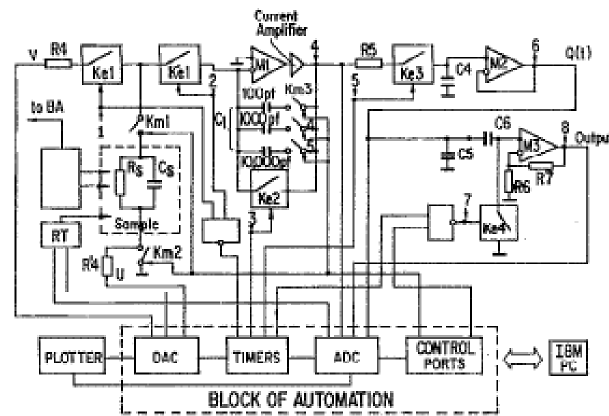

Figure 2.10: Circuit diagram of QDLTS system [59].

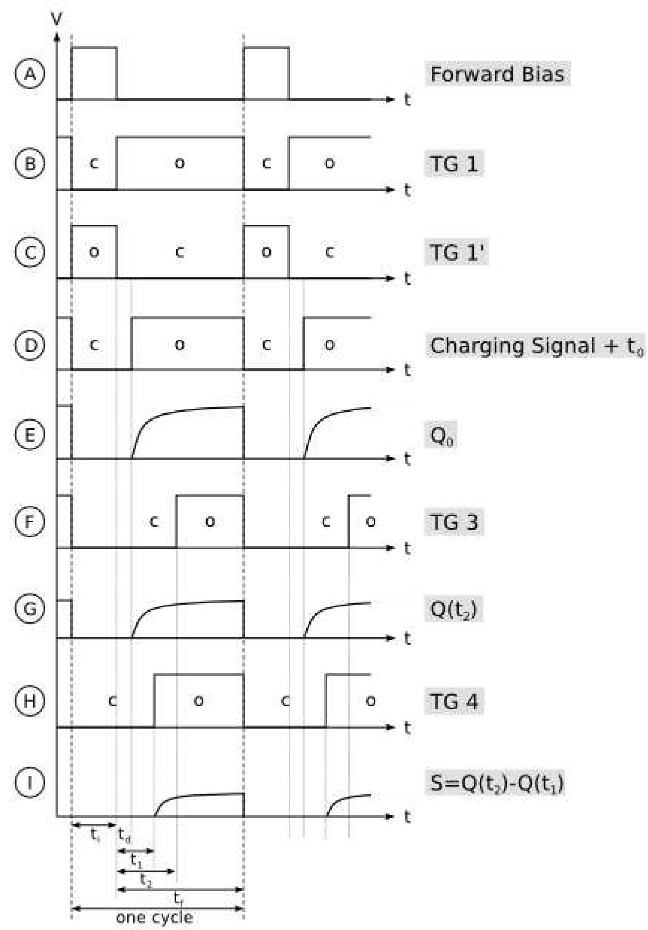

Figure 2.11: Time sequence diagram of signal input and output (adapted from [59]).

Chapter 3

Methodology

This section is organized to detail the process in which Quantum Fingerprint^{TM} sensor chips are fabricated. The methodology used in fabricating a sensor chip is in many ways adopted from procedures which currently exist in the semiconductor industry.

At the Nuclear Science and Engineering Institute Quantum Fingerprint^{TM} Fabrication Unit in University of Missouri (MU), at the sensor chip fabrication and testing facility has been designed and constructed to support this work. The facility incorporates equipment with capabilities for chip fabrication equipments (i.e. a sputtering machine, furnaces, and a wire bonder), surface cleaning accessories (chemical solutions and a plasma cleaner), a class 100 cleanroom, electrical and material characterization equipment (i.e. I–V, C–V, FTIR, Raman spectroscopy), two Q-DLTS devices, and sensor testing systems. In Figure 3.1, a summary of fabrication process is shown. In order to ensure both the consistency and the quality of the QF^{TM} sensor chips detailed in this work, the chips were all fabricated using the procedures detailed in the following sections of this chapter.

3.1 Material specifications

The materials selected for preliminary sensor development were silicon, 4H-SiC and sapphire. These materials are commercially available for purchase in the form of wafers as used commonly in semiconductor production. The two companies from

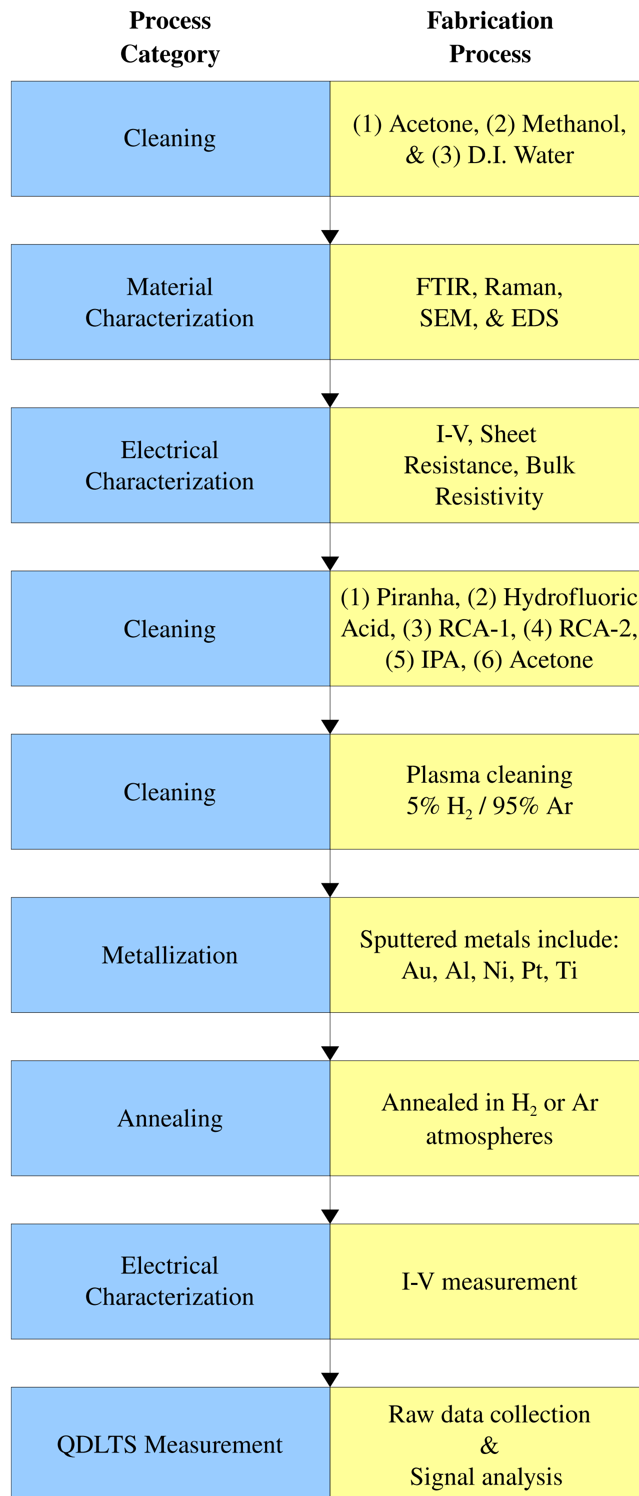

Figure 3.1: Process sequence for fabrication of a typical sensor chip.

which sensor materials were purchased from, were CREE, Inc. and University Wafer. CREE Inc. has been the leading manufacturer of SiC since 1987 and specializes in LED solid-state lighting, power-switching devices, and radio-frequency communication devices [60]. University Wafer is a supplier for bulk wafers in large and varieties and quantities [61]. The specifications from the manufacturers for the materials used in this work are shown in Table 3.1 for materials selected.

Both high and low doping concentration silicon wafers were purchased with the following specifications: N-type phosphorus doped silicon, 3" diameter, and resistivity of about 2 Ω· cm for highly doped wafers and about 20,000 Ω·cm for minimally doped wafers. The 4H-SiC wafers purchased have the following specifications, N-type 4H-SiC, 2" diameter, and resistivity of 0.139 Ω·cm. The sapphire wafers have the specifications of single crystal 2" diameter and C-plane orientation. Since the current design of the physical mask used in this work is about 1 cm by 1 cm, these wafers are then scribed using a diamond (or tungsten carbide) tip scriber to cut into appropriate sizes for making into sensor chips.

Table 3.1: Specifications of semiconductor materials used.

Material	Dopant & Concentration	Dimension & Orientation	Thickness (μm)	Resistivity (Ω·cm)
Si n-type	Phosphorus	3" (100)	350	2
Si n-type	Phosphorus	3" (100)	350	20000
4H-SiC n-type	Nitrogen	2" (0001)	350	0.139
Sapphire	–	2"(–)	430	–

3.2 Metal contacts on semiconductors

The methods of metal deposition used in this work will be discussed in this section. The topics presented here include: (1) material characterization – identification of material composition and topography, (2) electrical characterization – measurement of electrical properties of materials selected prior to metallization and after metallization, (3) substrate cleaning – substrate surfaces must be free of contaminants in order to ensure better adherence with metal contacts, (4) patterning – a physical mask is placed directly on top of the substrate to create desired pattern, and (5) metal deposition – depositing appropriate selection of metal and thickness to create Ohmic contacts.

3.2.1 Material characterization of semiconductors

To examine material characterization, the available systems at MU include Raman spectroscopy, Fourier Transform infrared spectroscopy (FTIR), scanning electron microscopy (SEM), and electron dispersive spectroscopy (EDS). The use of these techniques is to provide additional verification of the based material use for sensor chips.

The basic operating principle for both IR and Raman spectroscopies relies on the measurement of changes in the molecular vibrations between the bonds of atoms in a material. Based on the Hooke's law, the chemical bond holding the molecules of the material together, can be explained by simple harmonic motion. The vibrational frequency ν_0, in units of Hz, can be described by:

$$\nu_0 = \frac{1}{2\pi}\sqrt{\frac{k}{m}}, \tag{3.1}$$

where is the wave number and:

$$m = \frac{m_1 m_2}{m_1 + m_2}, \tag{3.2}$$

is the reduced mass in units of kg. The vibrational energy of a harmonic oscillator

E_{vb} can be defined as:

$$E_{vb} = h\nu_0 \left(n + \frac{1}{2} \right), \tag{3.3}$$

where h is Planck's constant and n is the vibrational quantum number that details Eigenstates of harmonic oscillator. In reality, oscillation between molecules (i.e. polyatomic molecule) is not harmonic, a better description can be approximated by:

$$E_{vb} = h\nu_0 \left[\left(n + \frac{1}{2} \right) - x_a \left(n + \frac{1}{2} \right)^2 \right], \tag{3.4}$$

where x_a is anharmonicity constant. Infrared spectroscopy measurements can be made in modes of absorption, transmission, and reflection of incident infrared beam. The absorption of infrared energy will induce transitions of a molecule from ground to an excited state, causing a shift in the wavelength specific to the selected material [62].

Raman spectroscopy is similar to infrared spectroscopy, both methods deal with vibrational frequencies of the specimen's molecular structure. The energy levels (ground state and excited state) of a molecule is usually separated by some energy $h\nu_M$, where ν_M is the frequency of molecular vibration. If an incident photon with energy $h_\nu L$ strikes the specimen surface, the photon can be scattered with a shifted wavelength. The frequencies of the photons scattered from the surface can be ν_L, $\nu_L - \nu_M$, and $\nu_L + \nu_M$. A scattered photon with a frequency of ν_L denotes elastic scattering (also called Rayleigh scattering) where, the energy transition starts and finishes at identical vibrational energy level. A frequency of $\nu_L - \nu_M$ denotes shifts from lower (ground state) to higher (excited state) vibrational energy level, also known as Stokes Raman scattering. For a frequency of $\nu_L + \nu_M$, the shift is from a higher to lower vibrational energy level, also known as anti-Stokes Raman scattering [62]. As the incident light interacts with molecule, energy change (lost or gained) will be characteristic of the chemical bond.

The scanning electron microscope (SEM) allows for characterization and observation of specimens at a nano meter to micron scales. Information such as element composition and surface topography can be obtained. The specimen is bombarded by a focused electron beam. In this process, the electrons lose energy due to scattering processes within a teardrop-shaped volume (or interaction volume) of the specimen. The extension of this interaction volume is about 100 nm to 5 μm beneath the surface, but the size of this interaction volume depends on electron's energy, specimen's density, and atomic number of the specimen. Interaction with the specimen creates secondary electrons, backscattered electrons, characteristic x-rays, and photons of various energies. There are specialized detectors that are capable of detecting these events. The signals are amplified and displayed as variations of brightness in a cathode ray tube (CRT). Raster scanning of the CRT display across the specimen surface corresponds to the electron beam and thus, the image display is an intensity map from the specimen [63]. Another mode of operation for the SEM is electron dispersive spectroscopy (EDS). In this method, an electron beam interacts with the specimen by ionizing the inner shell electron. Auger electrons and x-rays are created as a result. The x-rays produced in this process are characteristic for the materials in which they are created and can readily be measured with the specialized detectors.

3.2.2 Electrical characterization of semiconductors

Since the resistance and capacitance of semiconductor contacts can vary substantially for each individual chip produced, it is critical to measure and characterize these properties for every chip made. More specifically, one examines the ohmic contact of a substrate by current-voltage measurement. And resistivity measurements using a four-point probe.

The current-voltage measurement for an ohmic contact looks at the linearity and symmetrical response of current versus voltage under both forward and reverse

bias. In this work, measurement were made with an Agilient E5272A ammeter and a custom visual basic code was written to provide communication between the device and a desktop computer. Resistance was measured using a two-point probe approach, in which two fine needles were pressed onto the substrate metallization. This technique measures the total resistance, including contributions from sheet resistance (R_{SH}) and contact resistance (R_C). Details on the two-point probe approach can be found in Chapter 2 of this work. The current-voltage measurements were made before and after each sample was metallized to identify changes in resistivity after metallization.

A four-point probe was also incorporated for resistivity measurements. The four-point probe was purchased from Jandel Engineering and has a hand-held probe with a test unit. The four probes are made out of tungsten carbide, and are equally spaced at 1 mm apart in a linear array. The test unit, model number RM3-AR, has a current source providing selectable current from 10 nA to 100 mA. The test unit included PC control softare, where measurements can be output for current/voltage, sheet resistance, and bulk resistivity [64].

3.2.3 Substrate cleaning

Contaminants on substrate surfaces are problematic to electronic devices. Generally, sources of contaminants can be categorized into the following types: (1) particles, (2) metallic ions, (3) chemical residues, (4) bacteria, and (5) airborne molecular contaminants [65]. Problems involving the contaminants could lead to changes in device dimensions, surface cleanliness, surface topography, performance, reliability, and functionality [65]. A few of these sources are listed in Table 3.2. To ensure quality and performance of the sensor chips and reduce the possibility of contamination, it is critical that stringent fabrication procedures are documented and followed.

Table 3.2: Sources of substrate surface contaminants.

Problem	Description
Contaminants	(1) Particles: dead skin, hair, personnel generated particles (2) Metallic ions: metal ions that exist in the semiconductor material (3) Chemicals: processing chemicals and water (4) Bacteria (5) Airborne particles and humidity

The procedures used for substrate cleaning in this work were adapted from the widely used RCA (Radio Corporation of America) cleaning method. In 1965 while working at RCA, Werner Kern developed wafer cleaning steps to standardize the procedures. The objectives for this method are: (1) removal of organic layer, (2) removal of oxide layer, and (3) removal of ionic layer. There are however, several versions of the RCA cleaning method currently used. A modified cleaning procedure has been used in this research which involves changes in the chemical mixing ratio and order of steps. Typically in the semiconductor industry, wafer cleaning is automated due to handling of large quantities. Since the cleaning steps performed in this work have been conducted in a laboratory environment, chemical solutions were diluted to avoid potential hazard and etching to the substrate surface. The primary chemical used was de-ionized (DI) water, in which ionic contaminants have been removed through filtration, was used as a diluent, cleaning and rinsing substrates. Procedures implemented in this research are discussed in the following paragraphs [66].

1. A mixture known as Caro's acid (also known as piranha) was used. First to remove organic materials, such as photoresist and other visible organic contaminants. Caro's acid is typically composed of a mixture of sulfuric acid (H_2SO_4) and hydrogen peroxide (H_2O_2) where the mixture ratio can vary from 2 to 4:1. When these chemical solutions are mixed at room temperature, there is an exothermic reaction. Boil substrate at 130°C for about 10 to 15

minutes follow by rinsing with de-ionized (DI) water. An additional five minutes of ultrasonic bath in DI water is used to eliminate any residuals.

2. Hydrofluoric acid (HF) is typically used to remove a thin layer of oxide that grows on top of a material. A mixture of hydrofluoric acid (HF) and DI water was used. The mixing ratio was one part of HF to 50 parts for DI water, and substrates were immersed in this solution at room temperature. A substrate that was initially a hydrophilic surface would become hydrophobic once removed from the solution. A notable difference in the wetting characteristic was observed at about 15 seconds after removing from the solution; the substrate surface would repel any aqueous solutions.

3. The RCA standard clean-1 (RCA SC-1), an alkaline peroxide mixture was followed immediately after treated in HF. DI water, H_2O_2 and ammonium hydroxide (NH_4OH) were required. The ratio for this mixture can vary from 5:1:1 to 50:1:1. If one decides to dilute with more DI water, benefits would include less hazardous to personnel, less microroughing, cost effective, and easier to remove by the following cleaning procedures. This step is used for removal of organic surface films and metals (i.e. Au, Ag, Cu, Ni, Cd, Zn, Co, and Cr). This chemical solution was heated up to about 75 to 80°C (no more than 80°C) and simmered the substrates in the solution for about five minutes. A quick rinse with DI water and follow by additional five minutes in ultrasonic bath with DI water.

4. RCA SC-2, was a mixture that used DI water, H_2O_2, and hydrochloric acid (HCl). Typical mixing ratio ranged from 6:1:1 to 60:1:1. This step was used to dissolve alkali ions and hydroxides such as: $Al(OH)_3$, $Fe(OH)_3$, $Mg(OH)_2$, and $Zn(OH)_2$, as well as trace metals (Cu and Au). Immediately following RCA SC-1, this mixture was heated up to 70 °C, substrates were simmered for five to ten minutes. A quick rinse with DI water and followed by additional

five minutes in ultrasonic bath with DI water.

5. Since the substrates could easily be contaminated "again," use of isopropyl alcohol (IPA) and acetone were desired. The substrate was cleaned using ultrasonic bath with IPA for five minutes and five more minutes with acetone. Using acetone was to prevent dried water marks on the substrate.

6. Following steps for wet cleaning, substrates are further treated with plasma clean. A commercially available plasma cleaner was purchased from Harrick Plasma. The PDC-32G model is compatible with air, Ar, H_2, He, and N_2 gases, but not with F_2 gas since it was corrosive to some materials used in this current setup. According to the specification from plasma cleaner company, etch rate at the surface is about 10 nm/min [67].

3.2.4 Termination bonds on the substrate surfaces

The outermost layer of solid surface usually has dangling bonds due to disruption of crystal lattice. This surface can be very reactive and unstable with respect to chemical species in the surrounding environment [68]. It is critical to treat the substrate during manufacturing process for stable, non-reactive surface termination. For silicon and silicon carbide substrates, a thin layer of oxide film typically grows on the surface. Sapphire is a very inert material, it does not react with oxygen.

Silicon surfaces are typically terminated by -H, -F, or -OH groups. HF solutions are widely used during preparation for termination bonds and to get rid of oxides. For Si(100), formation of SiH_2 is favored because this orientation of dangling bonds after HF solutions. It was observed that hydrogen termination reacts very slow with air and water after etching in HF solutions [68]. However, it has also been noted that since Si-H has a stable bond, it is likely for oxygen to attack Si-Si bond instead [69].

It was also reported, that fluorine bond was found after HF solutions. Whether is was hydrogen or fluorine terminated surface depends on various concentration

of HF solutions [32, 69–71]. Fluorine terminating bond is typically low with HF solutions less than 12% fluoride concentration; but fluorine bonds are increased if the fluorine concentration in HF solutions is increased [72]. Bond energy between silicon-hydrogen bond is about 3 to 4 eV. Where as silicon-fluorine bond has a higher bond energy, around 6 to 7 eV [68]. Although fluorine atoms have larger electronegativity than hydrogen atoms, it was also reported to be less stable than hydrogen terminating bonds [68, 71]. Silicon-fluorine bonds are susceptible to air, therefore can be hydrolyzed to silicon-hydroxyl very easily. These bonding sites are then subjected to oxidation [69, 70].

3.2.5 Deposition of metal contacts

In this section, the processing steps for metal deposition will be discussed. Metallization recipes have been previously addressed in Chapter 2, further details will be described here regarding the dimensions of sensor chips, thickness of the metals to be deposited, and variation of the surface metallization pattern.

Metal deposition onto substrate surface can be done via DC sputtering, RF sputtering, thermal evaporation, electron beam evaporation, ion beam deposition, and chemical vapor deposition, just to name a few. The NSEI Quantum Fingerprint^{TM} Fabrication Unit currently has two sputtering machines. A Denton Desk IV TSC sputtering machine operates by magnetron sputtering. High deposition rate is available at low operating temperature and pressure for this kind of setup. A magnetron-type sputtering machine is usually consisted of cathode (selected target for deposition) with a magnetic backing. The magnet field provides a closed loop field lines at target surface. With the presence of ionized argon gas, positive ions are attracted to the negative voltage potential of target surface. Surface atoms of the target are sputtered if bombarding positive ions have enough kinetic energy to disrupt target's binding energy. Most magnetron-type sputtering machine operates in the pressure range around 1 to 20 mtorr, and negative voltage

potential of 300 to 700 V [73].

The Pelco SC5 sputtering machine operates by DC glow discharge. Configuration for this sputtering system is a target mounted to negative voltage cathode and substrate at anode. The presence of argon ions is kept at pressures around 10 to 100 mtorr, and a DC voltage of 1 to 5 kV is supplied to the electrode. As positive ions bombard target surface, remove atoms from the substrate surface which then condenses on the substrate [73].

In the present work, after cleaning the substrate it was brought into the cleanroom for metal deposition. The metallization pattern for each substrate was done by laying a physical mask over the substrate surface using Kapton® tape. The area in which the substrate surface was masked over corresponds to the area of exposed sensor surface. The optimal dimensions for the sensor surface were determined using the transmission line model (TLM) (see Chapter 2), from which the contact resistance can be deduced. The metallization layers used for silicon were a single Au layer and also an Al layer followed by an Au layer [40]. After metal deposition, substrates were annealed in inert gas (Ar) or H_2 gas for better metal-semiconductor adhesion. The metallization for 4H-SiC (as previously shown in Chapter 2) was done using Ni [47]. For better electrical contacts, Au was also be sputtered as the cap layer onto the substrate. The metallization for sapphire can be a bit more complicated. In order for better bonding between a metal and a sapphire substrate, metals that could form oxides were preferred. Although better adhesion to sapphire substrate has been demonstrated for Zr/Pt [55], but due to the fast oxidizing rate of the Zr metal, Pt layer was tested at this time. The choice of metals deposition the substrate surfaces are currently limited to non-oxidizing metals. Though, the two sputtering machines were operated under inert atmosphere, some of the metals were susceptible to oxygen attacks, which would be problematic as to the continuity of metal contacts.

3.3 Setting up a sensor fabrication and testing environment

3.3.1 Construction of a controlled cleanroom environment

A class 100 softwall cleanroom was built in the laboratory space of Nuclear Science and Engineering Institute, a schematic of the cleanroom floor plan is shown in Figure 3.2. The cleanroom was purchased from HEMCO Corp. [74]. Pre-fabricated structures of the cleanroom were shipped to the university, then assembled. The specifications of the cleanroom are shown in Table 3.3.

The backbone of a cleanroom is the high efficiency particulate air (HEPA) filter, its main functions include filtering out particles up to certain sizes and providing unidirectional airflow inside cleanroom to force out particles initially not removed by the filters. Formation of turbulent flows can be related to accumulations of particulates that remain in or are generated in the cleanroom. In order to minimize turbulent flows, the layout, spacing, and air flow velocity of HEPA filters were important considerations [75]. There are a total of eight HEPA filters installed, seven in the cleanroom and one in the gowning area, all of which are located on the ceiling. The cleanroom maintains a positive pressure in the room and the direction of air circulation pushes air out from underneath the softwall vinyl curtain, and circulates back into the room from the top. Cleanliness in the entire laboratory space can influence the workload of the filters and in result affect the lifespan of the filters. Since turbulent airflow are undesirable, the workbench areas are situated directly underneath each of the HEPA filters to maximize the usage of unidirectional airflow.

Static control is also critical to the functionality of cleanroom. Particulates can be held statically to surface, which can be difficult to remove with wipe down or wet cleaning. Essentially, anti-static materials are utilized in the cleanrom to the extent which is possible, to prevent any static charge buildup [65]. At the NSEI

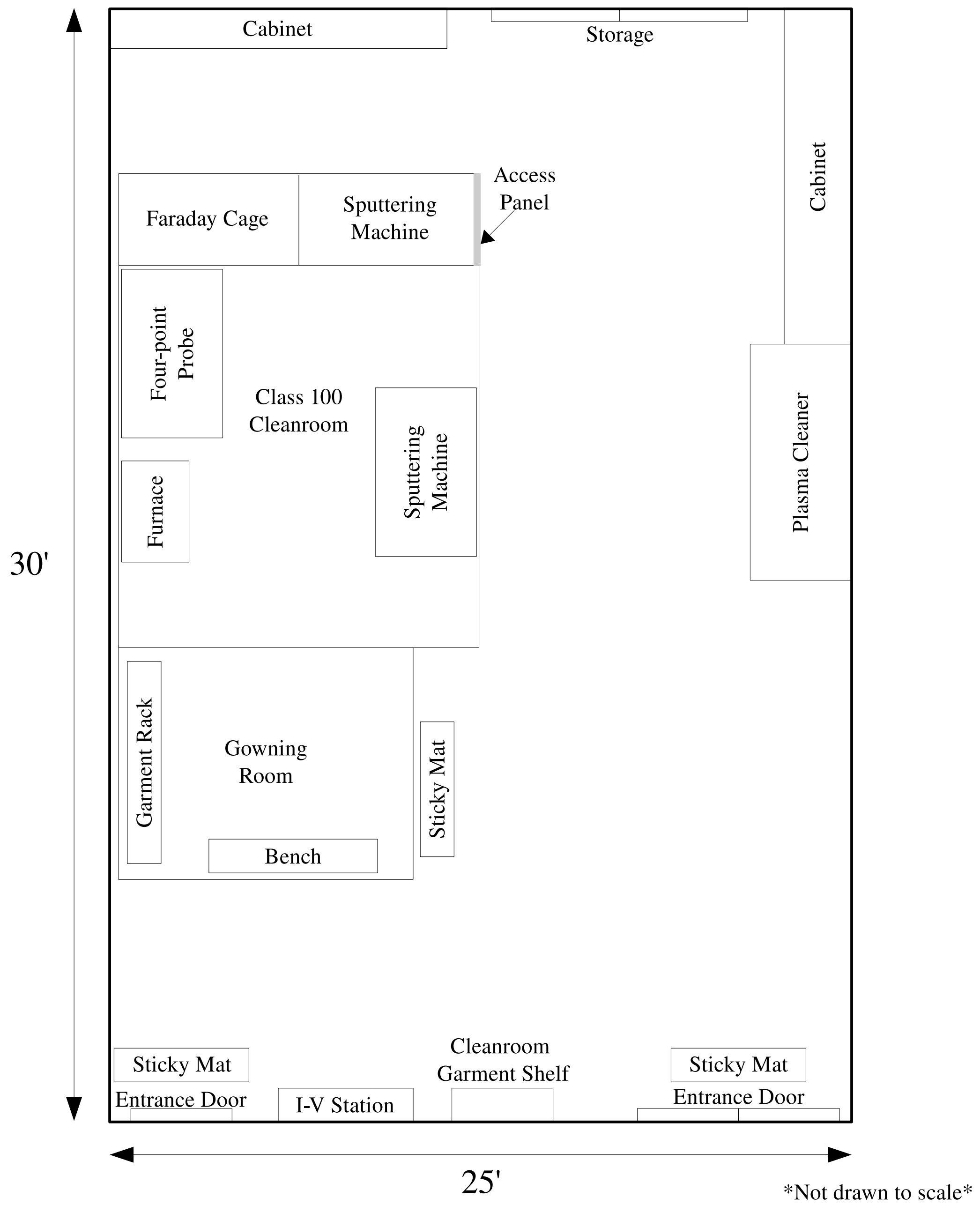

Figure 3.2: Cleanroom arrangement.

Quantum Fingerprint^{TM} Fabrication Unit, layers of static control paint were coated on the floor covering cleanroom, furniture, and anti-static personnel garments were also purchased.

Table 3.3: Specifications of the cleanroom at NSEI.

Specifications	Description
Class	100
Exterior dimension	12' L x 10' W x 9' H
Interior dimension	12' L x 10' W x 8' H
Gowning room	6' L x 6' W x 9' H
Gowning room interior dimension	6' L x 6' W x 8' H
Structural frame	6063-T5 aluminum
Ceiling	Polyprolylene ceiling panel
HEPA modules	99.9% efficiency for 0.3 μm particles
Number of HEPA modules	7 HEPA modules in the cleanroom and 1 module HEPA in the gowning area
Vinyl curtain/Strip doors	60 mil thickness and 6" off the ground

3.3.2 Enclosures for sensor testing

Aside from the importance of cleanroom for the Quantum Fingerprint^{TM} sensor chip fabrication, testing of the sensor chip should be conducted under a controlled environment in order to limit the interference of other airborne substances. The approach used in this work was to place the sensor chip in an enclosed system of a known volume, followed by introduction of the targeted species. Two types of enclosures were initially used in this research: a glass chamber and an aluminum enclosure (shown in Figure 3.3). The glass chamber (Pyrex) was designed at NSEI and custom manufactured by Wilmad-Labglass. Feedthroughs were de-

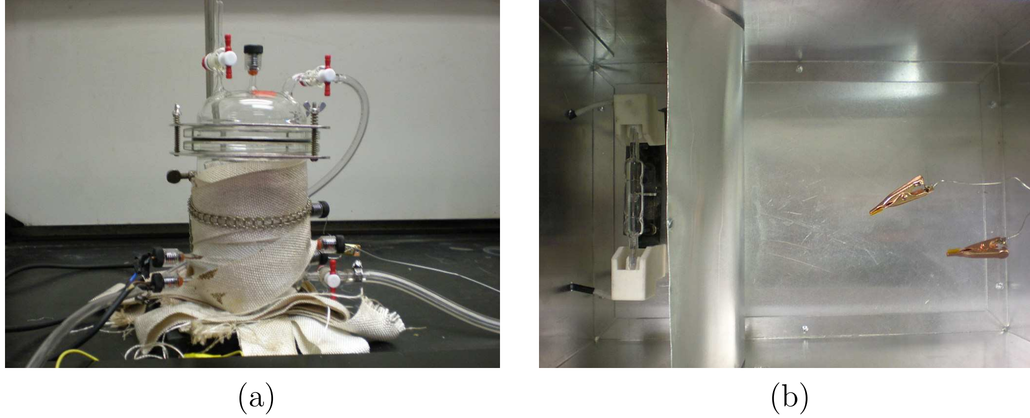

(a) (b)

Figure 3.3: Enclosures for sensor testing. (a) Glass enclosure and (b) Aligator clips and tungsten heating source inside shielded aluminum enclosure.

signed to maximize ports for sensor chips and targeted species introduction, and viton O-rings allowed for a vacuum seal. The features of the glass chamber are: the capability of chamber to hold vacuum (down to roughly 10^{-2} torr) thus limiting the contaminants and allow for monitoring gas concentration in a given (known) volume; an enclosed system which sample can be introduced and isolated from the external environment; the sensor chips were made from semiconducting materials, and since the conduction of electrons are thermally dependent, controls to constant temperature is crucial. The difficulties associated with this setup is that the glass chamber was not electrically shielded (although attempts were later made), data collection is therefore sensitive to surrounding noise (predominately 60 Hz interference). Another approach was an aluminum enclosure, the chassis itself was connected to a common ground along with Q-DLTS device. Although this setup allowed easier access to measure between different sensor chips, but data could only be collected at atmospheric pressure. Presence of air molecues was contributing to the signals.

3.3.3 Construction of a vacuum system for sample introduction

To solve the problems encountered while using the original (preliminary) test chambers, a stainless steel testing system was designed and built.

The stainless steel bell jar was purchased from Huntington Mechanical Laboratories. The bell jar has a 18" inner diameter base well and 30" in height. There is a view port and a total of eight ports for additional equipments. A schematic drawing of the vacuum system design and labels are shown in Figure 3.4. And the pictures of this vacuum system are shown in 3.5a and b.

The purpose of using a bell jar is to provide a controlled environment for the testing. A typical stainless steel bell jar is rated to be able to hold vacuum down to about 10^{-9} torr. The bell jar was wrapped around with heating tape and insulating material to manage the surrounding temperature. Auxiliary components to this vacuum system were the gas mixing enclosures, a gas flow control, pressure gauges, and a residual gas analyzer. Introduction of targeting species for testing could be controlled and monitored with these components. These include, the concentration amount, mixing ratio of the mixtures, and monitoring the presence of other species in the vacuum system. Targeting species could be introduced in the form of gas, liquid, or solid phase into the vacuum system. The QF^{TM} sensor chips sitting inside the bell jar would be connected through the electrical feedthroughs to the Q-DLTS device outside of the vacuum system. The bell jar therefore served as a controlled environment and Faraday shield against noise interference.

3.4 Data processing

A protype charge-based deep-level transient spectroscopy (Q-DLTS) unit was constructed by Daniel Montenegro, a graduate student at the NSEI. Based upon modifications of the design by D.V. Lang [1].

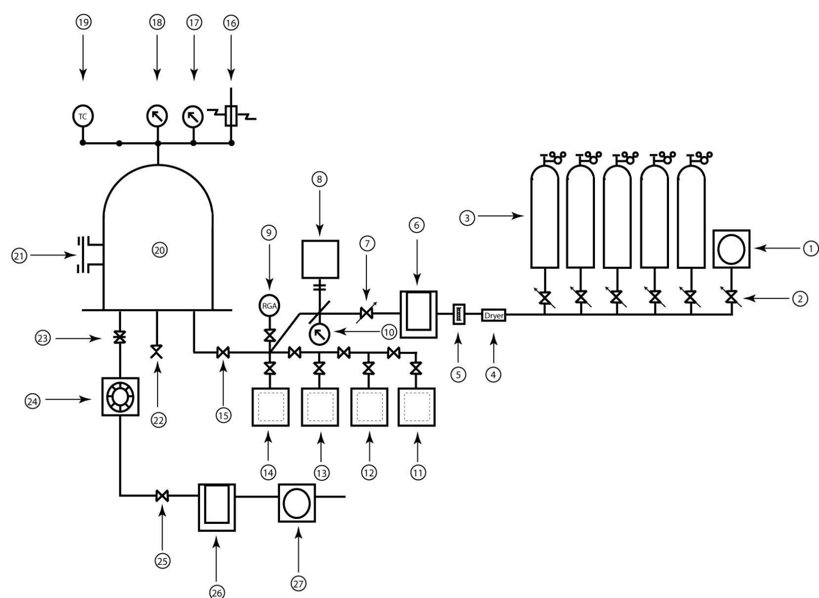

No.	Item	No.	Item	No.	Item	No.	Item
1	Roughing pump	**8**	Sample holder with Kwik flange disconnect	**15**	Butterfly valve	**22**	Vent-to-air valve
2	Needle valve	**9**	Residual gas analyzer	**16**	Electrical connections of sensor chips	**23**	Gate valve
3	Gas tanks	**10**	Pressure gauge (1000 Torr to 10^{-3} Torr)	**17**	Pressure gauge (1000 Torr to 10^{-3} Torr)	**24**	Turbomolecular pump
4	Dryer	**11**	Enclosure (Vol. 1)	**18**	Pressure gauge (10^{-3} Torr to 10^{-10} Torr)	**25**	Valve
5	Oxygen absorbent	**12**	Enclosure (Vol. 2)	**19**	Thermocouple	**26**	Oil trap
6	Oil trap	**13**	Enclosure (Vol. 3)	**20**	Bell jar	**27**	Roughing pump
7	Valve	**14**	Enclosure (Vol. 4)	**21**	View port		

Figure 3.4: Vacuum system design.

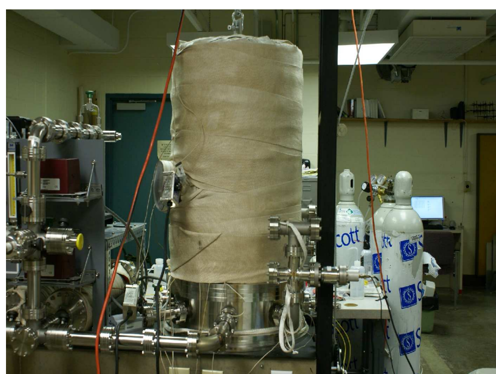

(a)

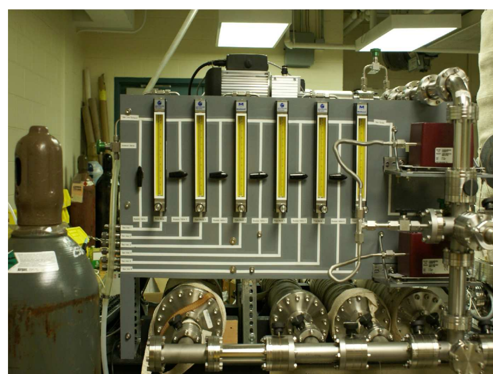

(b)

Figure 3.5: Vacuum system and gas mixing apparatus. (a) Stainless steel bell jar and (b) Gas mixing apparatus and flow control.

3.4.1 Data collection and signal analysis for MU prototype QDLTS unit

MU prototype Q-DLTS device was designed and constructed. The double-boxcar approach with analog controls of capacitance collection, is replaced with digital output and computer software manipulation. Data acquisition was performed using a NI USB-6009 DAQ card from National Instruments, allowing analog signals to be converted into digital signals. LabView software environment was available for user interface to the DAQ cards; digital output was saved as ASCII file and imported into Mathematica®for data analysis.

Preliminary testings with MU prototype QDLTS unit have been tested on diodes, LEDs, and RC network circuits. Uses for DLTS and related deep-level transient measurements have been tested on metal-insulator-semiconductor (MIS) capacitors, *pn* junction diodes, and so forth. Measurements on known samples were critical for verification of prototype Q-DLTS unit's functionality.

After a filling pulse was applied to the sample, energy states were excited to the conduction band, followed by relaxation back to minimum energy states. Raw data from the QDLTS unit contained information on voltage versus time. A computer code was written in Mathematica® program, would import these data and analyze them. Earlier published work [1, 58, 59] have utilized the rate window concept to describe the emission rates from trap centers. The rate window approach for Q-DLTS signals looked at voltage difference (or charge difference) at selected times across the specified time domain. A maximum response would result in distinctive peaks that corresponds to the trap centers; Q-DLTS signals can be expressed as: $\Delta S = V(t_2) - V(t_1)$, where S is the signal obtained from voltage (V) difference between t_1 and t_2 time interval. Emission rates of trap center can be expressed as: $\tau_{e,max} = \frac{t_2-t_1}{ln(t_2/t_1)}$.

In the early DLTS designs, the double boxcar technique was controlled by analog switches which manipulate timing of the current flow through the integrator.

The rate window (t_1 and t_2) was controlled by the analog switches, allowing signals to be collected at these times. For convenience, t_2/t_1 ratio was kept constant as signals were collected over the specified spatial range. The MU prototype QDLTS unit converted the analog output into digital output. The DAQ card could sample at every 22 μ seconds, and collects voltage output. Rather than relying on analog switches to control the rate window, t_2/t_1 ratio was kept constant, and their values were generated from algorithms written in computer code. The capability of modern analog-digital converter (ADC) allowed signals to be processed digitally, but also, less prone to malfunction from hardware failure. Although the actual time recorded may not match to the generated t_1 and t_2 from calculated values. The computer code was constructed in which information could be interpolated between the known points. The raw data of voltage output (integrated over time) were compared against the interpolated points. The interpolation function built-in from Mathematica® was able to match with the original raw data. This step signifies that the values calculated for t_1, t_2, and corresponding voltage output was a good representation of the actual data. The subsequent processing for Q-DLTS signals would be comparable to signals output from analog switches. A flow chart of this computer program implemented is shown in Figure 3.6.

3.4.2 Investigation of other signal analysis approach

Additional methods have been considered and investigated to provide insights to deep-level energy traps. So far, capacitance, current, and charge transient spectra using the double-boxcar technique was the commonly preferred method. Mathematica® programming environment was used to benchmark some of the other approach for signal analysis. Discrete Fourier transform and data fitting of decay constant were also examined.

Fourier transform is generally used to examine information between spatial domain and frequency domain. Examples which Fourier transform algorithm was

used are, Fourier transform infrared spectroscopy (FTIR), magnetic resonance imaging (MRI), and nuclear magnetic resonance (NMR). The common principle of operation was that, Fourier transform algorithm could explain a change in frequency due to a stimulant, and followed by relaxation. For instance, in FTIR spectroscopy, the vibrational motion of molecules were triggered by a photon stimulant. Molecules of various compositions would come back to original state at different relaxation times. Similarly, Fourier transform for MRI and NMR allowed for frequencies and amplitudes of periodic and sinusoidal wave signals to be deciphered. When dealing with the discrete time functions from the Q-DLTS signals, discrete Fourier transform analysis was attempted. The reason being, after a filling pulse was applied to a sample, the relaxation of electrically charged deep-level traps were observed. It was postulated, that discrete Fourier transform analysis may be used to describe the freqencies and amplitudes associated with these relaxation states. However, since the raw data collected were not periodic in nature, therefore Fourier transform analysis could not be utilized to describe relaxation from the deep-level traps.

Exponential analysis for the relaxation of electrically charged deep-level traps was also explored. The emission rates from electrically charged deep-level traps could be evaluated by the exponential decay function. The mathematical expressions for emission rates from deep-level traps have been discussed in chapter 2 of this work. The data collected contained information of exponentially decay from these deep-level traps, which corresponds to the decay constant or the emission rate. The exponential decay signal can be expressed and simulated by a generic expression, $S(t) = S_0(e^{-\lambda t})$. Furthermore, for multiple components in the exponential decay, the expression now becomes $S(t) = S_0 \sum_{i=1} n(e^{-lambda_i t})$. Data can be fitted by using these generic expression to find the decay constants. Preliminary testings were done using this method, however, it was soon realized this is a computational expensive approach. As multiple components of decay constants

increase, processing time and accuracy of data fitting may be problematic.

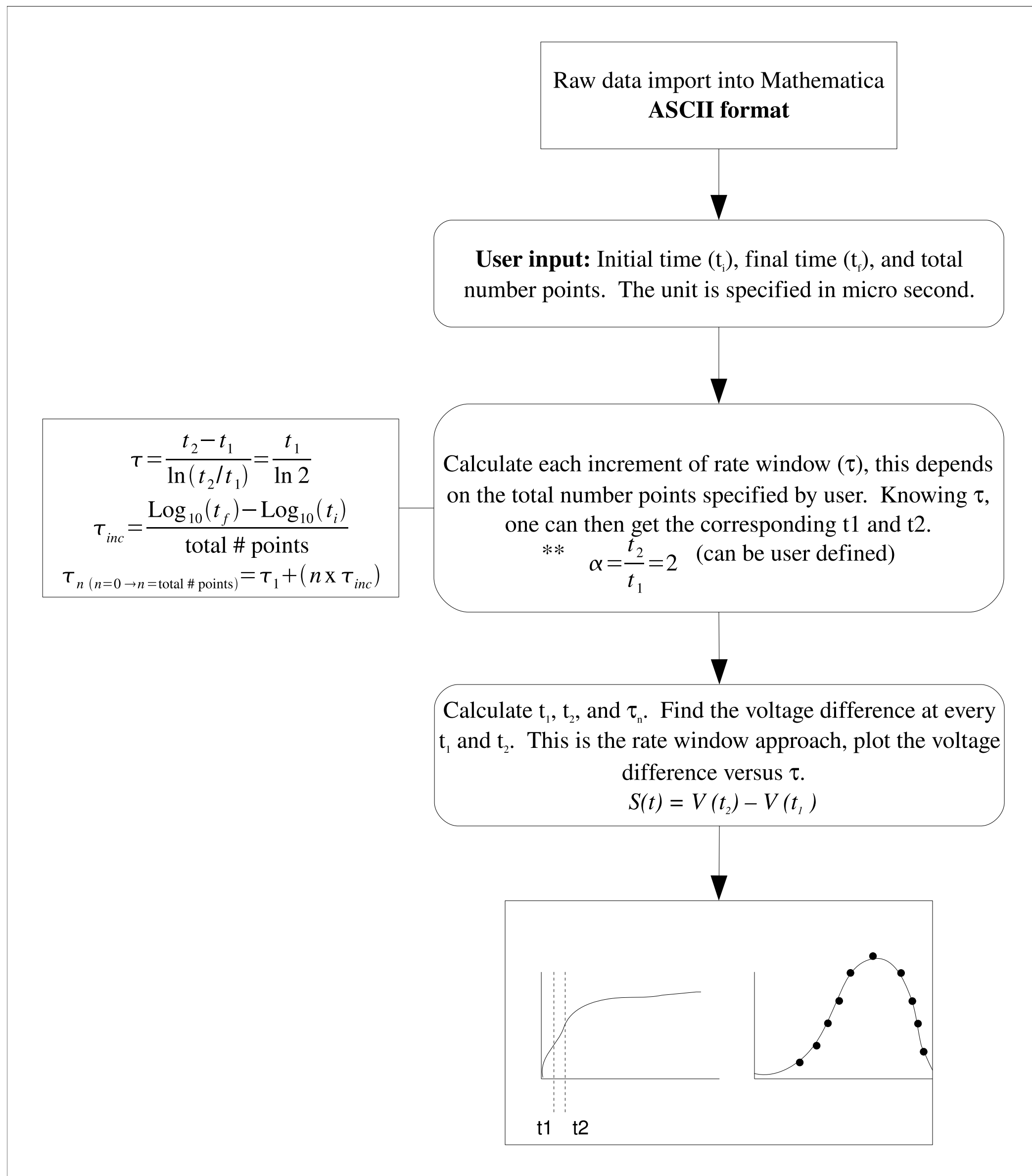

Figure 3.6: Flow chart of computer program.

Chapter 4

Results and Discussion

4.1 Results of preliminary tests on commercially packaged QF^{TM} sensor chips

4.1.1 Characterization and preparation of prototype QF^{TM} sensor chips

An initial batch of prototype QF^{TM} sensor chips were fabricated from Si, n-type 6H-SiC, and sapphire. The selected materials were 2” diameter, single crystal wafers. Metallization on all three materials was the same, Ti/Pt/Au with a total thickness of 1 μm. To allow for maximum detection area on the sensor surfaces, a comb-tooth, interdigitated pattern was metallized onto each wafer, an example of the product is shown in Figure 4.1.

The initial fabrication of the interdigitated pattern, metallization of proto-

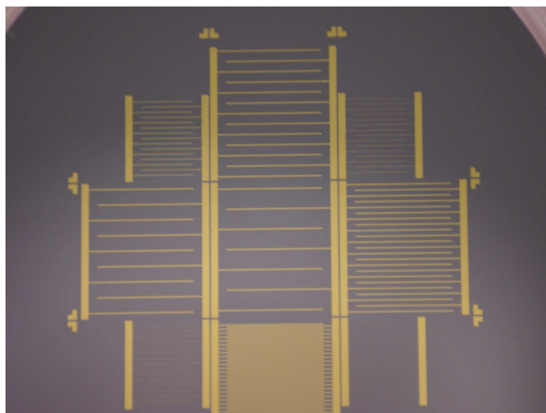

Figure 4.1: 2” diameter Si wafer with interdigitated pattern.

type sensor chips was contracted to Osemi, Inc., a company based in Red Wing, Minnesota which specializes in producing semiconductor epitaxial materials and provides consulting services for lithography. The metallization was done by Osemi using electron beam lithography. In this method, the scanning electron beam removes photoresist and lays the interdigitated pattern. The deposition of the metal layers were then done by evaporation. After metallization, wafers were sent to University of Missouri for annealing in an inert atmosphere up to 450°C. The thermal treatment process was done to enhance formation of alloys between each metal layers and to help sure better adhesion to semiconductor surface. In Table 4.1, the thermal treatment parameters used for the annealing of the semiconductor substrates in this work are shown.

Table 4.1: Thermal treatment parameters used for the lithographically fabricated sensor chips.

Material	Annealing gas	Annealing rate	Cooling rate	Maximum temperature	Hold time at maximum temperature
Silicon	Argon	25°C/min	25°C/min	450°C	30 min
Sapphire 1	Argon	2°C/min	2°C/min	450°C	30 min
Sapphire 2	Argon	1°C/min	1°C/min	450°C	30 min
6H-SiC	Argon	1°C/min	1°C/min	450°C	30 min

After performing the annealing process, it was noted that some of the metallization had peeled and that only a fraction were used for packaging. Some of the wafers that were successfully annealed were sent to NxGen Electronics (a company based in San Diego, California) for packaging. The wafers were diced according to the interdigitated array. In the chips which could be recovered for packaging, the top most metallization layer, gold, had diffused to lower metallization layers. Ball bonding with gold wire was therefore difficult, wedge bonding with aluminum wire

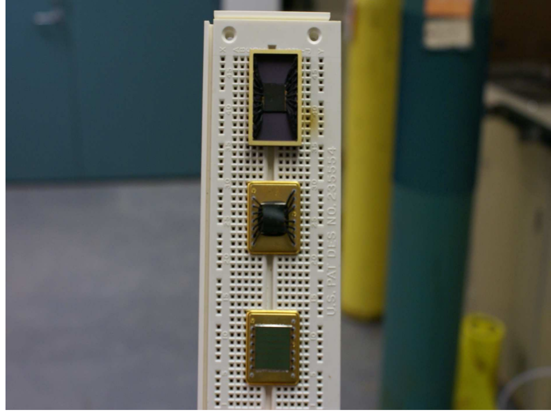

Figure 4.2: Prototype packaging of QF^{TM}.

was used instead. The sensor chips were packaged using two types of designs, a metal-based and a ceramic-based. The metal-based packaging were coated entirely with gold and conductive epoxy were used to attach the chips. The whole packaging was conductive and thus could contribute to additional capacitance during Q-DLTS measurements. A ceramic-based packaging and a non-conductive epoxy were used. This design was superior to the metal-based packaging because, the electrical current could only traverse through the wires (from wire or wedge bonding) and not anywere else. In Figure 4.2 these two prototype packagings are shown.

4.1.2 Preliminary measurements

Preliminary measurements were performed to evaluate the QF^{TM} sensor chips. An ammeter model number Agilent E5272A manufactured by Agilent Technologies was used to examine the ohmic characteristics of the packaged chips; results of the current-voltage (I-V) measurements are shown in Table 4.2.

Table 4.2: Prototype QF^{TM} sensor chips.

Name	Material	Packaging material	Epoxy used	Ohmic contact
SN02C	6H-SiC	Metal	Silver conductive epoxy	Yes
SN01S	Sapphire	Metal	Silver conductive epoxy	No
SN02S	Sapphire	Metal	Silver conductive epoxy	No
SN03S	Sapphire	Metal	Silver conductive epoxy	No
01	Sapphire	Metal	Non-conductive epoxy (Hysol FP4401)	No

Continued on Next Page...

Table 4.2 – Continued

Name	Material	Packaging material	Epoxy used	Ohmic contact
02	Sapphire	Metal	Non-conductive epoxy (Hysol FP4401)	No
03	6H-SiC	Metal	Non-conductive epoxy (Hysol FP4401)	Yes
04	Sapphire	Metal	Non-conductive epoxy (Hysol FP4401)	No
S/N001	6H-SiC	Ceramic	Non-conductive epoxy (Hysol FP4401)	Yes
S/N002	Sapphire	Ceramic	Non-conductive epoxy (Hysol FP4401)	No
S/N003	Sapphire	Ceramic	Non-conductive epoxy (Hysol FP4401)	No

Only the sensor chips fabricated from 6H-SiC were shown to have ohmic characteristics. Delamination occurred during annealing process for Si wafer which is likely due to thermal stresses between Ti and Pt layers. The packaged sapphire sensor chips did not show linearity in I-V responses. The I-V curves for 6H-SiC are shown in Figure 4.3.

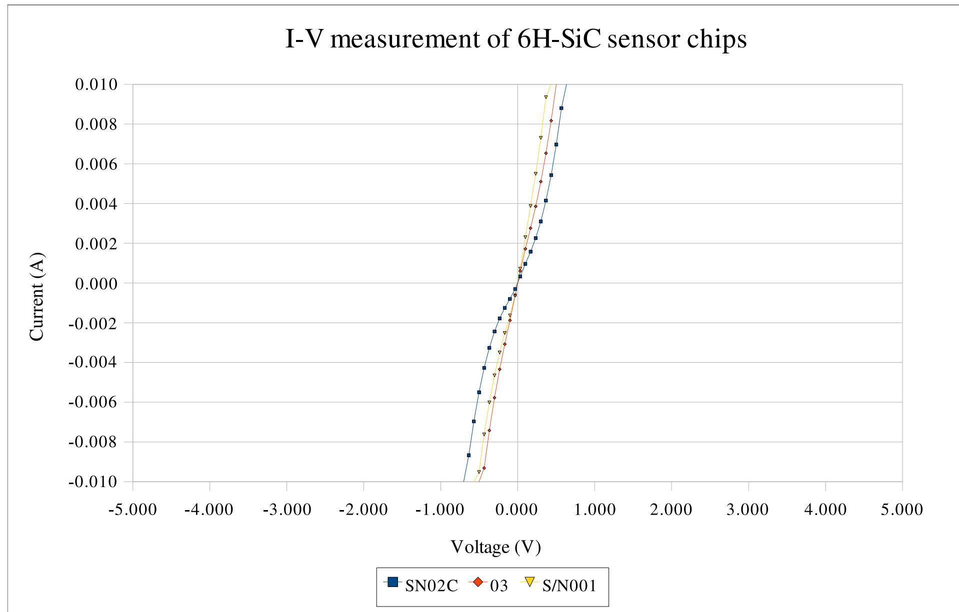

Figure 4.3: Current-voltage curves for the 6H-SiC sensor chips. Produced by Osemi Inc., and packaged by NxGen Electronics.

The preliminary Q-DLTS measurements were obtained using an ASMEC (Automatic System of Material Electro-Physical Characterization) system, manufactured by InOmTech®. Both the shielded metal enclosure (a part of ASMEC system) and a glass chamber were used for these measurements. The metal enclosure could only be measured at atmospheric pressure and was exposed to the external room air. The glass chamber was designed with several feedthroughs for target species introduction. However, noise interference and capacitance effect could not be avoided under this setup.

Q-DLTS signals were collected for the 6H-SiC packaged prototype sensors chips and a humidity sensor which was used. The humidity sensor (Vaisala HUMICAP®) is a commercially available product from Vaisala [76]. The humidity sensor has a thin-film polymer that changes dielectric properties with ambient humidity. Which in turn, allows one to measure the humidity based on changes in capacitance. In the preliminary tests, 1 mL of isopropanol alcohol was introduced into the metal enclosure. Figure 4.4 shows the graph for humidity sensor. Data was collected in atmospheric air with and without alcohol. It was noted that the observed Q-DLTS

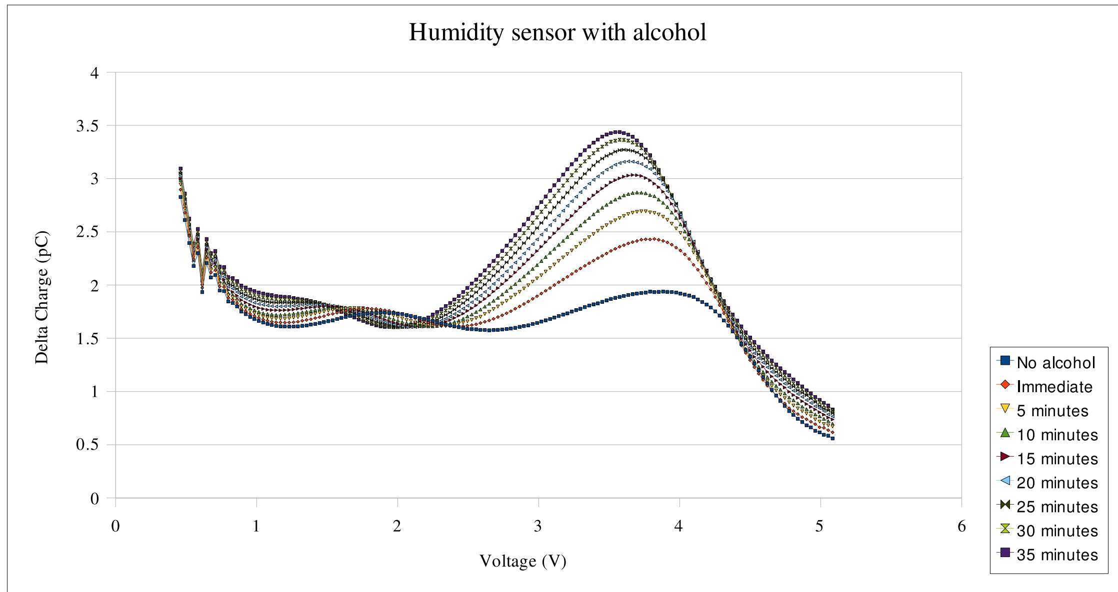

Figure 4.4: Q-DLTS spectra measured using the ASMEC system with a Vaisala HUMICAP humidity sensor with introduction of 1 mL isopropanol in a background of atmospheric air.

Spectral peaks became more prominent in the presence of alcohol over a period of time.

The same Q-DLTS measurements for prototype 6H-SiC sensor chips were also taken. The sensor chips were placed inside metal enclosure and exposed to air, isopropanol, and water vapor. The data collected using 6H-SiC sensor chip (SN02C) and the ASMEC systen are presented in Figure 4.5. Smoother spectral peaks were anticipated rather than the sharp peaks shown, since the ASMEC system utilizes a rate window approach. Where the emission traps would correspond to peaks on the spectrum. It is possible that the sharp peaks shown in Figure 4.5 are not the spectra. Rather, they were contributions from the poor metallization, the packaging, and noise (electrical interference, etc.). Another explanation could be due to to 6H-SiC's tight lattice spacing. If a crystal lattice has sufficient tight spacing, it is believed that it could be better at discerning the adsorbed species. More measurements are required to confirm these observations.

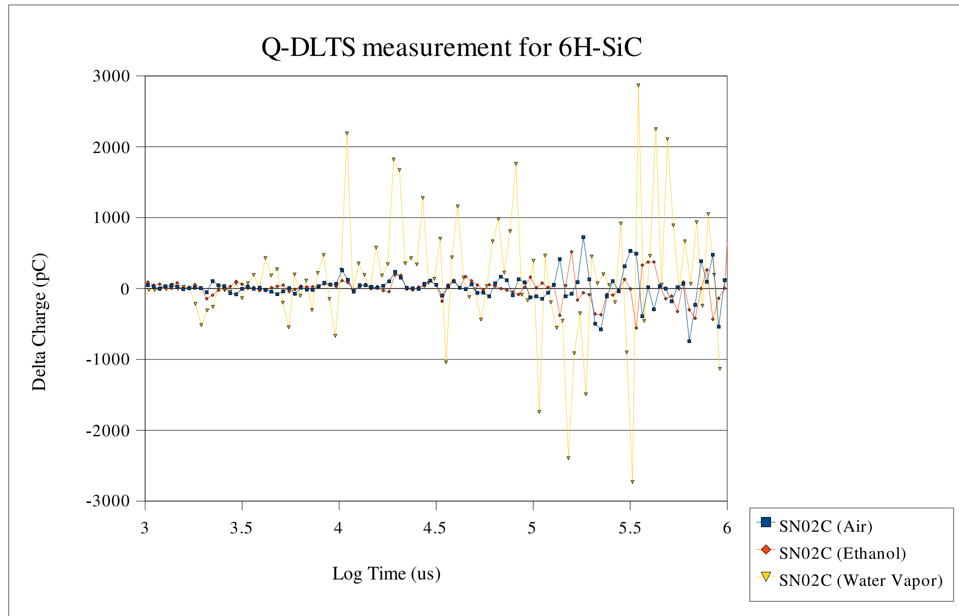

Figure 4.5: Q-DLTS of 6H-SiC sensor chip (SN02C) measured using the ASMEC system with presence of isopropanol and water vapor in a background of atmospheric air.

4.1.3 Discussion of the results from preliminary QF^{TM} sensor chips

Problems were encountered that contributed to unsuccessful fabrication of silicon and sapphire wafers. It was determined that a number of errors were made during the manufacturing process which include: (1) a thorough cleaning process was not performed before electron beam lithography and metal deposition for all of the wafers used an thus, air pockets and contaminants could be seen, creating discontinuities for metallization; (2) the gold layer diffused through the diffusion layer during annealing, which greatly reduced the area available for wire bonding; (3) during lithography, the scanning electron beam did not remove the resist evenly, leading to missing interdigitated lines that would otherwise effect the performance of that particular sensor chip; and (4) delamination between the metal layer and semiconductor surface, which is possibly due to presence of foreign contaminants and thermal stress created by rapid heating and cooling. It was believed that the silicon wafer had suffered from delamination of the metals between that of Ti and

Pt layer, most likely due to rapid cooling rate, causing thermal stress to the layers. In Figures 4.6a through 4.6c, photos taken of the sensor chips during fabrication are shown. Since sapphire is a very good insulator, a good metal contact would be required for electrical conductivity. Contaminants on the surface would be devastating because the electrical current would preferentially find an alternate pathway (through the contaminants), which would contribute to statistical noise. Furthermore, the gold layer had diffused through the Pt and Ti layers, which will decrease the available contact area for packaging (wire bonding) and act to increase the contact resistance. The current and voltage responses for the sapphire samples were shown to be those for an insulator and therefore, the samples were not suitable for Q-DLTS measurements.

The preliminary measurements of the packaged QF^{TM} sensor chips have shown that the fabrication process must be carefully controlled. A stringent quality control during the fabricating process and proper testing system is required for testing the performance of QF^{TM} sensor chips. Further metallization recipes and processing methods should be explored for 4H-SiC and sapphire. A proposed experimental matrix for metallization testing for both of these substrates is included in Tables 4.3 and 4.4.

Table 4.3: A proposed metallization experimental matrix for 4H-SiC based sensor chips.

Metal	Thickness (nm)	Annealing rate (°C min^{-1})	Cooling rate (°C min^{-1})	Maximum temperature (°C)	Hold time at maximum temperature
Ni	200	20	20	900	5 min
Ni/Au	200/200	20	20	900	5 min

(a)

(b)

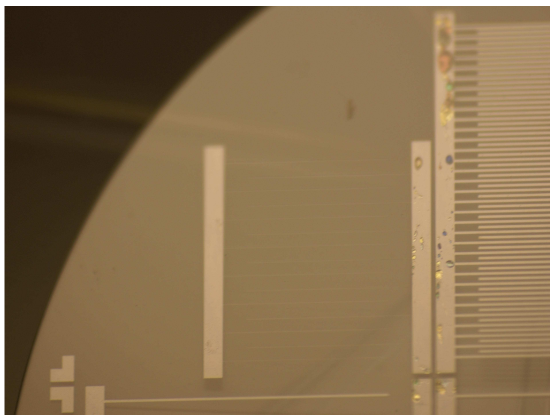

(c)

Figure 4.6: Damaged wafers: (a) delamination on Si wafer between Ti and Pt layers (b) front side of sapphire wafer after annealing, air bubbles can be seen (c) back side of sapphire after annealing, air bubbles and diffused gold.

Table 4.4: A proposed metallization experimental matrix for sapphire based sensor chips.

Metal	Thickness (nm)	Annealing rate (°C min^{-1})	Cooling rate (°C min^{-1})	Maximum temperature (°C)	Hold time at maximum temperature
Pt/Au	200/200	20	20	900	5 min
Ag/Au	200/200	20	20	900	5 min

4.2 Preliminary prototype Q-DLTS unit and computer code evaluation

A preliminary computer code was written in Mathematica®for the Q-DLTS data analysis. The data collected from the MU Q-DLTS prototype unit was analyzed with this computer code to view the transient spectra.

The rate window algorithm was first to be explored in this work. This technique has been used since the DLTS technique was developed by Lang [1]. Many other of transient spectroscopy methods have also utilized this approach, namely current and charge transients [2,57–59]. A common approach from the above transient spectroscopies is the use of double boxcar for rate window algorithm. In the previous works, mechanical switches were incorporated in the circuits to control sampling time and the magnitude of the output signal. The MU Q-DLTS prototype unit data collection has been synchronized between the LabView®software program and a DAQ card from National Instruments. The raw data recorded consists of the sampling time and associated voltage output as determined from on board integration of the charge collected. The computer code written in Mathematica®is structured to import and average the data, and then feed the data into a separate module to perform rate window algorithm calculations.

Since, the Q-DLTS and related techniques were initially designed to look at space charge region of semiconductors; diodes which had known Q-DLTS spectra

were selected for evaluation. In Table 4.5 some of the specifications are shown for these diodes. Another sample was also tested using the MU Q-DLTS prototype unit. Two two pairs of RC (resistor-capacitor) networks were connected in parallel. This sample design was design was selected for mimicking the emission rates from deep-level trap centers, since each RC network has an associated time constant which would correspond to a peak location in rate window algorithm. The results were compared for both InOmTech®ASMEC and the MU prototype. As mentioned earlier, the ASMEC utilized mechanical switches to control sampling timing, followed by use of the double boxcar approach. From the collected data, the prototype computer code was used to calculate the values required to generate a Q-DLTS spectrum. With the same parameters set for data collection, Table 4.6 details these parameters and Figure 4.8 shows comparison of these two spectra. From Figure 4.8, it shows that Q-DLTS spectra for both systems match one another at the peak locations (x-axis, in units of log μ seconds, at x = 2.5 and 4.3). Width of the areas underneath the signals were a little different and the charge collected for the second peak was less for the ASMEC. These differences were due to the mechanism in which a bias pulse was applied. The ASMEC varied by first V_0 followed by $V_0 + dV$, the signal is therefore the differential of these two bias voltages. The MU prototype had a constant bias voltage applied, the signal is given any differential voltages. However, the result from RC measurement had indicated that the prototype unit is working as it should, and the computer code written for rate window algorithm does simulate that of hardware switches.

Table 4.5: Specifications of commercial diodes used for Q-DLTS evaluation.

Sample	Material	Diode capacitance (pF)	Reverse voltage (V)	Leakage current
FJH 1100 diode	Si	2	–	3 pA at 5 V and 10 pA at 10 V

Continued on Next Page...

Table 4.5 – Continued

Sample	Material	Diode capacitance (pF)	Reverse voltage (V)	Leakage current
Red LED	AlGaAs or GaAsP or GaP	–	5	–

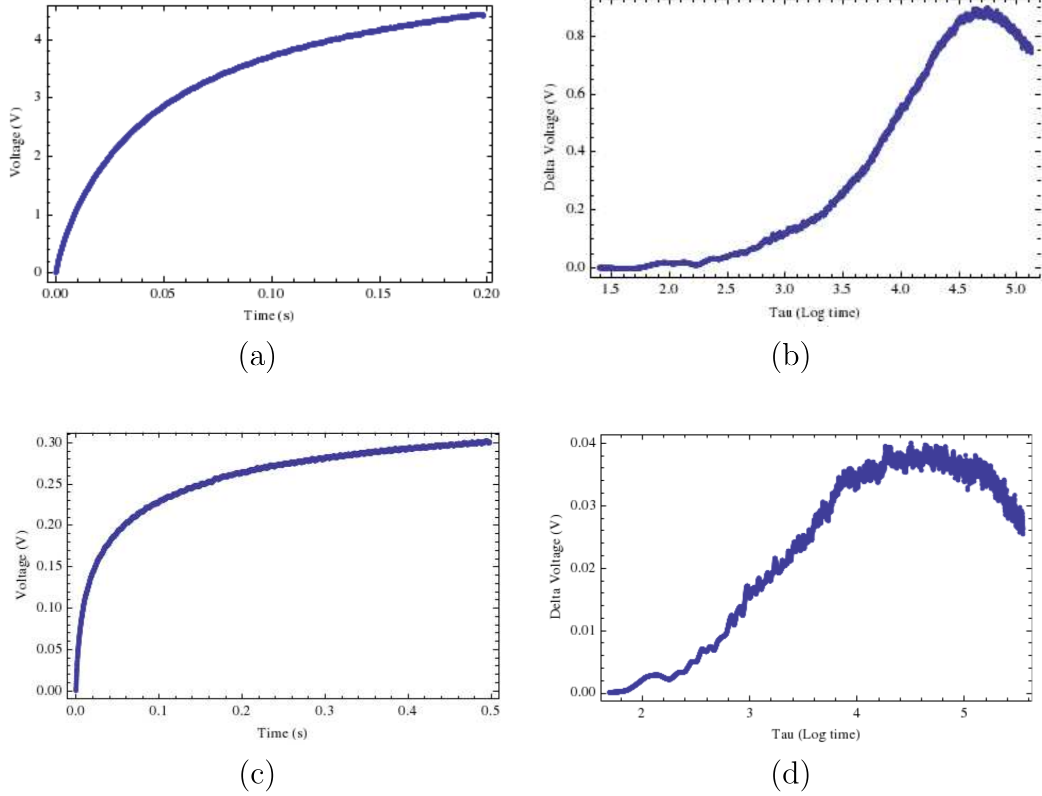

Figure 4.7: Preliminary examination of diodes with Q-DLTS (a) integrated voltage data for FJH1100 diode, (b) QDLTS of FJH1100 diode, (c) integrated voltage data for red LED, and (d) QDLTS of red LED.

Table 4.6: Specifications of commercial diodes used for Q-DLTS evaluation.

Sampling parameters	Values
τ_i (μs)	10
τ_f (μs)	10^6
Pulse width (μs)	500
Offset voltage, V_0 (V)	5
Bias voltage, dV (V)	1
Gain	100

4.3 In-house silicon sensor chips

Prototype sensor chips were fabricated in-house using both low and high resistivity silicon wafers. In order to simplify the production process and the uncertainty from metallizing a comb-tooth pattern, a single-strip exposed silicon surface pattern was used. Each chip was scribed to a dimension of 2.6 x 1.2 cm^2, which would mount onto a standard ceramic-based semiconductor package (purchased from Spectrum semiconductor materials, Inc. and product number HYB02415).

4.3.1 Material characterization and preparation

Each sensor chip was fabricated following the procedures described in chapter 3 of this work. The substrates were prepared to minimize any contaminants on the surface before performing material and electrical characterization. The characterization methods used for the in-house silicon samples produced in this work include raman spectroscopy, infrared spectroscopy, scanning electron microscopy, electron dispersive spectroscopy, and current-voltage response.

Both silicon substrates of high and low resistivity were processed with a two-solvent cleaning method. This is also called the AMD method (Acetone, Methanol, and D.I. water), while the solvents are used to remove oil and organic residues. The silicon samples were simmered in acetone and placed inside ultrasonic bath for five minutes. This was followed by simmering the sample in methanol inside the ultrasonic bath for another five minutes. Lastly, the samples were rinsed with and simmered in D.I. water in the ultrasonic bath for another five minutes to get rid of the solvents. After the cleaning process, the silicon samples were then characterized before metallization. Raman spectroscopy, infrared spectroscopy, scanning electron microscopy, and electron dispersive spectroscopy were used at this point to characterize the samples. For raman and infrared spectroscopies, the spectral libraries were available for comparison. The results obtained in this work confirmed that it was indeed silicon. In Figures 4.9a through 4.9f, an example of the results of raman spectroscopy, infrared spectroscopy, and scanning electron microscopy for the samples are shown. Electron dispersive spectroscopy was also used to verify the sample substrate's composition and representative results are included in Figures 4.10 through 4.12.

The electrical properties of the silicon substrates were also measured prior to metallization. The resistivity measurements were done using an Agilient E5272A ammeter connected to a probe station. The two probe needles were pressed onto the surface and the resistivity between the probes was measured. Some examples of the

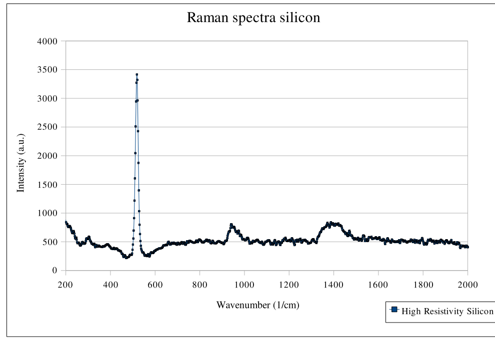

(a)

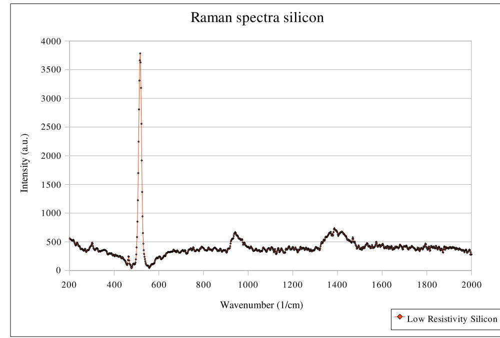

(b)

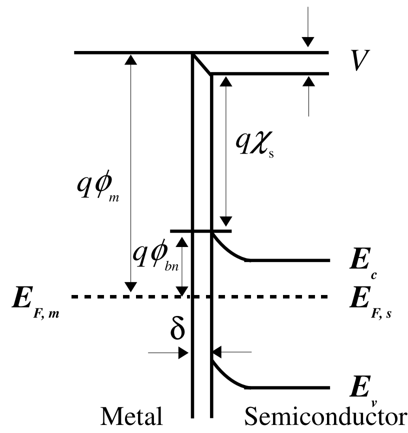

(c)

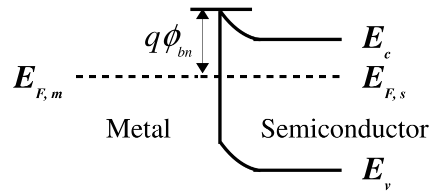

(d)

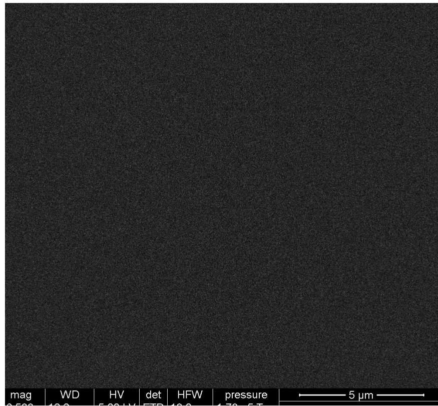

(e)

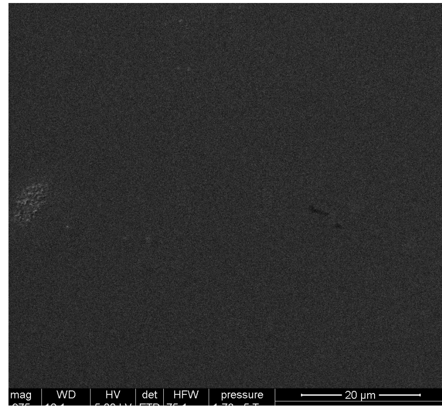

(f)

Figure 4.9: Some representative material characterization measurements for silicon substrates used in this work: (a) Raman spectroscopy of high resistivity silicon, (b) Raman spectroscopy of low resistivity silicon, (c) IR spectroscopy of high resistivity silicon, (d) IR spectroscopy of low resistivity silicon, (e) SEM of high resistivity silicon, and (f) SEM of low resistivity silicon.

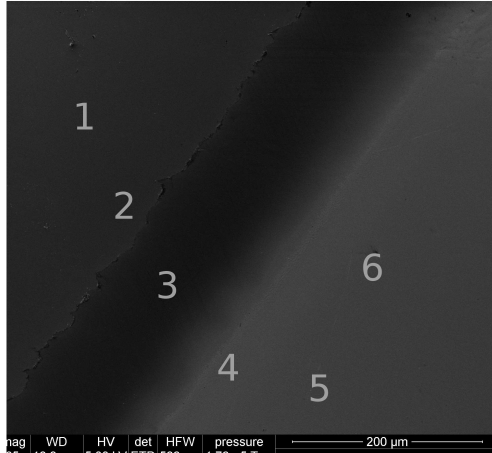

Figure 4.10: A SEM image indicating test locations on a representative sample.

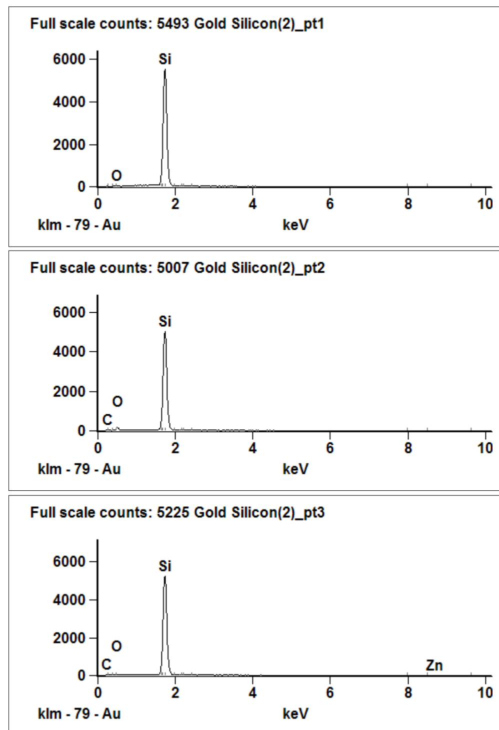

Figure 4.11: EDS spectra from a representative sample of metallized silicon (Point 1, 2, and 3 in Figure 4.10).

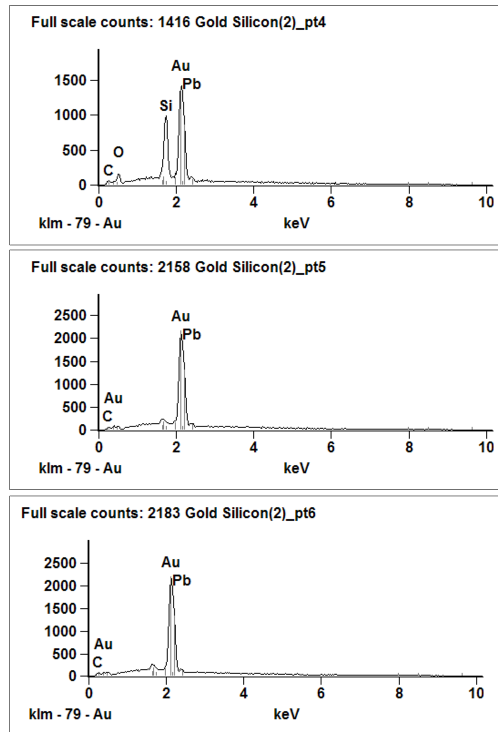

Figure 4.12: EDS spectra from a representative sample of metallized silicon (Point 4, 5, and 6 in Figure 4.10).

current-voltage responses measured for the silicon substrates are shown in Figures 4.13a and 4.13b. In figure 4.13a, the current-voltage response for a representative high resistivity silicon chip is shown. Likewise, in Figure 4.13b, the before and after metallization. Four-point probe measurements were performed using a hand-held 4-point cylindrical probe from Jandel Engineering. Each probe needle is spaced 0.1 cm apart. The device is also equipped with a test unit, which is a combined current source and digital voltmeter. A constant current was supplied to the sample during measurement. The 4-point probe included control software which allowed the user to save readings for the current/voltage, sheet resistance, bulk resistivity for wafer, and bulk resistivity. Aside from the resistance measurements made from prior to metallization, the sheet resistance of metal contacts was also measured. Values of some representative four-point probe measurements for the silicon substrates are shown in Table 4.7.

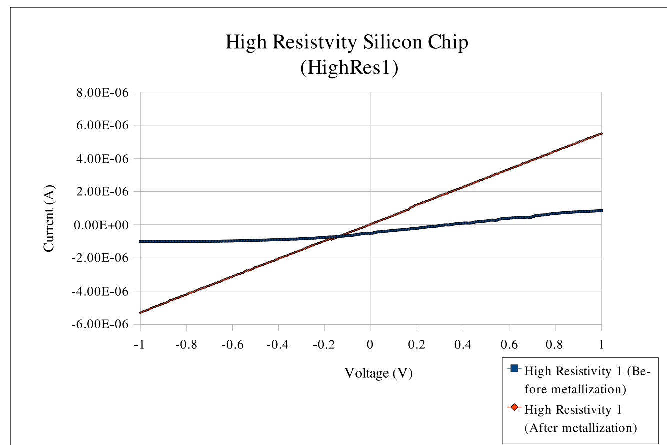

(a)

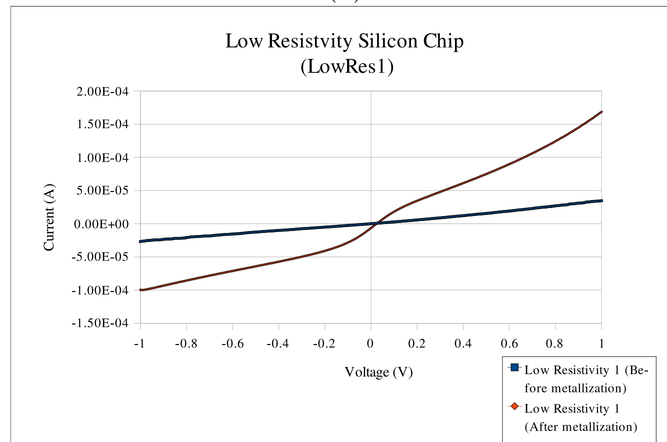

(b)

Figure 4.13: Current-Voltage response of silicon substrates for(a) High Resistivity silicon substrate, before and after metallization with gold (b) Low resistivity silicon of silicon substrate, before and after metallization with gold.

Table 4.7: Resistance measurements from four-point probe.

Silicon	Current range (A)	Voltage reading (mV)	Bulk resistivity (Ω·cm)	Sheet resistance (Ω/ square)
High resistivity	1 x 10^{-6}	163.234	22195.253	739841.782
Low resistivity	1 x 10^{-4}	2.375	3.230	107.649

4.3.2 Fabrication and experimental matrix for silicon sensor chips

The RCA cleaning method was used to treat the silicon substrates. In addition, both piranha and hydrofluoric acid were used to clean off any metal impurities and terminate the silicon surface with hydrogen bonds. Electrical characterization such as I-V curves, sheet resistance, and bulk resistivity were taken for each silicon substrates before sputtering and after annealing. An experimental matrix of for the silicon sensor chips made made in-house is shown in Table 4.8. The table details some of measurements and results for the chips fabricated in this work.

All of the chips have been treated with the standard RCA cleaning method. However, not all of the chips were treated with plasma cleaning and annealed, although it is recommended based upon the findings detailed in this section. As shown in Table 4.8, all of the chips fabricated in this portion of the work have ohmic contacts, and should, in theory, suitable for a Q-DLTS sensor; it was discovered that this is not entirely the case. In the table, all the chips made prior to test run number five were able to be tested with Q-DLTS. Both high resistivity and low resistivity silicon substrates were fabricated to examine the suitability as a gas phase Q-DLTS sensor. Test run numbers 5 to 10 were fabricated at the same time in order to minimize any sort of variations that may have occurred during handling. After RCA cleaning, these chips were subsequently cleaned in plasma before metallization. After sputtering, the chips were then transported in sample

bag, placed in a vacuum jar to minimize any contamination. Initially some samples were then annealed in a hydrogen atmosphere up to 300°C and held for about 10 minutes before cooling back down to room temperature. The I-V characteristics for all chips were ohmic; however, when tested for Q-DLTS, a large leakage current were observed. By passivating the chips in H_2 atmosphere, the presence of hydrogen in silicon could alter electrical properties of the material [77, 78].

To reduce the potential effects of annealing the samples in hydrogen atmosphere, the subsequent samples fabricated were annealed in argon atmosphere. Argon is an inert gas, so should not interfere with electrical properties of the silicon substrates. All of the fabrication processes leading up to annealing were done the same. Following this, the silicon chips were annealed in argon atmosphere and held at a temperature of 300°C for about 10 minutes before cooling back down to room temperature. The I-V measurements were carried out on the samples annealed under an argon atmosphere and ohmic contacts were verified for all of the chips. However, when tested for measurement of Q-DLTS spectra, a significant leakage currents were observed for all chips produced under argon annealing.

In order to determine what may have occurred, the chips were then removed from the process for further investigation. As shown in Table 4.8, test run numbers one through four were only treated with RCA and were not plasma cleaned or annealed. Since the first four test runs did produce chips suitable for Q-DLTS measurements, test run numbers 11 through 18 were fabricated using the same processes done for those chips. The samples from chip production runs 11 through 18 were all tested usingthe same material and electronic property measurement techniques. All of these chips were determined to have ohmic contacts and to have the properties consistent with those for the analogous types used in runs 1 through 4. Additionally, it is important to note that these chips were in fact manufactured from the same wafers used to produce the chips in runs 1 through 4. When these chips were subsequently tested in the MU Q-DLTS system, large leakage currents

were found for all of the chips (runs 11 to 18). These findings are consistent with those found for the chips produced in rungs 5 through 10 (except for run number 6). Some examples of the Q-DLTS response spectra for these chips are presented later in the chapter. After further examination of the fabrication and results from the sensor chip production trials, it is believed that the cause for an increased leakage current in the latter chips may have been due to a potential introduction of ionic contaminants in the deionized water.

As stated in Chapter 3, the RCA and cleaning recipe had been altered in this work, thes was done in order to decrease surface etching of the substrate from the chemicals and to improve worker safety. As a result, a significant amount of deionized water was used to dilute the concentrated chemical solutions used in the cleaning processes. However, since some of the RCA and cleaning methods involve boiling the in elevated temperature, it is believed that the deionized water may be a source that should be isolated. Ionic contamination during the fabrication process could also lead to increasing leakage in the device. It was suspected that deionized water maybe the source of problem in this case. In which by boiling chips in the hot water, contaminants may have diffused into the bulk or the surface [66].

The leakage current observed is the result that electrical charge rather than being integrated. And the leakage current is always going to be present, this is more so with a silicon based substrate. Although leakage current can be subtracted out, but as it can be seen in Figure 4.16 and 4.17, the Q-DLTS signals are susceptible to noises. Subtracting leakage current will introduce more statistical noises.

Table 4.8: Experimental matrix for silicon sensors.

Run	Name	Wet Cleaning Method	Plasma Cleaning	Annealing	Ohmic	Q-DLTS Measurement	Comment
1	LS2	Piranha, HF, & RCA	No	No	Yes	Yes	Broken

Continued on Next Page...

Table 4.8 – Continued

Run	Name	Wet Cleaning Method	Plasma Cleaning	Annealing	Ohmic	Q-DLTS Measurement	Comment
2	BSC5	Piranha, HF, & RCA	No	No	Yes	Yes	Broken
3	High Res/Al 1	Piranha, HF, & RCA	No	Ar	Yes	Yes	–
4	High Res/Al 2	Piranha, HF, & RCA	No	Ar	Yes	Yes	Peeled
5	HHR1	Piranha, HF, & RCA	Yes	H_2	Yes	No	High leakage
6	HHR2	Piranha, HF, & RCA	Yes	H_2	Yes	Yes	Broken
7	HLR1	Piranha, HF, & RCA	Yes	H_2	Yes	No	High leakage
8	HLR2	Piranha, HF, & RCA	Yes	H_2	Yes	No	High leakage
9	HighRes 1	Piranha, HF, & RCA	Yes	Ar	Yes	No	High leakage
10	HighRes 2	Piranha, HF, & RCA	Yes	Ar	Yes	No	High leakage
11	LowRes1	Piranha, HF, & RCA	No	No	Yes	No	High leakage
12	LowRes2	Piranha, HF, & RCA	No	No	Yes	No	High leakage
13	LowRes3	Piranha, HF, & RCA	No	No	Yes	No	High leakage

Continued on Next Page...

Table 4.8 – Continued

Run	Name	Wet Cleaning Method	Plasma Cleaning	Annealing	Ohmic	Q-DLTS Measurement	Comment
14	LowRes4	Piranha, HF, & RCA	No	No	Yes	No	High leakage
15	High Res 1	Piranha, HF, & RCA	No	No	Yes	No	High leakage
16	High Res 2	Piranha, HF, & RCA	No	No	Yes	No	High leakage
17	High Res 3	Piranha, HF, & RCA	No	No	Yes	No	High leakage
18	High Res 4	Piranha, HF, & RCA	No	No	Yes	No	High leakage

Figure 4.14: Resistance testing using transmission line method.

4.3.3 Q-DLTS signals for silicon sensor chips

Q-DLTS signals were collected for selected target species on the sensor chips. Target species included, CO_2, N_2, Ar, isopropanol, and ethanol. Initial testings were performed both in an aluminum enclosure and in the stainless steel bell jar. The results of these two setups will be discussed here.

The aluminum enclosure was connected to a common ground of the Q-DLTS device. Silicon sensor chips were measured in atmosphere pressure, with different target species introduced into the enclosure and measured at selected times. The processes for data collection involved:

1. Regeneration of the sample by heating up the substrate up to 40°C for 5 to 10 minutes, then cool down to room temperature.

2. An initial measurement was taken with just the presence of air in the enclosure. This would serve as a baseline for other target species.

3. 1 mL of 1-propanol was introduced into the enclosure. Data were collected for 1-propanol after placing in aluminum enclosure for 15 minutes.

4. Before introducing the next target species, the substrate was regenerated by

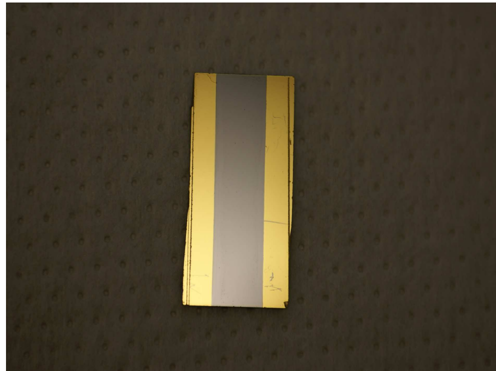

(a)

(b)

(c)

(d)

Figure 4.15: In-house silicon sensor chips designs. These designs took in consideration the exposed subsrate surface for sensing and the resistivity of metal contacts. (a) 3/16" silicon sensing surface, (b) 1/8" silicon sensing surface, (c) 1/2" silicon sensing surface, and (d) 3/4" silicon sensing surface.

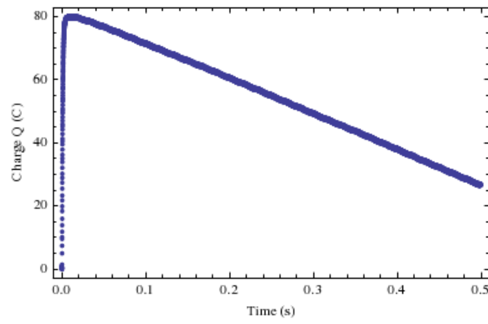

(a)

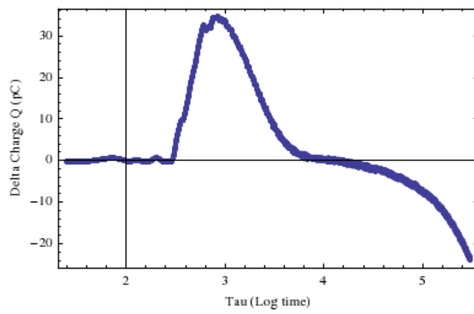

(b)

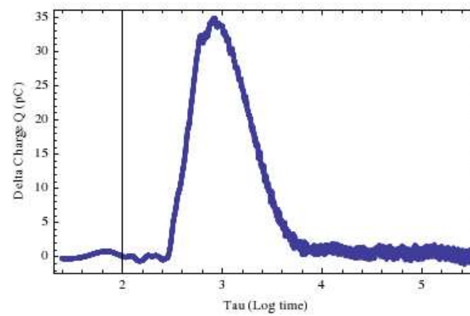

(c)

Figure 4.16: A representative of leakage current observed for high resistivity silicon substrate (a) raw data, (b) analyzed Q-DLTS signal, and (c) analyzed Q-DLTS signal after subtracted the leakage current.

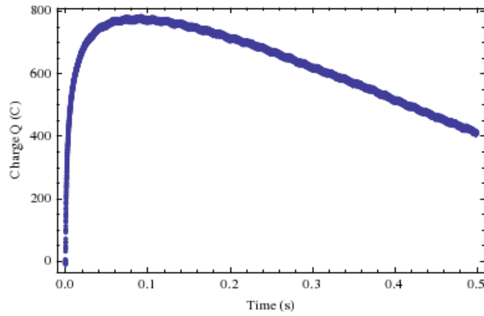

(a)

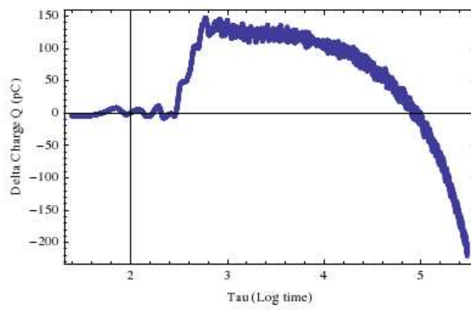

(b)

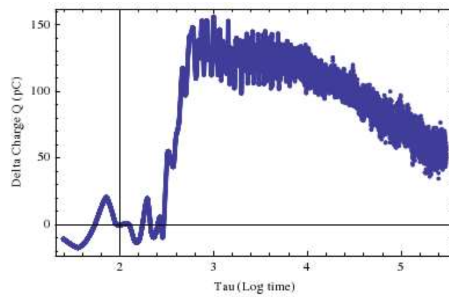

(c)

Figure 4.17: A representative of leakage current observed for high resistivity silicon substrate (a) raw data, (b) analyzed Q-DLTS signal, and (c) analyzed Q-DLTS signal after subtracted the leakage current.

heating up to 35 - 45°C for another 5 to 10 minutes.

5. Background (air) was measured again before the next target species.
6. Additional target species measured were isopropanol, methanol, butanol, ethanol and water.

Figure 4.18 shows preliminary data taken for Q-DLTS signals. The target species include 1-propanol, isopropanol, methanol, butanol, ethanol, and water. These target species are measured in the presence of air. It was observed that air has higher charge collected in comparison to the introduced target species. 99.99% of air is composed of N_2 (78.084%), O_2 (20.947%), Ar (0.934%), and CO_2(0.033%). The rest are Ne, He, Kr, SO_2, CH_4, H_2, N_2O, Xe, NO_2, O_3, CO, NH_3, and I_2. It is possible that there is a process of adsorption and desorption at the surface. What is adsorbed initially on the surface, may be in competition with the alcohol molecules. In this case, contribution from air may be decreasing with the presence of target species. As shown in Figure 4.18, some of the peaks have shifted and some have decreased or increased in charge collection. Namely, peak location at $\tau = 3.5$, the magnitude of charge collection has decreased with the presence of target species. On the other hand, peak magnitude around $\tau = 1.5$ to $\tau = 2.5$ have increased as the complexity of carbon, hydrogen, and oxygen atoms varied.

To understand the contribution of target species and not background air, Q-DLTS signal of air is subtracted out. By taking this approach, some additional noises and errors could be introduced. Figure 4.19 shows Q-DLTS signals after subtraction of air, which was denoted as color red in Figure 4.18. Negative portion of Figure 4.19 means, that charge collected was less. In other words, the deep-level traps correspond to certain emission rates have less concentration. In both Figure 4.18 and 4.19, a significant peak of charge collected was observed. This curve corresponds to post-removal of methanol from aluminum enclosure and sensor chip was regenerated by heating. Judging by the similarity in shape to the previous

measurements, it would be possible that faster emission rates were due to elevated temperature of sensor substrate.

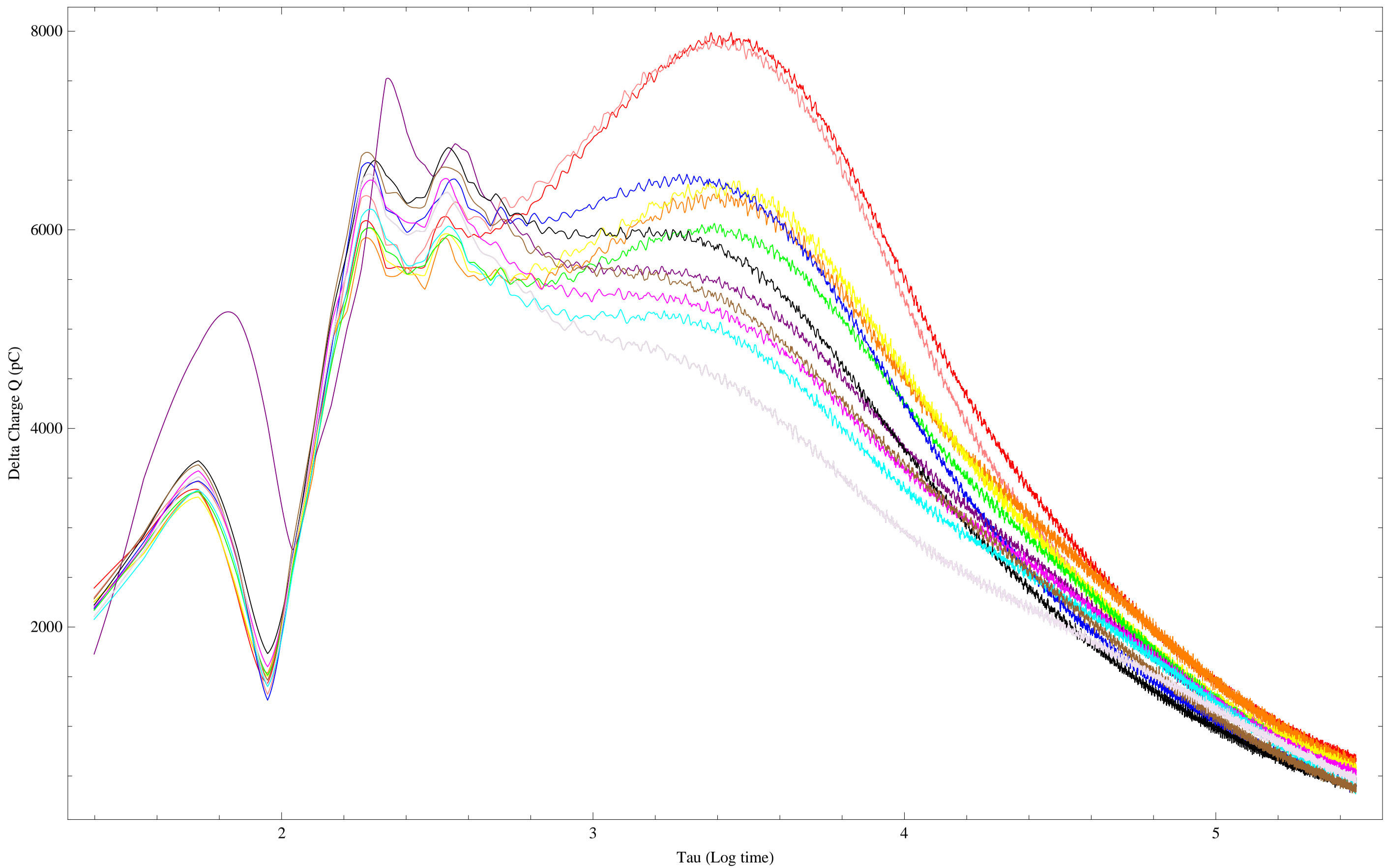

Figure 4.18: Q-DLTS signals of various target species. Red→ air, Pink→ 1-propanol, Orange→ 1-propanol removed and substrate regenerated with heat, Yellow→ isopropanol, Green→ isopropanol removed and substrate regenerated with heat, Blue→ methanol, Purple→ methanol removed and substrate regenerated with heat, Black→ butanol, Magenta→ butanol removed and substrate regenerated with heat, Cyan→ ethanol, Gray→ ethanol removed and substrate regenerated with heat, Brown→ water, Light purple→ water removed and substrate regenerated with heat.

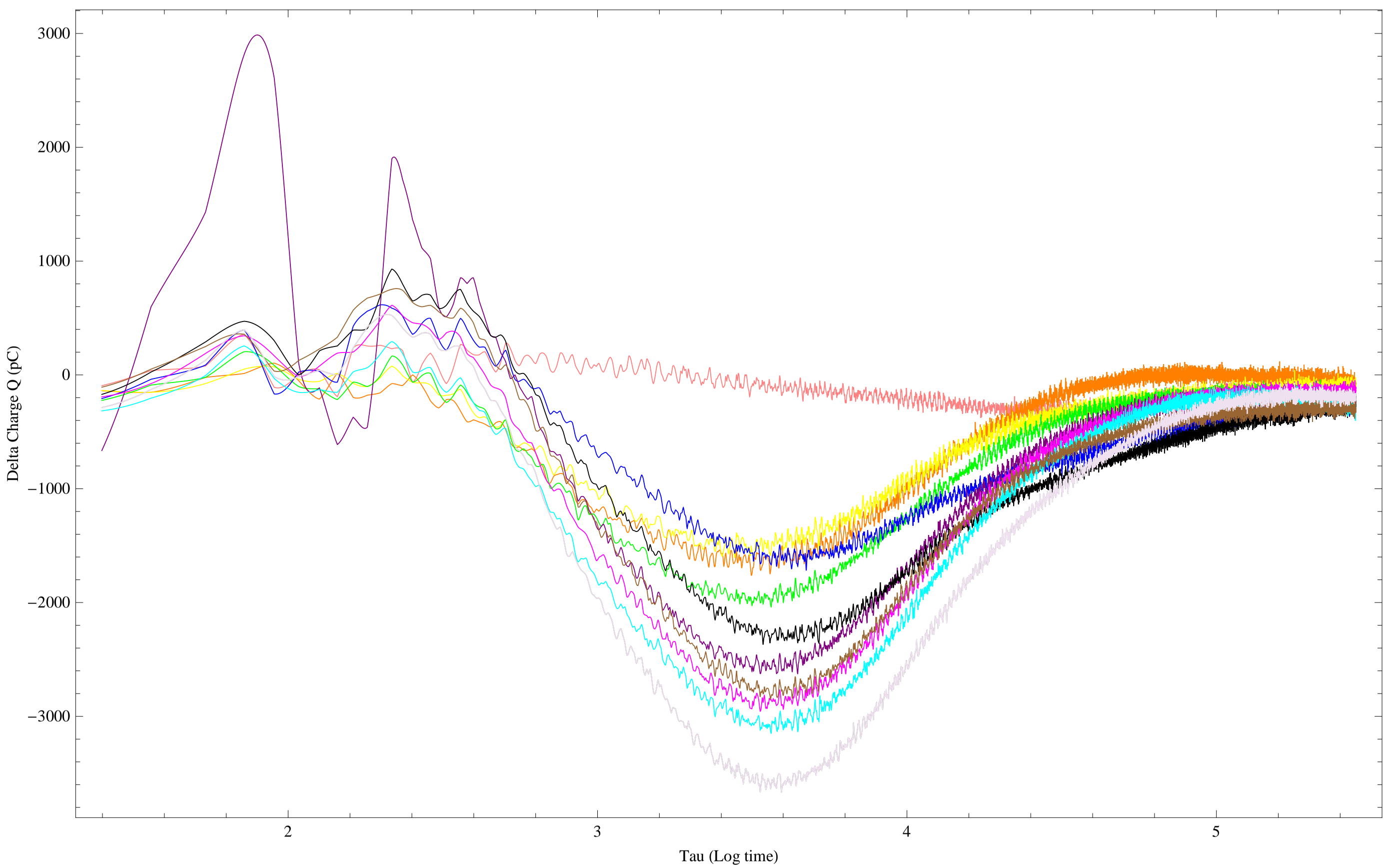

Figure 4.19: Q-DLTS signals of various target species after substraction background (air). Pink→ 1-propanol, Orange→ 1-propanol removed and substrate regenerated with heat, Yellow→ isopropanol, Green→ isopropanol removed and substrate regenerated with heat, Blue→ methanol, Purple→ methanol removed and substrate regenerated with heat, Black→ butanol, Magenta→ butanol removed and substrate regenerated with heat, Cyan→ ethanol, Gray→ ethanol removed and substrate regenerated with heat, Brown→ water, Light purple→ water removed and substrate regenerated with heat.

These measurements were made in atmospheric pressure and in a shielded metal enclosure. Results from preliminary measurements shown, the sensitivity of QF^{TM} sensor chips to composition in the air, required that the sensor chips to be measured in a more controlled environment. A vacuum system was constructed to provide an environment with minimal contamination and a fine control of pressure. Target species for preliminary testing of this set up includes N_2, Ar, CO_2, CH_4, isopropanol, and acetone. Data collection for target species followed the procedures below:

1. Connect the QF^{TM} sensor chips to the electrical connections inside the vacuum bell jar. Pump down volume to the lowest pressure possible. Meanwhile, heat the bell jar for extended time to outgas, and cool down to room temperature the following day.

2. Record the pressure and temperature before data collection. The lowest pressure recorded was about 10^{-6} Torr and temperature around 72.5 °F.

3. A baseline measurement is taken each time between target species is introduced. Pressure and temperature are recorded.

4. Target species were introduced incrementally to the selected pressure range, each differed by an order of magnitude. At beginning of every measurement, pressure and temperature are recorded.

5. For gaseous target species, the last pressure measured is at atmospheric pressure. For liquid target species, each pressure increment corresponds to 1 mL of liquid introduced into the vacuum system.

Analyzed Q-DLTS signals for nitrogen gas are shown in Figure 4.20. This set of data is taken for nitrogen gas. For reproducibility check, vacuum system is first pumped down to about 10^{-6}, and brought to atmosphere before pumped back down again. Due to the introduction of target species, charge collection on

QF^{TM} chip varied with pressure changes. As shown in Figure 4.20a, significant charge increase is observed between 0.1 torr and 10 torr. This may indicate an increasing amount of nitrogen molecules present on the sensor surface. A trend of saturation was initially observed near the atmospheric pressure, this is shown by the magnitude charge collected. However, the black curve in Figure 4.20a shows presence of nitrogen gas at atmospheric pressure, taken after one hour. This curve shows charge collected from surface is still growing; indicating it may take some time for nitrogen population adsorbed on sensor surface to come to an equilibrium. Similar trend is observed in Figure 4.20c, except the same QF^{TM} chip is subjected to from atmospheric pressure to baseline. About 10 to 15 minutes was waited between each measurement at the select pressure range. However, as shown in Figure 4.20a and 4.20c, longer waiting period maybe required for sensor surface to come to a steady-state. Figure 4.20b and 4.20d looked at the magnitude of charge collection after background is subtracted.

Additional Q-DLTS measurements were also taken for CO_2 and CH_4 with the same QF^{TM} sensor chip. These will be shown in Figures 4.21 and 4.22. Similar trend was observed with CO_2 gas for Q-DLTS spectra and charge collected. It was initially postulated that, a unit cell of sensor surface may be related to the ability to discern the target species. As mentioned in Chapter 2, a unit cell spacing of silicon is about 5.43Å, where as CO_2 gas molecular diameter is around 4.64Å; CH_4 gas molecular diameter is in the proximity of 4.2 Å; and N_2 gas molecular diameter is about 3.8Å [79]. The molecular diameter of these gas molecules in this case, were all quite a bit smaller than a unit cell of silicon lattice. It was suspected that the occupancy of gas molecules on silicon surfaces may be within a unit cell. In other words, resolution for sensor chips made from silicon may be less than other semiconducting materials of smaller lattice spacing. Because any molecules that landed on silicon's surface may just be treated as a single unit, where as materials of tighter lattice spacing may be able to discern the variation.

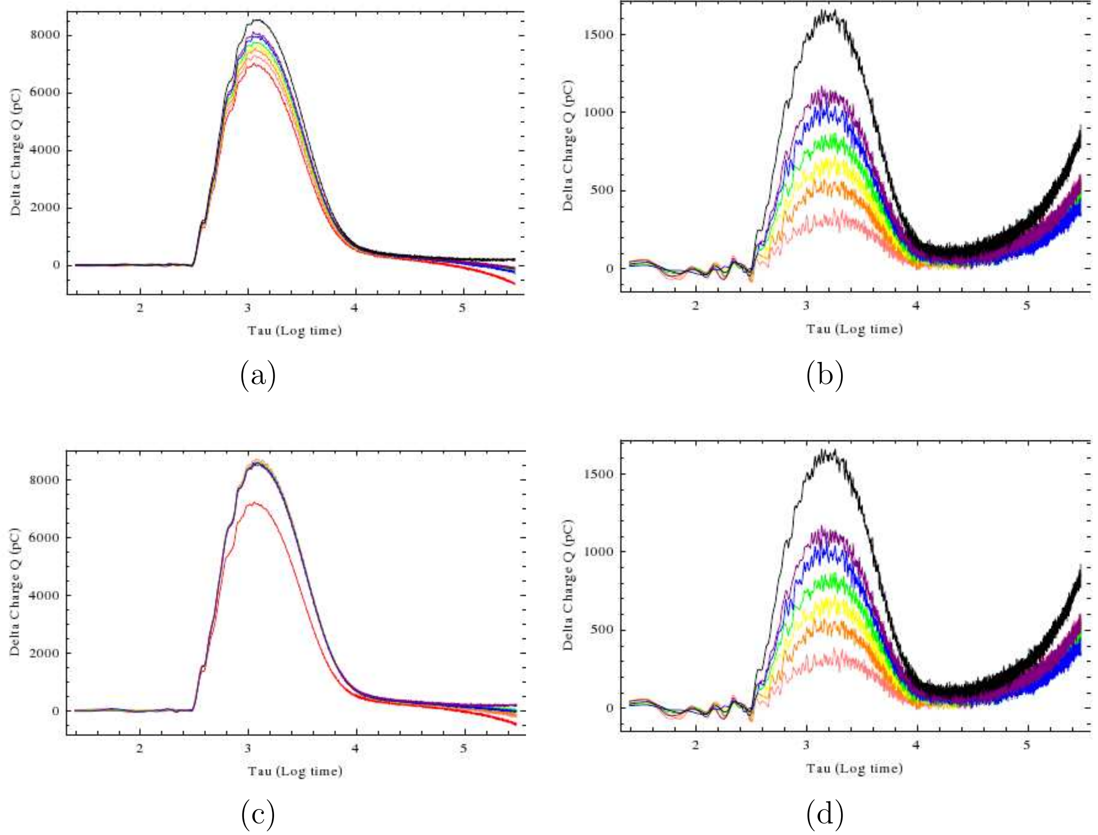

Figure 4.20: Q-DLTS signals measured in vacuum system for sensor chip BSC5 (a) N_2 gas introduced from 0.1 torr to atmospheric pressure, (b) same as (a) but background is subtracted, (c) N_2 gas is pumped down from atmospheric pressure to 0.1 torr, (d) same as (c) but background is subtracted. Red→ 0.043E-3 torr, Pink→ 0.13 torr, Orange→ 1.03 torr, Yellow→ 10.04 torr, Green→ 99.5 torr, Blue→ 300 torr, Purple→ 740 torr, Black→ 740 torr after 1 hour.

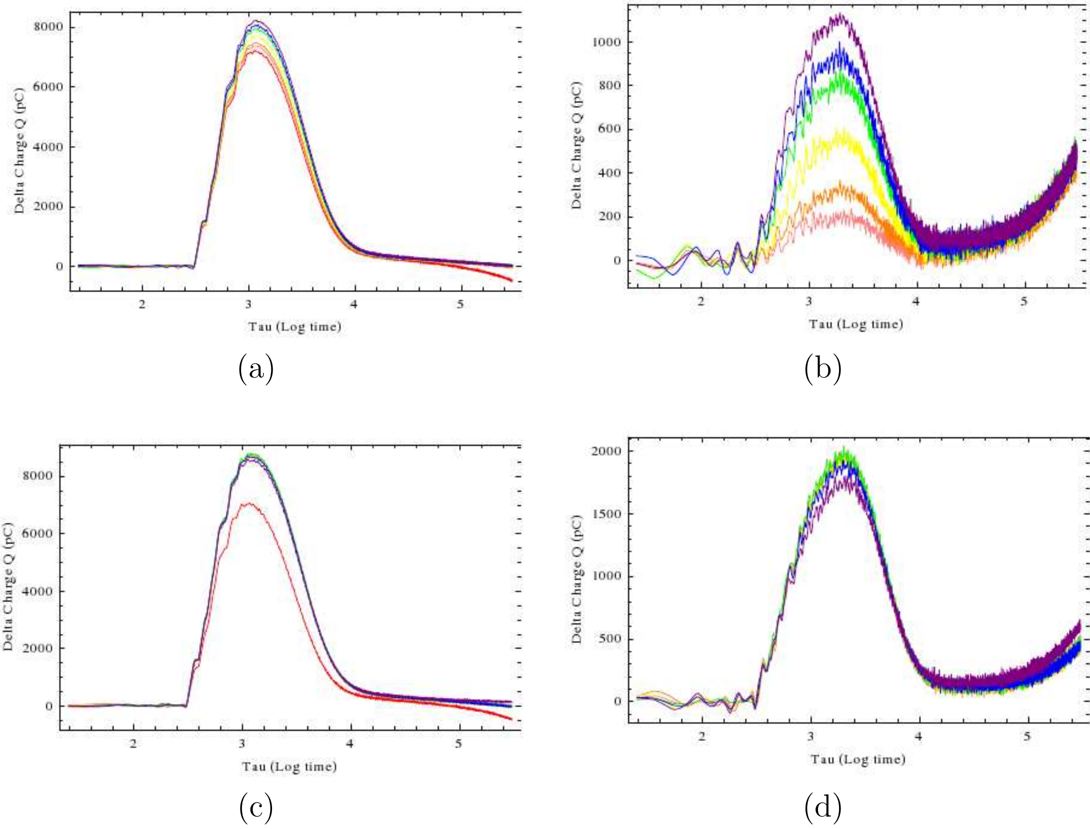

Figure 4.21: Q-DLTS signals measured in vacuum system for sensor chip BSC5 (a) CO_2 gas introduced from 0.1 torr to atmospheric pressure, (b) same as (a) but background is subtracted, (c) CO_2 gas is pumped down from atmospheric pressure to 0.1 torr, (d) same as (c) but background is subtracted. Red→ 0.043E-3 torr, Pink→ 0.11 torr, Orange→ 0.98 torr, Yellow→ 10.05 torr, Green→ 99.62 torr, Blue→ 298.5 torr, Purple→ 740 torr, Black→ 740 torr after 1 hour.

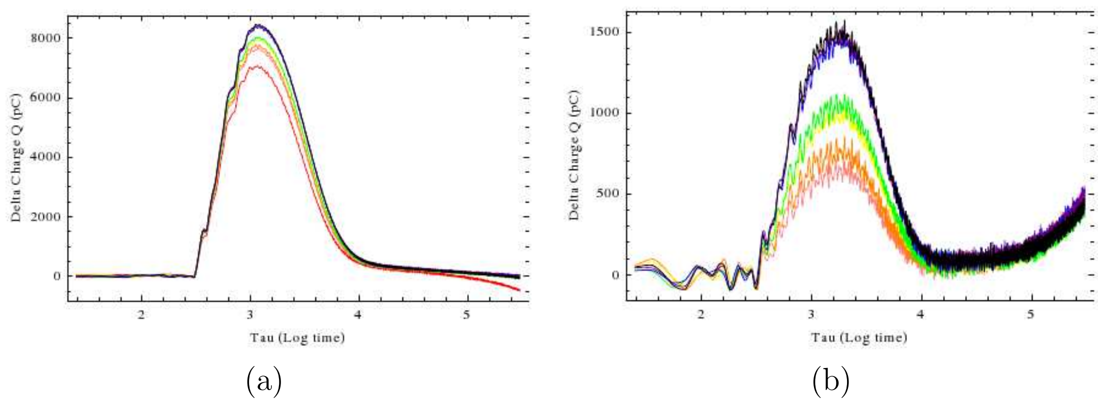

Figure 4.22: Q-DLTS signals measured in vacuum system for sensor chip BSC5 (a) CH_4 gas introduced from 0.1 torr to atmospheric pressure, (b) same as (a) but background is subtracted. Red→ 2.3E-3 torr, Pink→ 0.11 torr, Orange→ 0.98 torr, Yellow→ 10.05 torr, Green→ 99.62 torr, Blue→ 298.5 torr, Purple→ 740 torr, Black→ 740 torr after 1 hour.

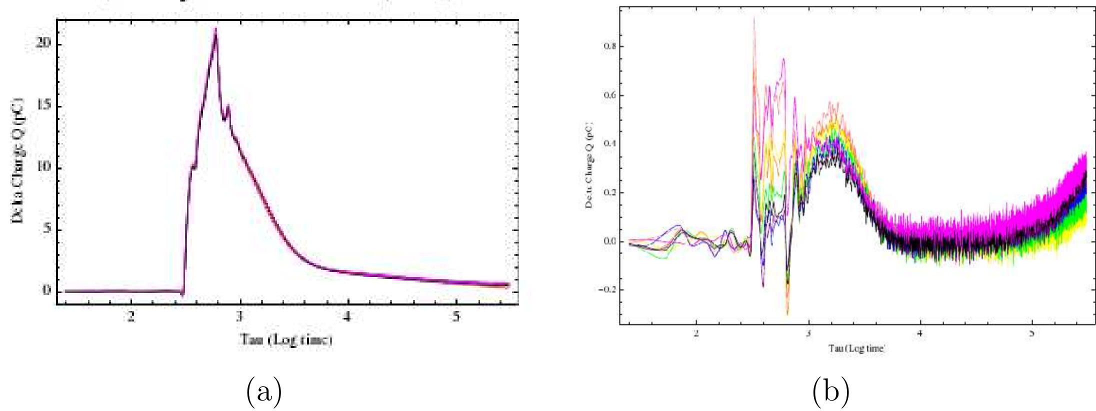

(a) (b)

Figure 4.23: Q-DLTS signals measured in vacuum system for sensor chip LS2. A mixture of 5% Ar and 95% N_2 gases. Gas mixture was sat overnight for a more uniform mixing. The mixture is initially at atmospheric pressure and pumped down to the specified pressure. (a) Measurements from 0.01 torr to atmospheric pressure, (b) same as (a) but background is subtracted. Red→ 1E-5 torr, Pink→ 0.01 torr, Orange→ 0.05 torr, Yellow→ 0.11 torr, Green→ 0.54 torr, Blue→ 1.08 torr, Purple→ 10.35 torr, Black→ 42.77 torr, and Magenta→ 102.79 torr

Chapter 5

Conclusions and future work

A fabrication and testing process for QF^{TM} sensor chips based on various semiconductor substrates has been demonstrated in this work, along with some initial measurements of Q-DLTS spectra. There are many complex issues to be addressed in order to develop a deployable QF^{TM} based sensor. A few observations will be discussed in the following sections, based upon the empirical findings and analysis from this work.

Material selection - The choice of substrate materials was a critical step. Silicon was used mainly in this work, although silicon carbide and sapphire substrates had also been considered. In terms of cost, silicon is cheap and widely available, so it would be ideal for both research development and commercialization. The versatility of silicon also makes it a possible candidate to be manufactured into a disposable unit. The cost for sapphire and silicon carbide is significantly higher but, commercialization is still possible. QF^{TM} sensor chips made out of sapphire or silicon carbide may be less dispensable; regeneration of the substrate surfaces should be considered in between each use. Out of all three materials, silicon substrates had the largest lattice spacing. Thus, the selectivity of target species may be sacrificed because of how molecules (or cluster of molecules) were treated on the substrate surface. Sapphire and silicon carbide substrates on the other hand, have a tighter lattice spacing. The ability to discern target species adsorbed on the surface is still an area to be addressed. Among the three substrates, silicon is

also most susceptible to damage during handling (direct impact). The hardness of bulk silicon material is much less than that of sapphire and silicon carbide. As previously noted, several silicon sensor chips fabricated in this work were damaged before additional measurements could be made. Small bandgap semiconductors (i.e. silicon) are also more likely to have a higher leakage current at room temperature than wide bandgap materials. Hence, electrons could tunnel through the potential barrier by the thermal stimulation even at room temperature and contribute to signal noise when measuring the decay current from electron traps.

Material processing - Material processing was also relevant to the performance of QF^{TM} sensor chips as observed in this work. Hydrogen termination was typically used for stable surface termination. Fluorine termination of greater electronegativity was also considered. However, analysis of the literature search had suggested that fluorine termination could be less stable than hydrogen termination [68, 69]. Attack of air (oxidation) to the substrate surface was more predominant than hydrogen termination. A higher leakage current was also observed on some of the sensor chips. Leakage current is an inherent problem in any kind of electronic devices. Often times, the actual signals measured were substantially larger such that the leakage current was negligible. A wet chemical cleaning process, commonly used in the semiconductor fabrication industry, was used for removal of substrate surface contaminants. The chemical solutions used for cleaning process, could potentially etch substrate surfaces leaving undesirable surface roughness. Therefore, the mixing ratios of chemical cleaning solutions have been changed in this work to avoid influences of surface roughness [66, 70, 71]. Metallization on the substrate surface is another critical element which would affect metal-semiconductor contact. Some of the metals considered are susceptible to oxygen attack, which included: titanium, aluminum, and zirconium. Discontinuity between deposited metal layers on the substrate surface would act to inhibit current transport at the metal-semiconductor interface.

Testing environment - A controlled testing environment is critical to the QF^{TM} sensor chips. It was noted that QF^{TM} spectra measured for targets in atmosphere were likely sensitive to both the target species and the components of atmospheric air. Thus, it was difficult to isolate a characteristic spectra due to charge traps formed by the target species on the substrate. It is believed that there may have been adsorption and desorption processes occurring at the sensor surface. A high vacuum chamber was constructed to provide a contaminant-free and temperature controlled environment. The vacuum chamber was made from stainless steel; this provided electrical shielding to minimize noise interference. The vacuum chamber was also constructed to provide a controlled (measured) concentration of gas species. Quantitative information of detectable species could be obtained through this process. Characterizing of controlled concentration for gas species in the chamber was examined. Calibration of the vacuum system for gas species at various concentrations was verified using a residual gas analyzer [80].

Data analysis - Data analysis of Q-DLTS signals was approached in three different ways. The rate window approach was first used. This approach was conventionally used on DLTS and is similar to transient spectroscopy techniques. A computer code was written as part of this work in order to generate the Q-DLTS spectra. The experimental tests in this work have shown that it was capable of producing the same spectra as produced by a commercially available Q-DLTS system (ASMEC). Discrete Fourier transform analysis was also examined. The purpose was to explore different analysis techniques to explain the physical phenomenon. However, since the raw data were not periodic in nature, discrete Fourier transform analysis could not be used. Fitting of exponential decay curves to the charge decay measurements was also explored. This data fitting method could be used to calculate the emission rates from trap centers. One could relate the calculated emission rate to peak position (in τ) on a Q-DLTS signal spectrum (ie. the emission rate is the inverse of τ). However, when carried out in this work, this approach was

found to rapidly become computationally expensive as more complicated exponential functions, containing multiple emission rates, were considered.

Ongoing research would still be required in many areas of this project. Various wide bandgap materials, terminating bonds to substrate surface, optimal sensor chip metallization are still topics of interest for further investigation.

Semiconductor materials, preferably with tighter lattice spacing could provide better resolution for discerning adsorbed atoms on a substrate surface. Nevertheless, there are many materials that could be explored: GaN, AlN, diamond, polymorphs of SiC, InN, etc. Of the materials which could be tested, the most important consideration should be to characteristics relevant to the sensor's performance, such as electrical, mechanical, optoelectronic, and thermal properties.

Surface states of the semiconductor should be addressed in future research. Examples include, understanding of surface termination for the bulk crystal lattice, various terminating species, and treatment process for termination. A physical theory describing the surface states should be derived for comparison of theoretical and experimental values. Sources contributing to leakage current should also be further investigated. Hydrogen and ionic contamination in the water were potential sources of leakage current in the present work.

Additional data analysis techniques and algorithms should continue to be explored for optimal representation and recognition of measured spectra. For benchmark purposes, a computer code was initially developed in Mathematica®. However, to minimize the overhead cost of Mathematica® and computer requirements, an in-house computer code should be developed. A pattern recognition algorithm may also be considered for examination of a Q-DLTS signal spectrum. A broad spectrum shape could first be identified from the built-in Q-DLTS library using a coarser scale pattern matching, followed by a finer scale pattern matching. This approach may allow users to zoom in at various regions of interest and lessen the computational time.

The detection of chemical agents using a solid-state, gas-phase sensor was examined in this dissertation. A charge-based deep level transient spectroscopy system was used to characterize the deep level states created by targeted species on the sensor surface. The critical components for the development of such sensor technology have been examined. These include selection of appropriate semiconductor substrates and metal contacts for ohmic contacts, fabrication protocols and metallic pattern designs for optimal signals, development of sensor technology measurement protocols, and testing of sensor chips under a controlled environment. The substrate materials tested in this work include silicon, silicon carbide, and sapphire. Several chemical agents were selected for testing, which included: water, 1-propanol, isopropanol, methanol, butanol, ethanol, nitrogen gas, argon gas, and methane gas. The testing of the sensor chips was performed in both atmospheric air and in a controlled, high vacuum environment, isolated from the presence of other species. The experimental measurements made in this work have shown some dependency of targeted species concentrations and pressures with electrical charge collected from trap centers.

Bibliography

[1] D. V. Lang. Deep-level transient spectroscopy: A new method to characterize traps in semiconductors. *J. Appl. Phys.*, 45:3023–3032, 1974.

[2] K. I. Kirov and K. B. Radev. A simple charge-based DLTS technique. *Phys. Stat. Sol. (a)*, 63:711–716, 1981.

[3] D. Diamond. *Principles of Chemical and Biological Sensors*. John Wiley & Sons, Inc., 1998.

[4] J. Fraden. *Handbook of Modern Sensors: Physics, Designs, and Applications*. Birkhuser, 2004.

[5] J. Stranks. *Human Factors and Behavioural Safety*. Butterworth-Heinemann, 2007. Chapter 2: Human sensory and perceptual processes.

[6] J. S. Wilson. *Sensor Technology Handbook*. Newnes, 1st edition, 2005.

[7] S. P. Mohanty and E. Kougianos. Biosensors: A tutorial review. *IEEE Pot.*, 25:35–40, 2006.

[8] S. Middelhoek and S. A. Audet. *Silicon Sensors*. Academic Press, 1989.

[9] R. W. A. Scarr and R. A. Setterington. Thermistors, their theory, manufacture, and application. *IRE Transactions on Component Parts*, 3:6–21, 1961.

[10] R. G. Jackson. *Novel Sensors and Sensing*. CRC Press, 2004.

[11] B. G. Streetman and S. K. Banerjee. *Solid State Electronic Devices*. Pearson Prentice Hall, 6 edition, 2006.

[12] B. G. Yacobi. *Semiconductor Materials - An Introduction to Basic Principles*. Kluwer Academic/Plenum Publishers, 2003.

[13] S. Capone, A. Forleo, L. Francioso, R. Rella, P. Siciliano, J. Spadavecchia, D. S. Presicce, and A. M. Taurino. Solid state gas sensors: State of the art and future activities. *J. Optoelectron. Adv. Mater.*, 5:1335–1348, 2003.

[14] Y. Shimizu and M. Egashira. Basic aspects and challenges of semiconductor gas sensors. *MRS Bull.*, 24:18–24, 1999.

[15] M. A. Prelas, T. K. Ghosh, R. V. Tompson, D. S. Viswanath, and S. K. Loyalka. U. S. Patent No. 11,639,405, January 10 2008.

[16] E. P. McCluskey, R. Grzybowski, and T. Podlesak, editors. *High Temperature Electronics*. CRC Press, 1997.

[17] M. N. Yoder. Wide bandgap semiconductor materials and devices. *IEEE Trans. Electron Dev.*, 43:1633–1636, 1996.

[18] J. C. Zolper. A review of junction field effect transistors for high-temperature and high-power electronics. *Solid-State Electron.*, 42:2153–2156, 1998.

[19] D. L. Dreifus and B. A. Fox. Active devices. In M. A. Prelas, G. Popovici, and L. K. Bigelow, editors, *Handbook of Industrial Diamonds and Diamond Films*, pages 1043–1072. Marcel Dekker, Inc., 1998.

[20] M. C. Gupta and J. Ballato. *Handbook of Photonics*, chapter 4. CRC Press, 2 edition, 2006.

[21] M. J. Madou. *Fundamentals of Microfabrication - The Science of Miniaturization*. CRC Press, 2nd edition, 2002.

[22] S. Kasap and P. Capper, editors. *Springer Handbook of Electronic and Photonic Materials*. Springer, 2006.

[23] S. E. Saddow and A. Agarwal, editors. *Advances in Silicon Carbide - Processing and Applications*. Artech House, Inc., 2004.

[24] J. Guo, D. E. Ellis, and D.J. Lamp. Electronic structure and energetics of sapphire (0001) and (1102) surfaces. *Phys. Rev. B*, 45:647–656, 1992.

[25] D. K. Schroder. *Semiconductor Material and Device Characterization*. John Wiley & Sons, Inc., 3rd edition, 2006.

[26] J. Bardeen. Surface states and rectification at a metal semi-conductor contact. *Phys. Rev.*, 71:717–727, 1947.

[27] S. M. Sze and K. K. Ng. *Physics of Semiconductor Devices*. Wiley, 3rd edition, 2007.

[28] C. G. B. Garrett and W. H. Brattain. Physical theory of semiconductor surfaces. *Phys. Rev.*, 99:376–387, 1955.

[29] W. Mönch. *Semiconductor Surfaces and Interfaces*. Springer, 3rd edition, 2001.

[30] V. G. Bordo and H.-G. Rubahn. *Optics and Spectroscopy at Surfaces and Interfaces*. Wiley-Vch, 2005.

[31] A. Zangwill. *Physics at Surfaces*. Cambridge University Press, 1988.

[32] M. Werner. Ohmic contacts. In J. G. Webster, editor, *Wiley Encyclopedia of Electrical and Electronics Engineering*, volume 15. Wiley, 1999.

[33] E. H. Rhoderick. *Metal-Semiconductor Contacts*. Clarendon Press, 1978.

[34] B. Pellegrini. Properties of silicon-metal contacts versus metal work-function, silicon impurity concentration and bias voltage. *J. Phys. D: Appl. Phys.*, 9:55–68, 1976.

[35] Badih El-Kareh. *Silicon Devices and Process Integration - Deep Submicron and Nano-Scale Technologies*. Springer, 2009.

[36] A. Kikuchi. Calculation of ohmic contact resistance at a metal/silicon interface. *Phys. Stat. Sol. (a)*, 175:623–629, 1999.

[37] M. V. Sullivan and J. H. Eigler. Electroless nickel plating for making ohmic contacts to silicon. *J. Electrochem. Soc.*, 104:226–230, 1957.

[38] M. P. Lepselter. U.S. Patent No. 3,274,670, September 27 1966.

[39] M. J. Rand. U.S. Patent No. 3,889,359, June 17 1975.

[40] Y. C. Yu. Electron tunneling and contact resistance of metal-silicon contact barriers. *Solid-State Electron*, 13:239–247, 1970.

[41] G. Pensl, F. Ciobanu, T. Frank, M. Kreiger, S. Reshanov, F. Schmid, and M. Weidner. SiC material properties. *J. High Speed Electron. Sys.*, 15:705–745, 2005.

[42] J. Crofton, L. M. Porter, and J. R. Williams. The physics of ohmic contacts to SiC. *Phys. Stat. Sol. (b)*, 202:581–603, 1997.

[43] L. M. Porter and R.F. David. A critical review of ohmic and rectifying contacts for silicon carbide. *Mater. Sci. Eng., B*, 34:83–105, 1995.

[44] F. Roccaforte, F. La Via, and V. Raineri. Ohmic contacts to SiC. *Int. J. High Speed Electron. Syst.*, 15:781–820, 2005.

[45] T. V. Blank and Y. A. Gol'dberg. Mechanisms of current flow in metal-semiconductor ohmic contacts. *Semiconductors*, 41:1281–1308, 2007.

[46] A. Addamiano. U. S. Patent No. 3,510,733, May 5 1970.

[47] G. Pope, O. Guy, and P. A. Mawby. Comparison of different surface pre-treatments to n-type 4H-SiC and their effect on the specific contact resistance on Ni ohmic contacts. *Mater. Sci. Forum*, 457-460:833–836, 2004.

[48] S. P. Murarka. Self-aligned silicides or metals for very large scale integrated circuit applications. *J. Vac. Sci. Technol., B*, 4:1325–1331, 1986.

[49] S. Y. Han and J. Lee. Effects of interfacial reactions of electrical properties of Ni contacts on lightly doped n-type 4H-SiC. *J. Electrochem. Soc.*, 149(3):G189–G193, 2002.

[50] R. T. Tung. Recent advances in schottky barrier concepts. *Mater. Sci. Eng., R*, 35:1–138, 2001.

[51] F. Roccaforte, F. La Via, V. Rainer, R. Pierobon, and E. Zanoni. Richardsons constant in inhomogeneous silicon carbide Schottky contacts. *J. Appl. Phys.*, 93(11):9137–9144, June 2003.

[52] S. Liu, K. Reinhardt, C. Severt, and J. Scofield. Thermally stable ohmic contacts on n-type 6H- and 4H-SiC based on silicide and carbide. *Inst. Phys. Conf. Ser.*, 142:589–592, 1996.

[53] K. Otsuka, H. Ishida, and T. Tsuboi. Study of Al - Al2O3 bond interface. *J. Am. Ceram. Soc.*, 70(7):C154–156, 1997.

[54] S. Suenaga, M. Koyama, S. Arai, and M. Nakahashi. Solid-state reactions of the Ag-Cu-Ti thin film Al2O3 substrate system. *J. Mater. Res.*, 8:1805–1811, 1993.

[55] G. Bernhardt, C. Silvestre, N. LeCursi, S. C. Moulzolf, D. J. Frankel, and R. J. Lad. Performance of Zr and Ti adhesion layers for bonding of platinum metallization to sapphire subsrates. *Sens. Actuators, B*, 77:368–376, 2001.

[56] C. T. Sah. Bulk and interface imperfections in semiconductors. *Solid-State Electron.*, 19:975–990, 1976.

[57] B. W. Wessels. Determination of deep levels in Cu-doped GaP using transient-current spectroscopy. *J. Appl. Phys.*, 47:1131–1133, 1976.

[58] A. W. Farmer, C. D. Lamp, and J. M. Meese. Charge transient spectroscopy. *Appl. Phys. Lett.*, 41:1063–1065, 1982.

[59] B. M. Arora, S. Chakravarty, and S. Subramanian. Deep-level transient charge spectroscopy and Sn donors in Al(x)Ga(1-x)As. *J. Appl. Phys.*, 73:1802–1806, 1993.

[60] http://www.cree.com, Accessed Date: May 12, 2009.

[61] http://www.universitywafer.com, Accessed Date: May 12, 2009.

[62] S. Wartewig. *IR and Raman Spectroscopy.* Wiley-Vch, 2003.

[63] J. Goldstein, D. Newbury, D. Joy, C. Lyman, P. Echlin, E. Lifshin, L. Sawyer, and J. Michael. *Scanning Electron Microscopy and X-Ray Microanalysis.* Springer, 3rd edition, 2003.

[64] www.jandel.co.uk, Accessed Date: May 10th, 2009.

[65] P. Van Zant. *Microchip Fabrication.* McGraw-Hill, 2004.

[66] W. Kern. Overview and evolution of semiconductor wafer contamination and cleaning technology. In W. Kern, editor, *Handbook of Semiconductor Wafer Cleaning Technology - Science, Technology, and Application*, pages 3–67. Noyes Publications, 1st edition, 1993.

[67] Harrick Plasma, 120 Brindley St. Ithaca, NY 14850. *User's Manual for the Basic Plasma Cleaner PDC-32G (115V) or PDC-32G-2 (230V) (and Optional Plasmaflo).*

[68] X. G. Zhang. *Electrochemistry of silicon and its oxide.* Kluwer Academic/Plenum Publishers, 2001.

[69] M. Ikeda, S. Iwamoto, and N. Nagashima. Behavior of fluorine on silicon (100) surfaces etched with NH4F aqueous solutions. *Electronics and Communications in Japan*, 83:41–58, 2000.

[70] T. Takahagi, A. Ishitani, and H. Kuroda. Fluorine-containing species on the hydrofluoric acid etched silicon single-crystal surface. *J. Appl. Phys.*, 69:803–807, 1991.

[71] K. Ljungburg, U. Jansson, S. Bengtsson, and A. Soderbarg. Modification of silicon surface with H2SO4:H2O2HF and HNO3:HF for wafer bonding applications. *J. Electrochem. Soc.*, 143:1709, 1996.

[72] T. Takahagi, I. Nagai, A. Ishitani, and H. Kuroda. The formation of hydrogen passivated silicon single crystal surfaces using ultraviolet cleaning and HF etching. *J. Appl. Phys.*, 64:3516, 1988.

[73] J. George. *Preparation of Thin Films.* Marcel Dekker, Inc., 1992.

[74] http://www.hemcocorp.com/index.html, Accessed Date: May 14, 2009.

[75] S. D. Klocke and W. Whyte. *Cleanroom Design.* John Wiley & Sons, 2nd edition, 1999.

[76] http://www.vaisala.com, Accessed Date: May 18, 2009.

[77] S. K. Estreicher. Dyanmics of hydrogen in silicon. In G. R. Myneni and S. Chattopadhyay, editors, *Hydrogen in Materials and Vacuum Systems*, volume AIP Conference Proceedings 671, pages 40–48, 2003.

[78] M. Stavola. Hydrogen in semiconductors. In G. R. Myneni and S. Chattopadhyay, editors, *Hydrogen in Materials and Vacuum Systems*, volume AIP Conference Proceedings 671, pages 21–30, 2003.

[79] S. Chapman and T.G. Cowling. *The Mathematical Theory of Non-Uniform Gases.* Cambridge University Press, 3rd edition, 1970.

[80] J. Rothenberger. (private communication), 2009.

[81] D. Montenegro. (private communication), 2009.

Appendix A

MU prototype Q-DLTS unit

Figure A.1: A schematic diagram of MU prototype QDLTS unit [81].

VITA

Annie YuNing Hsu Tipton was born in Taipei, Taiwan on November 16, 1979. She attended Ruamrudee International School in Bangkok, Thailand. She completed a Bachelor of Science degree in Radiation Science at Chang Gung University in Tao-Yuan, Taiwan in July 2002. She then continued her education at the University of Missouri in Columbia, completed a Master of Science degree in Nuclear Engineering in August 2005, and a Doctor of Philosophy degree in Nuclear Engineering in August 2009. She is married to Dr.Earl Lynn Tipton.